UNIVERSITY OF CALIFORNIA

Santa Barbara

Designing Light-material Interactions for Soft Robotics

A dissertation submitted in partial satisfaction of the

requirements for the degree Doctor of Philosophy

in Mechanical Engineering

by

Luke F. Gockowski

Committee in charge:

Professor Elliot Hawkes, Co-Chair

Professor Megan T Valentine, Co-Chair

Professor Javier Read de Alaniz

Professor Yangying Zhu

September 2022

The dissertation of Luke F. Gockowski is approved.

_____
Professor Javier Read de Alaniz

_____
Professor Yangying Zhu

_____
Professor Megan T. Valentine, Committee Co-Chair

_____
Professor Elliot W. Hawkes, Committee Co-Chair

September 2022

Designing Light-material Interactions for Soft Robotics

by

Luke F. Gockowski

ACKNOWLEDGEMENTS

The list of people who made the journey to the PhD both possible and worthwhile is a long one. As much as I could write an essay about each of these people, I'll keep it short and sweet. Each of these people were critical in either some part or all of sparking my interest in science & engineering, my interest in research, getting into a PhD program, and finding a way to push through.

Ms. Russel — Ms. Russel was my 2nd grade science teacher (yes, we're going this far back) while I was living in Cameroon. She opened my eyes to the physics of phenomena that surround us (like ice melting or how butter is made) and how to look for explanations for them. I can't even remember your first name but thank you Ms. Russel! Few things stand out to me as I try to recall 2nd grade, but her classes live vividly and rent-free in my memories.

Mr. Sean Godack — Mr. Godack was my high school calculus teacher. He offered patience and taught me fundamentals that filled the gaps in my patchwork schooling that spanned three countries and two different school systems. I definitely would not have made it through undergraduate or graduate school without those fundamentals. Thank you, Mr.

Godack!

Ms. Star Sharp — Star was the program director the Penn State Millennium Scholars Program. She wore innumerable hats—serving as mom away from home, program director and disciplinarian, and our greatest supporter and advocate. Star, thank you for your infectious hustle, your care, and everything you've done for me and all the Scholars!

Dr. Tak Sing Wong — Dr. Wong was the coolest undergraduate research adviser I could ask for. He was very relaxed, relatable, funny, and his ability to enjoy his job made me entertain the idea of a professorship one day (after graduate school, I no longer entertain that idea). The greatest gifts he gave me were confidence in my creativity, artistic freedom, encouragement, and a light-hearted but rigorous approach to research. Thank you, Tak Sing!

The Wong Lab — A huge thank you to the Wong Lab for being so supportive, even several years later, and staying in touch like a family. I want to especially thank my undergraduate research mentor, Birgitt Boschitsch—the kindest, most supportive

	and enthusiastic mentor anyone could ask for!
Dr. Megan Valentine	Megan has been my graduate adviser since day one of graduate school (I was pretty adamant about joining her lab after visiting). The greatest gifts she has given me has been intellectual freedom, level-headed discussions (especially when I'm freaking out about things I don't need to freak out about), a deep well of knowledge of materials characterization, and connections to people who do good science. Thank you for your support, Megan!
Dr. Elliot Hawkes	Elliot began co-advising me around my third year of graduate school, as I also weaseled my way into his lab. The greatest gifts he's given me are teaching me a lean approach to rapid prototyping, his unending refinement of ideas, willingness to entertain "silly" ideas, a fun & light-hearted approach to doing research, unwavering enthusiasm, and infectious (perhaps endless) energy. Thank you, Elliot!
Hawkes & Valentine Labs	Valentine Lab is where I learned the ropes of graduate school. Thank you to Aimal and Marcela for taking me under your wings & helping me make sense of the madness

that is academia. Thank you Younghoon and Jaejun for being such jolly companions in the lab! Hawkes Lab brought unending silliness and fun to the ardors of research. Thank you Matt, Charlie, David, Nicholas, Anna, and all the undergraduates who rounded out the group—for selfless help, cooperation, and for not taking yourselves too seriously. The combination of personalities in this lab is sitcom-worthy and it definitely made the latter half of graduate school more enjoyable.

Collaborators

None of the science over the course of my PhD would be possible without some incredible PIs (Craig Hawker, Javier Read de Alaniz, Yangying Zhu, Bolin Liaio, Matt Helgeson, Noy Cohen, Bob McMeeking, and others) and some incredible collaborators (Neil Dolinski, Serena Seshadri, Charles Xiao, and others). We did some cool stuff and wrote about it! Better yet: some people have read it! Thank you also to all the undergraduates and other collaborators involved in these projects. Amy, you did great!

Staff

We have some incredible staff in the mechanical engineering department. Thank you Dave Bothman, Kirk Fields, Greg Dahlen, and Trevor Marks for being walking

encyclopedias of mechanical engineering knowledge with (mostly) open-door policies. I've enjoyed bothering each of you for answers over the years! Thank you to the front desk ladies Laura Reynolds, Julie Dunson, Melecia Valdez, and others for making the logistics of being a student-researcher much more manageable. Thank you also to the custodians and other folks "behind-the-scenes" who made my research possible without me evening knowing it.

My Support System

To my friends, old & new: thank you for your company, commiseration, support, and constant jokes to make light of what is a long, tough marathon. Souce, Sachira, Serena, Timnit, Azi, Aimal, Felicia, Melanie, and the whole Legion of Uglies (you know who you are): I appreciate you all dearly. Couldn't have made it through with a smile on my face if it wasn't for you guys. Love you! To my family: close & extended, thank you for your unwavering support and for constantly teasing me about being in school for so long. Love you! Miya: thank you for your unwavering love and support—through all the highs and all the lows—and for helping me make the best of this weird adventure. This PhD would not be possible without you. Love you beyond measure!

Finally, I would be remiss if I didn't acknowledge the National Science Foundation (NSF) for funding my research. The work presented herein was partially supported by NSF Grant # EFMA 1935327.

VITA OF LUKE F. GOCKOWSKI
SEP 2022

EDUCATION

University of California Santa Barbara *Sep 2017 – Sep 2022*
Mechanical Engineering, Ph.D. student

Penn State University *Aug 2013 – May 2017*
Mechanical Engineering, B.S. – Millennium Scholar

HIGHLIGHTED SKILLS

- **Software:** MATLAB, CAD (Solidworks), Arduino / C++, COMSOL, Solidworks Flow Simulation
- **Research:** experiment design, sensor selection, data collection & analysis, automated data processing, mechanical testing, imaging, electromechanical test assemblies, cross-disciplinary collaboration
- **Prototyping:** 3D printing, laser cutting, machining (lathe, end-mill, GD&T), molding/casting
- **Interpersonal:** collectivist attitude, consensus building, critical thinking, leadership, empathy

WORK EXPERIENCE

Researcher, Hawkes & Valentine Labs (Santa Barbara, CA)
Sep 2017 – Present

- Developing a solar-harvesting soft robot; characterizing & improving the thermodynamic efficiency of soft actuators; designed & built an electromechanical test setup for automated data collection (2020 – present).
- Characterized the photokinetics of novel light-responsive opacity-switching dyes; leveraging these findings to create light-actuated muscles (published, *Nature Communications*, DOI: 10.1038/s41467-020-16277-7)
- Characterized mechanical properties of novel multimaterial 3D prints (published, *Material Horizons*, DOI: 10.1039/D0MH00331J)

Mechanical Systems Analyst, KCF Technologies (State College, PA)
Apr 2017 – Aug 2017

- Leveraged computational fluid dynamics (CFD) to diagnose cavitation issues in fracking components
- Designed an improved manifold to minimize cavitation and increase fluid flow, verified by simulation
- Annual maintenance cost savings of >$20M for customer

Research Assistant, MIT Media Lab (Cambridge, MA)
Jun 2016 – Aug 2016

- Designed multi-nozzle extruder for architecture-scale deposition of bio-based inks (adviser: Dr. Neri Oxman)

Mechanical Systems Analyst, Boeing (Long Beach, CA)
May 2015 – Aug 2015

- Designed and implemented cost-effective solution to a repeated wing actuator mechanism failure

Research Assistant, Wong Lab for Nature-Inspired Engineering
(State College, PA)
May 2014 – Apr 2017

- Designed an automated electromechanical test setup for high cycle (i.e., >3000) probing of soap-film-based particle filters (published, *Science Advances,* DOI: 10.1126/sciadv.aat3276)
- Designed, fabricated, and tested a low-cost forward osmosis desalination unit (published, honors thesis)

TEACHING & LEADERSHIP

Instructor, Soft Robotics Weekend Workshop (Santa Barbara, CA)
Feb 2022 – Mar 2022

- Taught 12 students how to construct and model wearable sensors and smart materials, a flea-inspired jumping robot, and a soft robotic arm.

SAT Math Tutor, Gateway Educational Services (Santa Barbara, CA)
Oct 2017 – Present

- Taught effective problem-solving strategies to 10-student cohorts; increased scores by average of ~200 pts

Teaching Assistant, Intro to Machine Shop (Santa Barbara, CA)
Sep 2021 – Dec 2021

- Guided 40+ students on GD&T and best machining practices for machining an air-powered motor

Project Manager, PIPELINES Program (Santa Barbara, CA)
Jun 2018 – Aug 2018

- Managed & mentored a team of three students in their endeavor to build a miniaturized sub-sea optical repeater for the U.S. Navy. Advised students on technical communication and presentation.

SELECT PUBLICATIONS

1. Stogin, B. B., **Gockowski, L.**, Feldstein, H., Claure, H., Wang, J., & Wong, T.-S. (2018). **Free-standing liquid membranes as unusual particle separators.** *Science advances*, 4(8), eaat3276.

2. **Gockowski, L.** F., Dolinski, N. D., Chavez, R., Cohen, N., Eisenreich, F., Hecht, S., … Valentine, M. T. (2020). **Engineering crack tortuosity in printed polymer-polymer composites through ordered pores.** *Materials Horizons*, 7(7), 1854–1860.

3. Seshadri, S., **Gockowski, L. F.**, Lee, J., Sroda, M., Helgeson, M. E., Read de Alaniz, J., & Valentine, M. T. (2020). **Self-regulating photochemical Rayleigh-Bénard convection using a highly-absorbing organic photoswitch.** *Nature communications*, 11(1), 1–8.

4. Lee, J., Sroda, M. M., Kwon, Y., El-Arid, S., Seshadri, S., **Gockowski, L. F.**, … Read de Alaniz, J. (2020). **Tunable Photothermal Actuation Enabled by Photoswitching of Donor--Acceptor Stenhouse Adducts.** *ACS Applied Materials & Interfaces*, 12(48), 54075–54082.

5. Areyano, M., Booth, J. A., Brouwer, D., **Gockowski, L. F.**, Valentine, M. T., & McMeeking, R. M. (2021). **Suction-controlled detachment of mushroom-shaped adhesive structures.** *Journal of Applied Mechanics*, 88(3).

6. Xiao, C., **Gockowski, L. F.**, Liao, B., Valentine, M. T., & Hawkes, E. W. (2021). **Thermodynamically-informed air-based soft heat engine design.** *arXiv preprint* arXiv:2103. 14157.

7. Dolinski, N. D., Callaway, E. B., Sample, C. S., **Gockowski, L. F.**, Chavez, R., Page, Z. A., … Others. (2021). **Tough multimaterial interfaces through wavelength-selective 3D printing.** *ACS Applied Materials & Interfaces*, 13(18), 22065–22072.

SELECT PRESENTATIONS

1. Luke Gockowski, C. Xiao, E. Hawkes, M. Valentine, **"Designing Light-Material Interactions for Soft Robotics,"** Invited Virtual Seminar, Illinois Institute of Chicago (IIT) Department Seminar, 2021.

2. Luke Gockowski, E. Hawkes, M. Valentine, N. Cohen, **"Programmable stiffness in 3D-printed systems."** Oral Presentation, 56th Annual Technical Meeting of the Society of Engineering Science, St. Louis, MO (2019).

3. Luke Gockowski, S. Seshadri, J. Lee, M. Sroda, M. Helgeson, J. Read de Alaniz, E. Hawkes, M. Valentine, **"Photothermal actuation of a fluidic soft muscle."** Oral Presentation, American Physical Society, Denver, CO (2020).

4. Luke Gockowski, N. Dolinski, N. Cohen, B. McMeeking, C. Hawker, M. Valentine, **"One-step, multi-material 3D printing of fracture-resistant, mussel-inspired composites."** Oral Presentation, Gordon Research Conference, Ventura, CA (2019).

5. Luke Gockowski, J. Duro-Royo, N. Oxman, **"Robotic Extruder for the Water-Based Digital Fabrication Platform."** Oral Presentation, MIT Media Lab Summer Internship Presentations, Boston, MA (2016).

6. Luke Gockowski, BB. Stogin, TS. Wong, **"Particle retention mechanism on a liquid membrane."** Poster Presentation, Penn State Undergraduate Research Symposium, State College, PA (2015).

7. Luke Gockowski, J. Wang, and TS. Wong, **"Anisotropic Slippery Surfaces Inspired by Nature: When Pitcher Plant Meets Butterfly."** Oral Presentation, Pittsburgh Plate & Glass, Pittsburgh, PA (2014).

FIELDS OF STUDY

Major Field: Light-responsive materials for soft robotics

Studies in photoresponsive fluid systems with Dr. Javier Read de Alaniz and Dr. Matt Helgeson.

Studies in thermodynamics of solar-induced boiling with Dr. Yangying Zhu and Dr. Bolin Lao.

Studies in stereolithography and mechanical testing with Dr. Craig Hawker.

ABSTRACT

Designing Light-material Interactions for Soft Robotics

by

Luke F. Gockowski

Soft robotics represents a shift in engineering design methodology: one that draws inspiration from biology and strives to move away from complex, rigid assemblies of numerous discrete parts and towards soft assemblies comprised of relatively few parts. Proponents of this shift advocate that soft robots will enable safe operation around humans, increased resistance to mechanical damage, operation in hazardous environments, and other functions that are presently inaccessible via traditional (i.e., rigid) robotics. However, bringing these visions to life requires efficient energy systems, soft controllers, and new material systems.

This dissertation is an exploration of the myriad ways that light-material interactions can be leveraged to offer innovations in each of these areas. Light serves as the common thread among each of these investigations as it is an accessible form of energy that can be modulated (e.g., by wavelength or intensity) and transmitted (e.g., lasers) or harvested (e.g., sunlight) over long distances with highly tunable spatial and temporal precision.

First, we examine the capabilities of soft heat engines, identify their major sources of losses and offer three key insights that soft roboticists can leverage to minimize them (Chapter II). Second, we investigate the photokinetics of a novel class of photoswitches, which constitute the basis for a thermofluidic switch (Chapter III). Finally, we investigate the mechanical properties of bio-inspired stiff-soft multi-material composites that exhibit impressive toughness (Chapter IV).

These endeavors at the intersection of materials, mechanics, chemistry, and thermodynamics put forth foundational knowledge that advances the field of soft robotics and also inspires new avenues for meeting the growing demand for adaptive and autonomous materials and devices.

TABLE OF CONTENTS

I. Introduction

Light, in its broadest sense (i.e., electromagnetic radiation), constitutes one of the most spectacular mediums of energy exchange in our universe. For example, consider a common house plant bathing in sunlight as it rests on a windowsill. Sunlight—a broad shower of electromagnetic radiation that spans wavelengths from 250 to 2500 nm—hurdles through space at 300,000 km s^{-1} (~670 million miles per hour), traverses a minimum distance of 146 million km (91 million miles) to reach Earth, scatters partially as it interacts with gases and particulates in the atmosphere, and eventually passes through the transmissible glass of the window where it finally irradiates the leaves of the plant. There, a surprisingly small portion of this light (i.e., ~3-6%) is used in the process of photosynthesis.[1] The remaining 94-97% of light might be rejected or converted via a variety of pathways: reflection off the surface of the leaves, transmission through the leaves, or absorption and eventual emission as infrared radiation / heat (i.e., non-photochemical quenching) or fluorescence (i.e., chlorophyll fluorescence).

This toy example illustrates some of the impressive properties of light, but also the unique light-material interactions that dictate how it is converted from one form of energy into another. Indeed, light can be modulated (e.g., filtered by wavelength) and transmitted (e.g., lasers) or harvested (e.g., sunlight) over long distances with tunable spatial and temporal precision. Investigating and leveraging the unique properties of light has been the subject of centuries of research. We continue this

[1] Estimate from the Food and Agriculture Organization of the United Nations.

tradition by playing with light in myriad ways to uncover what innovations it has to offer to the field of soft robotics. The sections that follow provide necessary background for later chapters detailing each of our innovations.

1.0 Primer on Soft Robotics

What is the goal of robotics? As researchers responsible for the ever-evolving future of this field, this question is worth constant consideration. For the purposes of this dissertation, however, we suggest that the goal of robotics is to develop autonomous and/or cooperative machines that improve the well-being of humans. Toward this end, most robots to date have been designed from rigid components (e.g., metals, rigid polymers) that enable speed, power, precision, and efficiency in completing tasks where humans would otherwise underperform or be at risk of harm (e.g., repetitive tasks such as the welding of car bodies on an assembly line). However, these same properties can make traditional robotics unsafe for operation around humans and inept at navigating unmapped, natural environments.

Thus, the goal of soft robotics is to "endow robots with new, bioinspired capabilities that permit adaptive, flexible interactions with unpredictable environments" and safe interaction "with humans and natural environments" [1]. "Soft" here refers to mechanisms and materials that demonstrate compliance—e.g., compliant mechanisms, polymeric materials, and/or elastomeric materials. Due to their flexible and adaptive nature, soft robots have been described as good candidates for deployment in hazardous search-and-rescue environments [2], in wearable assistive robotics [3], [4], and in biomedical devices [5]. However, for this

potential to be fully realized, breakthroughs are required in areas of challenge that are also common to rigid robots [6]:

1. **New materials & fabrication schemes** for developing the multifunctional, power efficient, compliant, and autonomous soft robots of the future.
2. **New power sources, battery technologies, and energy-harvesting schemes** that enable long-lasting operation of soft robots.
3. **Control schemes that enable navigation and exploration in extreme environments**—i.e., the ability to adapt and overcome unmapped and unpredictable terrain.

This dissertation details how we leverage the properties of light to address some of these challenges: (1) as an energy source, (2) as a switch, and (3) as a tool for material synthesis. Sections B, C, and D that follow lay out fundamental principles that we revisit in Chapters II, III, and IV, respectively.

1.1 Light as a Renewable Energy Source

Sunlight is an abundant and renewable energy source that fuels most life on Earth. Records of harvesting sunlight for human exploits span several millennia: from ~300 B.C. when Greeks & Romans used reflected sunlight from “burning mirrors” to light torches in sacred ceremonies, to present-day development of increasingly efficient photovoltaic cells. Faced with the challenge of untethering soft robots from unwieldy power sources (e.g., compressed air tanks, voltage sources), soft roboticists are increasingly turning to artificial light [7]–[9] or sunlight [10], [11] for

the wireless, long-range excitation of soft robots. The requisite softness for soft robots negates the use of traditional light-harvesting robotics equipment—e.g., rigid photovoltaic cells, electric motors, linkages, etc.—for their construction. As such, soft thermally actuated phase-change actuators (STAPAs) driven by light have been the subject of several reports [7]–[10].

The prototypical light-driven STAPA comprises a deformable constraint (e.g., silicone, thin polymer sheet) that encapsulates a low-boiling point fluid (e.g., ethanol, Novec 7000) and an absorber (**Fig. 1**). Light passes through the transmissible boundary, irradiating the absorber which then converts light energy to heat.

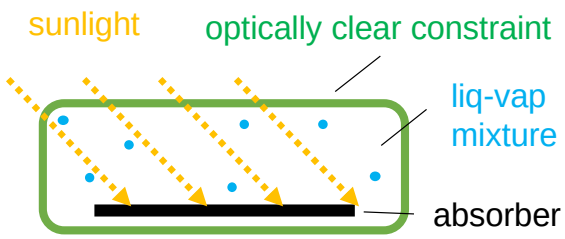

Fig. 1. Schematic of a prototypical soft thermally activated phase-change actuator (STAPA). The STAPA comprises an optically clear deformable constraint that allows sun to irradiate its contents—i.e., a solar absorber and a working fluid. As the absorber converts solar energy into thermal energy, the temperature of the working fluid is increased until it reaches saturation (i.e., boiling) temperature.

Heat generated by the absorber warms the working fluid until it reaches its saturation temperature (i.e., boiling) at which time vaporization and thus volume expansion can occur. In the process of volume expansion work is done by ($W_{net} > 0$) the system to its surroundings—e.g., against atmosphere or against a useful

load. In the process of compression, work is done to ($W_{net} < 0$) the system. The net work done by the STAPA is known by taking the product of net pressure at its physical boundary, $P(v)$ (which varies with actuator volume, v) and incremental volume changes, dV:

$$W_{net} = \int P(v)dV \tag{1}$$

This basic principle describes the process by which most researchers have demonstrated motion, locomotion, or anthropomorphic tasks (e.g., grasping, lifting). However, in the endeavor to create "new power sources, battery technologies, and energy-harvesting schemes that enable long-lasting operation of soft robots," few have investigated the efficiency with which light (and then heat) is converted into useful work. Noting this knowledge gap, in Chapter II, we analyze the dominant sources of losses inherent to the use of STAPAs in soft robots, offer design guidelines for their minimization, and demonstrate the utility of these guidelines via a compliant solar-powered roller capable of locomotion using only the modest flux of sunlight.

1.2 Light as a Material Stimulus

Light is increasingly being recognized as an appropriate material stimulus due to its wavelength tunability, wireless delivery, high spatial and temporal resolution, and relative sustainability (as it does not produce the wasteful byproducts inherent to

chemical fuels). These properties constitute the basis of communication across length scales—e.g., the activation of photoswitches. Photoswitches are molecules that can switch reversibly between stable and metastable isomeric states in response to light. Tuning and leveraging the properties associated with each of these states form the basis of several investigations (e.g., “smart” polymers [12]), including our own.

In 2014, Helmy and co-workers reported synthesis of a new class of organic photochromic molecules that offers an unprecedented combination of negative photochromism, tunable photoswitching using visible light, sustained performance over high cycle numbers, impressive molecular length changes, and large polarity changes [13]. Termed donor-acceptor Stenhouse adducts (DASAs), this first class of organic photoswitches (DASA 1.0) were found to switch from a conjugated, colored, and hydrophobic conformation to a ring-closed, colorless, and zwitterionic conformation upon irradiation with visible light (**Fig. 2**).

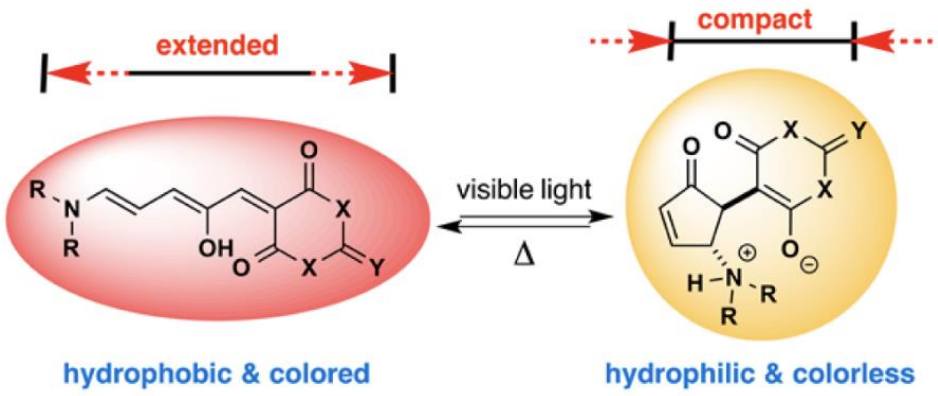

Fig. 2. Donor-acceptor Stenhouse adducts (DASAs), a new class of visible-light-mediated organic photoswitch. Adapted, with permission, from [13].

Though this was an impressive inaugural demonstration of visible-light-induced photoswitching, this first class of DASAs had a narrow and non-tunable absorption window (i.e., λ = 545−570 nm) and were reversibly active in nonpolar media (e.g., toluene). These shortcomings were addressed four years later, with the synthesis of a new generation (i.e., DASA 3.0) that possessed improved color tunability (i.e., λ = 585−735 nm) and switchability in polar and nonpolar media. In addition, ultraviolet-visible (UV-vis) spectrophotometery revealed that the absorbance of this new class of DASA is nearly 60% greater that of non-switching organic dyes with comparable peak absorbances (**Fig. 3**). This unique property, combined with the negative photochromism of DASAs (i.e., switching from a colored to colorless state upon irradiation) result in relatively high-velocity (~mm s^{-1}), thermally driven, self-regulating flows at modest light intensities (i.e., ~25 mW cm^{-2}).

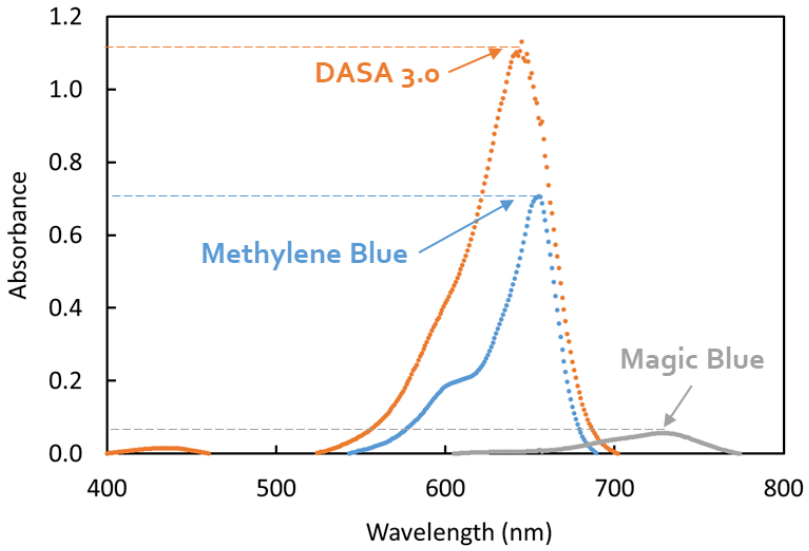

Fig. 3. Third generation donor-acceptor Stenhouse adducts (DASA 3.0) outperform commercially available organic dyes with comparable peak absorbances.

Self-regulating flows arise as a result of "bleaching fronts" that propagate through the fluid volume (**Fig. 4**). As these fronts propagate, they cause temporally- and spatially-varying absorbance and thus thermal gradients that incite buoyancy-driven flows. The solvent-dependency of this photothermally-induced fluidic behavior is the primary subject of investigation in Chapter III.

DASA 3.0's negative photochromism and high absorbance also can be leveraged switch between heat generating and heat rejecting states. For example, we found that a high-concentration (>5 mM) solution of DASA 3.0 in dichloromethane (DCM) irradiated with ~51.5 mW cm^{-2} was sufficient to incite liquid-to-vapor phase change inside of a polymeric pouch. We offer thoughts on how this feature might constitute future investigations of thermal switches in Conclusions & Future Directions.

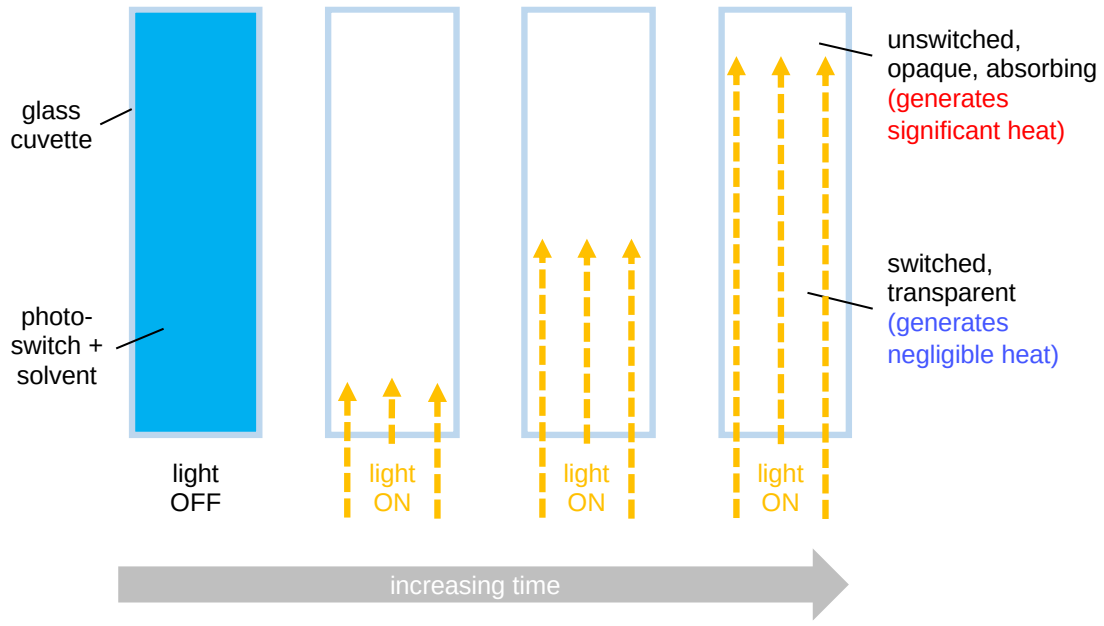

Fig. 4. The use of negative photochromes enables coherent "bleaching fronts," that propagate in the depth of the direction of light.

1.3 Light as Tool for Material Synthesis

In the previous section, the negative photochromism of DASAs enabled "bleaching fronts" that were responsible for the dynamic self-regulating flows we discuss further in Chapter III. However, these same bleaching fronts also offer a route by which light attenuation can be circumnavigated and light can propagate at a programmable rate through a medium. Indeed, the Beer-Lambert Law describes the attenuation of light as it passes through a medium:

$$A = \epsilon l C \tag{2}$$

From this relationship, it can be seen that the amount of light absorbed by the solution, A, is linearly related with the concentration of the species, C, and its molecular attenuation coefficient, ϵ; l is the optical path length in cm. While this effect is still present at the bleaching front, the bleaching front propagates through the solution at a rate that can be modeled and tuned. As we will see in Chapter III, modeling the rate of bleach front propagation can be challenging in low viscosity solvents with large thermal gradients because simultaneous convective flows influence the velocity of the bleaching front. However, in the highly viscous fluids the velocity of the bleaching front, V_{front}, is driven simply the quantum yield of photoinitiator consumption, ϕ_0, incident intensity, I_0, and the initial photoinitiator concentration, $C_{A,0}$ [14], [15]:

$$V_{front} = \frac{\phi_0 I_0}{C_{A,0}} \tag{3}$$

The predictability of this reaction was hypothesized to be suitable for stereolithography—where controllability, repeatability, and accuracy are required for 3D printing.

In 2018, Dolinski and co-workers exploited this phenomenon to control the rate of free radical polymerization in a new stereolithographic method—i.e., solution mask liquid lithography (SMaLL) [16]. Critically, the use of coherent bleaching fronts that propagate at a predictable velocity through a resin bath enabled large depths of cure and rapid build rates without moving parts or mechanical assemblies. In

addition, resin mixtures with two orthogonal photo-crosslinking systems (i.e., activated via different wavelengths of light) could be selectively polymerized to produce polymer-polymer composites with spatially varying elastic moduli and extremely good interfacial bonding between phases. Notably, this stepwise spatial change in modulus does not sacrifice mechanical strength. Furthermore, in a recent investigation, we proved the hypothesis that a continuous acrylate network bridging both material domains results in remarkably tough interfaces [17]. Additionally, continuous photopolymerization in the depth of the resin feedstock eliminates layering defects intrinsic to stereolithographic systems with translating stages.

These characteristics of SMaLL make it a formidable platform for creating bio-inspired polymeric composites whose mechanical properties can be investigated. Indeed, nature is replete with composites whose simultaneous toughness and strength draw upon strong interfaces joined by soft (e.g., biopolymer) and hard (e.g., mineral) domains [18], [19]. In Chapter IV, we draw inspiration from these motifs, leverage SMaLL to print bio-inspired stiff-soft polymer-polymer composites with templated porosity, and finally investigate their mechanical properties. The continued development of SMaLL, as well as comparable multi-material printing techniques with good interfacial strength, is vital to the development of future bio-inspired soft robots.

We dive deeper into each of these studies in the chapters that follow.

II. Thermodynamically informed heat engines for soft robots

2.0 Abstract

A core challenge for the field of soft robotics is untethering fluidically actuated robots from unwieldy power sources to increase their mobility and functionality. One potential solution explored in the literature is the soft heat engine, which uses wirelessly activated, thermally-driven liquid-to-vapor phase change processes to do work. Phase change processes are an attractive means of untethering from pneumatic pumps because they enable large strokes and impressive forces. Despite this advantage, soft heat engines in the literature suffer from meager cycle efficiencies (<0.002 percent), and little work has focused on the sources of energy loss. Furthermore, the unique constraints of soft heat engines—i.e., low operating pressures and temperatures, significant heat losses, non-flow processes, and deformable boundaries—warrants thermodynamic analysis of this new problem. Herein, we identify major sources of losses in soft heat engines and offer three key insights that soft roboticists can leverage to minimize them: (1) maximize power input, (2) operate at the system's optimal temperature, and (3) maximize volumetric expansion. We confirm the validity of these insights via benchtop experiments and demonstrate efficiencies nearly two orders of magnitude higher than previously reported. We demonstrate the usefulness of these insights by applying them to the design and construction of a compliant roller capable of locomotion using only the modest flux of sunlight (~870 W m^{-2}). Our results guide the design of efficient

thermally activated actuators and spur scientific inquiry into a new generation of untethered, mobile, and more capable soft robots.

2.1 Introduction

Due to their flexible and adaptive nature, soft robots have been described as promising candidates for deployment in hazardous search-and-rescue environments [2] or in wearable assistive robotics [20], [21]. However, this potential has yet to be fully realized, partly due to prohibitive tethering to unwieldy power sources (e.g., compressed air pumps), which often dwarf the robots in mass and size, and hinder their mobility. Recognizing this limitation, efforts to eliminate these bulky power sources have included using wireless micro-compressors [22], [23], monopropellant [24]–[26], combustion [27]–[29], and soft thermally-activated phase-change actuators [4], [7]–[10], [22], [30]–[47]—we term these STAPAs.

While each of these approaches has its strengths and weaknesses (reviewed elsewhere [3]), we focus specifically on STAPAs because of their low-complexity and promising ability to achieve large strokes and high forces [30]. STAPAs typically comprise a soft constraint (e.g., an elastic silicone case), a low-boiling-point fluid (e.g., ethanol), and an electrical heat source (e.g., nickel chromium wire and a voltage source). For untethered operation, wireless liquid-to-vapor phase change has been demonstrated via magnetic induction [30], [32] and light stimulus [7]–[9].

For both tethered and untethered STAPAs, however, very little attention has been given to improving their thermal efficiency. Indeed, most literature on STAPAs

neither focuses on nor reports the thermal efficiency of a complete work cycle (i.e., expansion and compression) [4], [9], [10], [34]–[47], favoring other methods of efficiency reporting instead (e.g., efficiency of expansion alone) [7], [8], [30]–[32]. Even when work cycle efficiency is accurately reported, the highest reported value in the literature is presently ~0.0018% [33]. For STAPA-driven soft robots to become a practically relevant technology, thermodynamic analysis that offers design guidelines for improving efficiency is needed. Interestingly, the unique combination of constraints inherent to small-scale soft heat engines—i.e., relatively low temperatures and pressures of operation, construction from soft polymeric materials, and cyclic processes in a deformable constraint (see Supplementary Text S1 for further discussion)—warrant thermodynamic analysis of this new problem.

Herein, we apply thermodynamic theory to this new class of heat engine (Fig. 5A) to identify dominant sources of energy loss and illuminate key design principles for minimizing them (Fig. 5B). Experimental application of these theoretical insights yields actuators with an efficiency of up to 0.235% (Fig. 5C), which is more than two orders of magnitude higher than previously reported [33]. In turn, we demonstrate through a proof-of-concept compliant roller that application of these insights can enable soft robot locomotion using only the modest flux of sunlight. Our work offers critical insights for improving the efficiency of soft heat engines and demonstrates how this solution might inform the next generation of untethered, mobile, and adaptable soft robots.

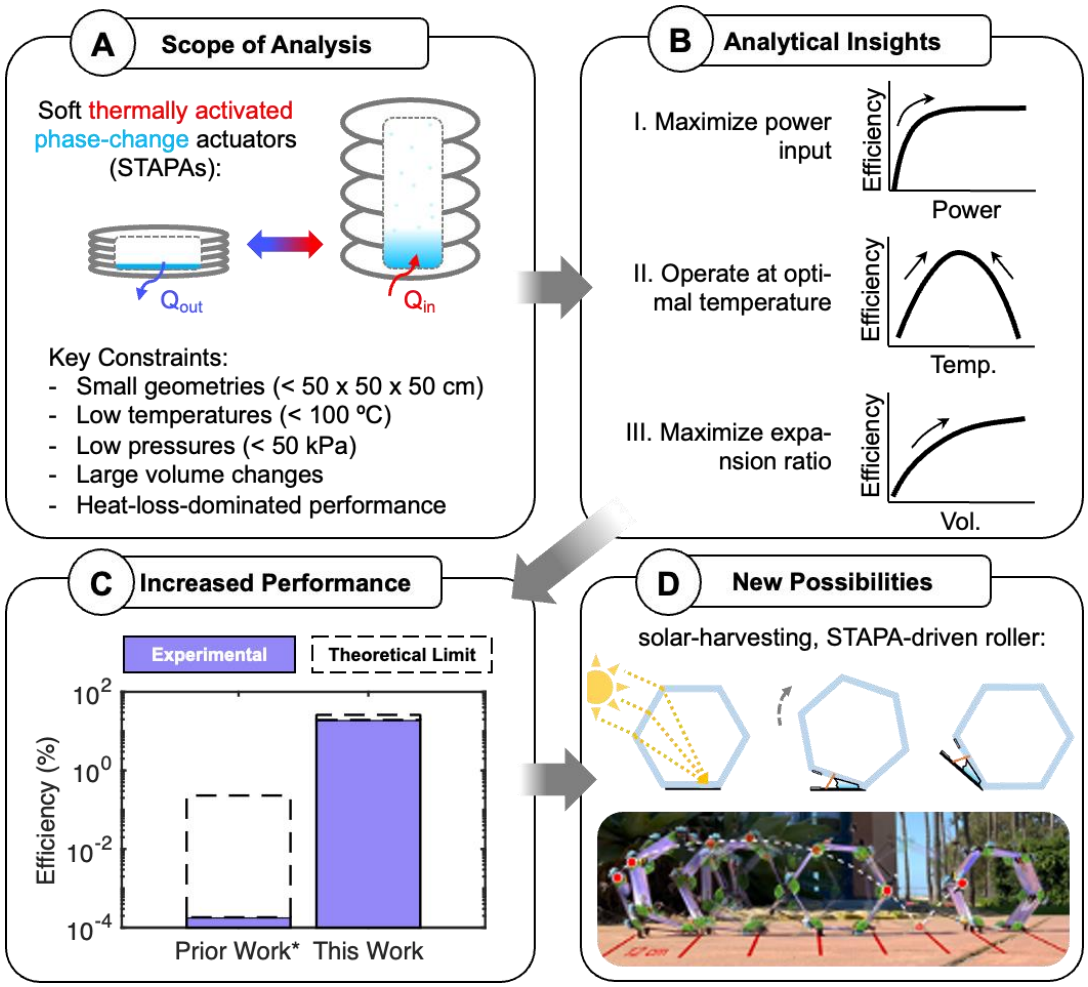

Fig. 5. A graphical abstract illustrates the scope of our thermodynamic analysis, key insights from it, significant efficiency improvement that can be reaped when applied, as well as a compliant solar-driven roller that was made possible via our theoretical insights. (**A**) Key characteristics of soft thermally activated phase change actuators (STAPAs) distinguish them from large industrial phase-change-based processes. These key differences warrant new thermodynamic analysis. (**B**) Our analysis illuminates the greatest common sources of inefficiency for STAPAs. Further, we identify three key thermodynamic insights that can be leveraged by soft robot designers for efficient operation. (**C**) Recreating the trends we predicted in theory via benchtop experiments, we find that our soft actuators outperform prior work (*see ref. [33]) by just over two orders of magnitude. Furthermore, we are operating at roughly 3.4% of

the theoretical efficiency limit of our system. (**D**) Applying these insights, we demonstrate a compliant roller capable of locomotion using only the diffuse flux of sunlight.

2.2 Results

2.2.0 Theory

2.2.0.0 Sources of Energy Losses

We identify sources of energy loss in soft heat engines by examining deviations from the Carnot heat engine. The Carnot heat engine is a theoretical construct used to describe the upper limit of heat engine efficiency. The Carnot heat engine undergoes the Carnot cycle, which involves reversible processes that are extremely challenging to recreate experimentally. As soft heat engines deviate from the Carnot cycle, they incur two categories of loss we term temperature limit losses and process limit losses; there is some overlap between the two categories.

Temperature limit losses are inefficiencies due only to temperature and can be identified by examining the Carnot efficiency:

$$\eta_C = 1 - \frac{T_c}{T_h} \tag{4}$$

Here, T_c and T_h are the cold and hot reservoir temperatures, respectively. Losses are minimized when T_c/T_h approaches 0; however, several material constraints (e.g.,

thermal degradation of soft materials) make it challenging to achieve this. We discuss opportunities to develop materials that address temperature limit losses in the Supplementary Text S2, however, such investigations lie outside the scope of this paper as new materials synthesis is generally less accessible to soft roboticists.

Conversely, methods for addressing process limit losses are generally more accessible to the soft roboticist. The three process limit losses are cycle shape loss, heat loss, and non-useful work. The remainder of energy that hasn't been lost can be converted to useful work. First, cycle shape losses are incurred due to deviations from the Carnot cycle. While the Carnot cycle is most efficient, it is much easier to experimentally realize a rectangular shaped cycle—e.g., via a STAPA undergoing constant-load expansion and compression. Here, cycle shape losses are the difference between Carnot cycle and the ideal rectangular shaped cycle ($\eta_C - \eta_{r,ideal}$). The efficiency of the ideal (i.e., lossless) rectangular shaped cycle, $\eta_{r,ideal}$, is derived in the Supplementary Text S3 and is:

$$\eta_{r,ideal} = \frac{(P_2 - P_1)(v_3 - v_2)}{\hbar_3 - \hbar_2 + u_2 - u_1} \tag{5}$$

Here, P is system pressure, v is specific volume, $\hbar$ is specific enthalpy, and u is specific internal energy. Subscripts correspond to discrete thermodynamic states in the cycle (see Materials & Methods).

The second process limit loss is heat loss to the environment. The efficiency of a rectangular-shaped cycle with heat losses, $\eta_{r,ht}$, is also derived in the Supplementary Text S4 and is as follows:

$$\eta_{r,ht} = \eta_{ht}\eta_{r,ideal} \cong \left(1 - \frac{h(T_2 - T_\infty)}{\dot{q}_{in}}\right)\eta_{r,ideal} \quad (6)$$

Here, h is the lumped heat loss coefficient, T_∞ is the ambient temperature, and $\dot{q}_{in}$ is the power input. We observe that the efficiency of the rectangular cycle with heat losses is the ideal efficiency multiplied by a prefactor, which we call the heat transfer efficiency term, η_{ht}.

The third process limit loss is non-useful work. Some of the working fluid pressure-volume work is used to overcome parasitic forces such as material hysteresis or system friction that could otherwise be converted to useful work. The remaining fraction of work done by the fluid that goes to useful work is η_W, which we term work efficiency. Thus, the total efficiency of the rectangle cycle with heat transfer and work efficiency, $\eta_{r,htw}$ accounted for is:

$$\eta_{r,htw} = \eta_w\eta_{ht}\eta_{r,ideal} \quad (7)$$

2.2.0.1 Methods for Minimizing Losses

Analysis of the rectangle cycle with heat transfer and work efficiency (Equation 3) suggests three such methods for improving efficiency: (1) maximize power input, (2) operate at the optimal temperature, and (3) maximize fluid vaporization. The first insight emerges from the prefactor term η_{ht} in Equation 3, which suggests that the ideal efficiency (i.e., Equation 2) is approached as $h(T_2 - T_\infty)/\dot{q}_{in}$ approaches zero. To achieve this h should be minimized, for example by adding insulation that minimizes losses. However, commercially available soft, extensible insulating skins with low losses (e.g., hysteresis) are scant. As such, maximizing the power input $\dot{q}_{in}$ is an accessible method for minimizing losses. This is illustrated in Fig. 2A.

The second insight emerges from both terms in Equation 3. Here, we note that pressure and temperature are directly related by the vapor pressure relationship of the working fluid. Thus, the ideal rectangle efficiency $\eta_{r,ideal}$ suggests that an increasing pressure during expansion (P_2) and thus temperature during expansion (T_2) has a positive effect on efficiency. Conversely, the prefactor η_{ht} suggests that increasing temperature during expansion has a negative effect on efficiency. As such, these competing factors result in an optimal temperature for maximizing efficiency, as is illustrated in Fig. 2B.

The third insight arises from the ideal rectangle efficiency term $\eta_{r,ideal}$. Here, maximizing fluid vaporization (i.e., maximizing the $v_3 - v_2$ term in Eq. 2) reduces the relative amount of energy spent merely warming the fluid (i.e., the $u_2 - u_1$ term in Eq. 5). This is illustrated in Fig. 2C. In summary, insight (1) offers a practical way to

minimize heat losses when insulating a STAPA is challenging, while the combination of insights (2) and (3) influence cycle shape losses by tuning the width (i.e., volume differentials) and the height (i.e., pressure differentials) of the cycle. We test the impact of these insights in the following section.

2.2.1 Experimental Investigation of Key Thermodynamic Insights

Here, we aim to translate our theoretical design insights into observable efficiency benefits for STAPAs. To this end, we test a bellows-like STAPA under a variety of thermal and mechanical conditions using a purpose-built testing apparatus (see Materials & Methods). Using this method, we verified that our first theoretical insight—i.e., that increasing power increases efficiency—applies to our system. To do so, we varied the amount of constant power supplied to the system. Indeed, we found that the predicted trend holds: increasing power results in more substantial efficiency gains when input power is low relative to heat loss rate and less substantial gains when input power is high relative to heat loss rate (**Error! R eference source not found.** 2D). These trends align with expected theory (Fig. 2A) and confirm that STAPA efficiency can be increased simply by maximizing power input, within the practical limits of a given system.

Second, we confirmed that our theoretical insight suggesting the presence of an optimal expansion temperature holds for our STAPA system. For this, we recognized that temperature and pressure are directly correlated when the system is at

saturation (i.e., boiling) and one can be used to tune the other. Thus, we increased pouch pressure and thus temperature by increasing the loads felt by the pouch (see Materials & Methods). Our results illustrate an expansion temperature optimum of 40.75 °C for our system (Fig. 2E) that enables roughly a six-fold increase in efficiency over the low-temperature case (i.e., 36.75 °C). This insight illustrates that STAPA efficiency can be greatly improved by identifying and operating at the optimal operating temperature of the system.

Lastly, we demonstrated that our third insight—increasing expansion ratio increases efficiency—applies to our system. Using the cycle shape that coincides with the optimal operating temperature (Fig 2E), we calculated the cycle efficiency at different volume expansion ratios (Fig. 2F). Volume expansion ratio is defined as the ratio of volume during expansion (i.e., liquid-vapor mixture) and the starting fluid volume (i.e., liquid). Here again, large increases in STAPA efficiency can be derived from maximizing expansion ratio within system constraints.

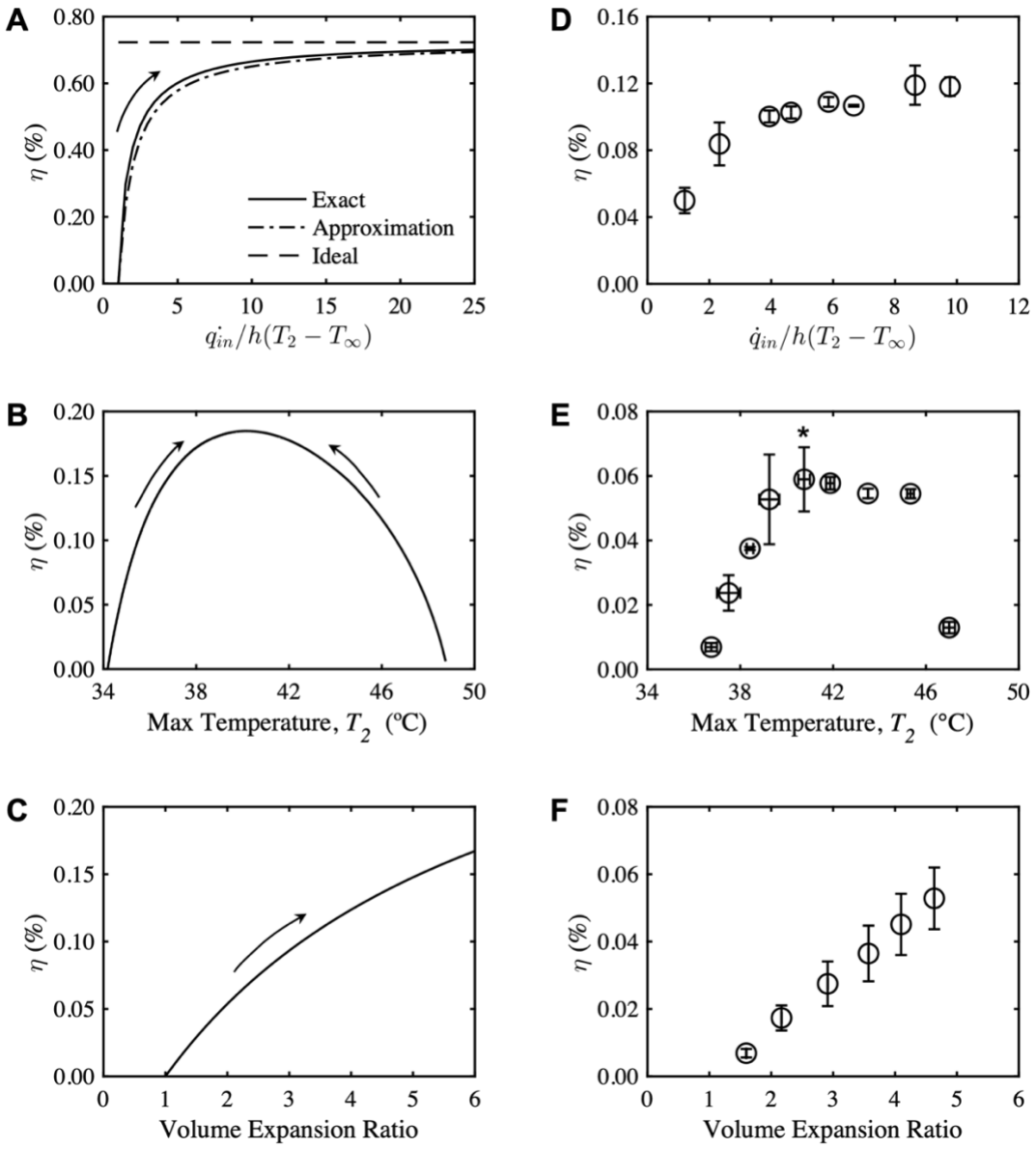

Fig. 6. Comparison of trends for efficiency maximization as predicted by theory (A-C) and observed experimentally (D-F). (**A**) A theoretical plot of the heat transfer coefficient term versus efficiency. Here, the power input $\dot{q}_{in}$ is varied and all other variables are held constant. The ideal curve plots the efficiency of the cycle with no heat losses. As $\dot{q}_{in}$ increases, both the exact and approximation curves trend towards the ideal limit. The approximation curve is [Charles, description]. The exact curve is [Charles, description]. (**B**) A theoretical plot of varying max temperature T_2 versus efficiency. Here, a temperature optimum occurs at ~40 ºC. (**C**) A

theoretical plot of volume expansion ratio versus efficiency. Here, volume expansion ratio is defined as the system volume (liquid-vapor mixture) divided by the initial volume of working fluid (pure liquid). (**D**) An experimental plot of the heat transfer coefficient term versus efficiency. Power input was varied from 1.3-10.0 W and the effect on efficiency was measured. Indeed, increasing power increases thermal efficiency. (**E**) An experimental plot of max temperature versus efficiency. Indeed, the experimental system has an optimal working temperature for maximizing efficiency. (**F**) An experimental plot of volume expansion ratio versus efficiency. Indeed, increasing expansion ratio results in increasing efficiency. Error bars for all plots represent standard deviation. All runs are N=3 unless denoted otherwise (i.e., *N=2).

Leveraging the insights above, we aim to demonstrate that with sufficient attention to the thermodynamics of STAPAs, even the modest flux of sunlight (i.e., ≤ 1000 W m^{-2}) can directly power soft robot locomotion. We imposed three design constraints to limit the number of possible designs: the locomotive must (1) not exceed a physical envelope of 15 cm x 30 cm x 30 cm, (2) be powered by a sunlight fueled STAPA, and (3) incorporate sufficient compliance to resist damage due to drops and/or mechanical crushing. Here, we introduce a STAPA-driven compliant roller capable of locomotion using only sunlight (Fig. 3). The sections that follow detail thermodynamically informed decisions made in its design.

2.2.1.0 Mode of Locomotion

The soft robotics literature is replete with diverse methods of locomotion: inching, rolling, jumping, eversion, and others. Of these, rolling is attractive because of the low force required for locomotion—i.e., equal to or greater than the drag forces. The

ideal STAPA-driven roller is composed of infinite sides (i.e., a cylinder) to minimize the work of locomotion, but also to maximize the number of actuators actively absorbing sunlight. Due to the “always-on” nature of sunlight, any time spent not absorbing sunlight is time that isn’t taking advantage of available energy and thus lowers system efficiency. At the same time, increasing the number of sides increases manufacturing complexity. As a result of these tradeoffs, we chose to design and construct a roller with six sides (Fig. 3A).

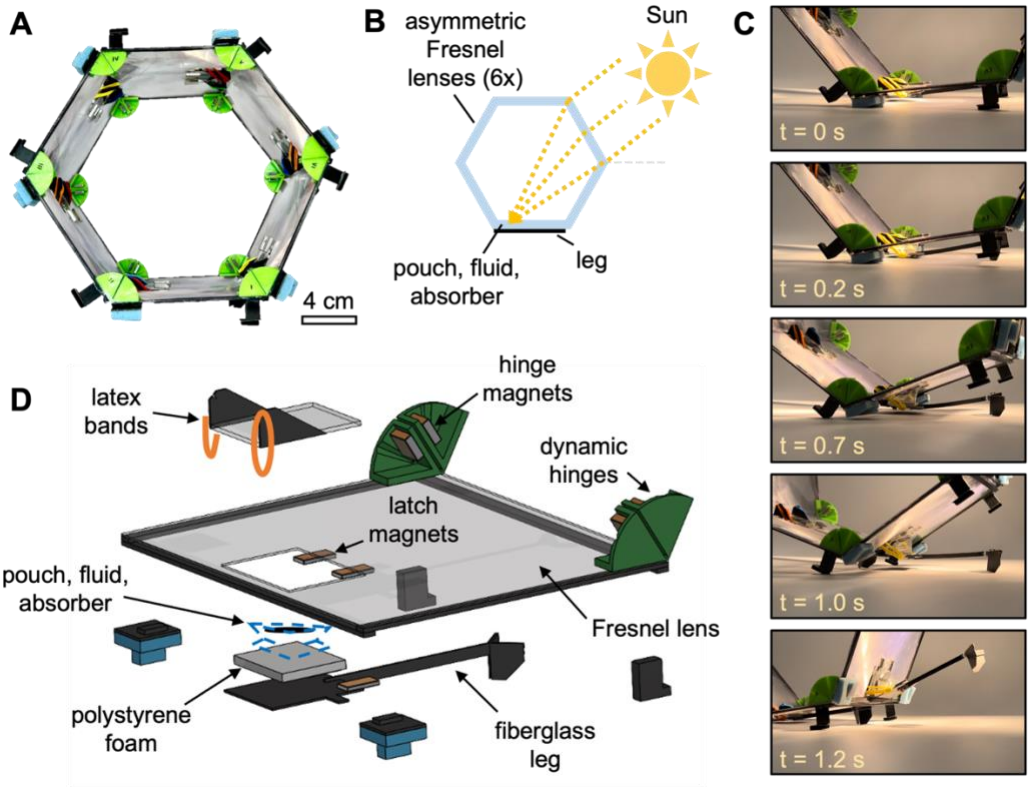

Fig. 7. Robot working principles and design. (**A**) We present a six-sided compliant roller capable of locomotion using only sunlight. (**B**) For a given side, actuation is made possible as sunlight is collected and concentrated through asymmetrical Fresnel lenses onto an adjacent pouch, which is nestled between the robot leg and its body. The pouch contains an absorber and

low-boiling point fluid. (**C**) As the fluid is vaporized, it generates increasing pressure until sufficient pressure is generated to overcome the force of a magnetic latch and flip the roller about a cloth hinge. (**D**) A labeled 3D rendering illustrates key components of one of the six robot sides. All sides are identical in construction. A fiberglass leg enables force transduction from the pouch. Magnets adhered to the leg create a latching mechanism that enforces a threshold pressure for actuation. Latex bands serve as a restoring load during the compression step of the cycle. Polystyrene foam minimizes heat losses to the body. Dynamic hinges offer stiffness during regular robot operation but can deform bi-directionally under loads that exceed the roller's weight.

2.2.1.1 Working Principle

Each side of the six-sided roller is equipped with an asymmetrical Fresnel lens that bends and concentrates light onto an adjacent pouch, sandwiched between a hinged leg and the robot body (Fig. 3B). In order to complete a flip (illustrated in Fig. 3C), each side of the roller is equipped with a variety of components (Fig. 3D) that enforce thermomechanical conditions that parallel those of our benchtop actuator experiments. Each heat-sealed pouch contains low-boiling-point fluid (Novec 7000) and a disk of black fabric that absorbs solar radiation. As the fabric absorbs sunlight, it generates heat and eventually incites vaporization of the working fluid.

Oscillating between heating and cooling states, each pouch progresses through a four-step cycle that parallels that of our benchtop tests. First, a constant-volume heating condition (Fig. 8A) is enforced by latch magnets (Fig. 7D, "latch magnets")

adhered to both the leg and the roller body. In this state, the system is supplied with heat, but no pressure-volume work is done. Second, once sufficient vapor pressure is generated, expansion and pressure-volume work against a load can occur (Fig. 8B). Here, the robot differs from our benchtop experiments in that no additional heat is input during the expansion stage (i.e., $\dot{q}_{in}$ = 0). This is because as soon as the robot body begins to rotate during a flip, the lenses fall out of alignment with the collimated light of the sun. As such, the latch magnets serve the secondary purpose of ensuring that sufficient energy has been harvested during the constant-volume heating phase for a flip to occur. Third, constant-volume cooling commences (Fig. 8C). In the benchtop experiments, the constant-volume condition is enforced by an angle limiter (see Materials & Methods); in the roller, this condition is set by the maximum volume of the pouch. Finally, compression using a relatively low load resets the system to its initial state (Fig. 8D). In the roller, this is achieved using the restoring force of the latex bands (Fig. 8D, “latex bands”). The compression pressure—and thus the condensation temperature—can both be tuned by tuning the strength of these latex bands. We design the thermodynamic cycle of our roller’s pouches to parallel that of our benchtop experiments so that we can apply the same three theoretical insights in its design.

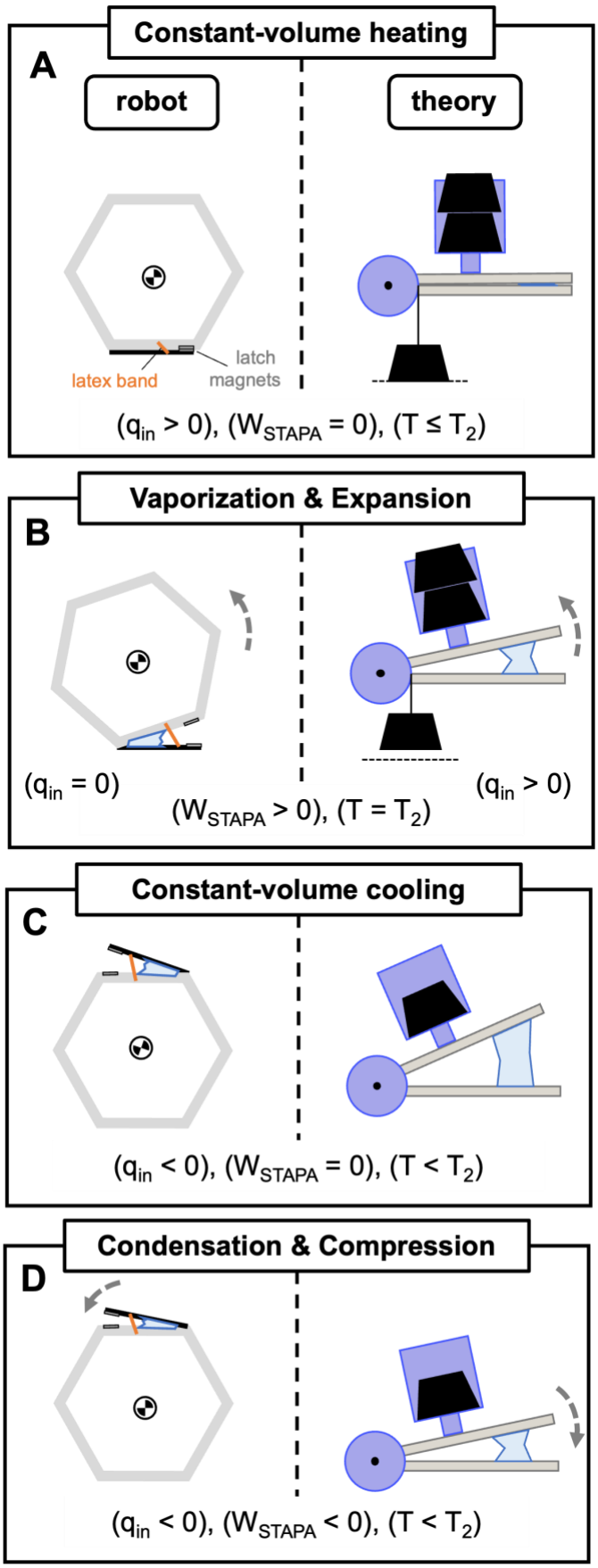
Constant-volume heating
A
robot
theory
latex band
latch
magnets
$(q_{in} > 0), (W_{STAPA} = 0), (T \leq T_2)$
Vaporization & Expansion
B
$(q_{in} = 0)$
$(q_{in} > 0)$
$(W_{STAPA} > 0), (T = T_2)$
Constant-volume cooling
C
$(q_{in} < 0), (W_{STAPA} = 0), (T < T_2)$
Condensation & Compression
D
$(q_{in} < 0), (W_{STAPA} < 0), (T < T_2)$

Fig. 8. Parallels between thermodynamic conditions in the roller, actuator experiments, and theory. (**A**) In the first state heat flows into the system (thus increasing the temperature of the fluid), however, the fluid remains below or equal to its saturation (i.e., boiling) temperature, T_2. No work is done in this process. (**B**) As heat continues to flow into the system, however, the fluid eventually reaches saturation temperature. At the saturation point, vaporization of the working fluid increases pressure and incites volumetric expansion. In the process, the STAPA does pressure-volume work against a resistive load. In the case of the robot, this enables a flip. (**C**) This panel illustrates the roller three flips later, with the leg at the top of the robot. As the actuator reaches maximum stroke, heat is rejected from the system in a temporary constant-volume condition. No work is done in this process. (**D**) As heat continues to be rejected, the fluid temperature eventually drops below the saturation temperature and vapor condensation occurs. As a result, pressure inside of the STAPA drops enough that the restoring loads can now do work to compress it back to its initial state.

2.2.1.2 Applying the Three Key Insights

The first insight states that power input should be maximized for maximum efficiency (Fig. 6A,D). Solar energy flows on a per unit area basis, implying that harvestable solar power input scales with increasing collector surface area. To maximize power input, we maximize the lens area within the self-imposed geometric constraint. Fresnel lenses made from polyvinyl chloride (PVC) are used here because of their flexibility and robustness to deformation. Additionally, they are easily cut in half—allowing light to be bent onto the adjacent pouch.

Next, our second insight suggests that each system will have an optimum working temperature that should be identified and at which the system should operate (Fig. 6B,E). Using Fresnel lenses, the roller harvests an estimated ~9-18W

of solar energy depending on the angle of the sun. Even at these higher powers, theory still predicts an optimum temperature (see Supplementary Text S12). To identify this optimum temperature, pressure (and thus temperature) was varied by varying the area of contact between the pouch and the roller body (i.e., contact area). We created a weight-matched replica of our roller and measured the time required for a flip to occur for each pouch size (Supplementary Materials, Fig. S16). In each condition, the pouch (invariant of its size) receives the same amount of light power and has the same quantity of work it must complete (i.e., flipping the roller). As such, the time required for a flip to occur is linearly inversely related to the efficiency of the STAPA:

$$\eta = \left(\frac{1}{t_{flip}}\right)\frac{W_{flip}}{\dot{q}_{lamp}} \tag{8}$$

Here, $\dot{q}_{lamp}$ is the power of the lamp supplying light energy, W_{flip} is the fixed amount of work required for a flip, and t_{flip} is the measured amount of time for the robot to flip. These experiments show that decreasing pouch size (i.e., increasing pressure/temperature) increased efficiency with diminishing gains. These diminishing gains may be indicative of an optimum, however, manufacturing constraints prevent us from testing pouches any smaller (Supplementary Materials, Fig. S16).

The final insight states that higher volume expansion ratios result in higher efficiencies (Fig. 6C,F). Recall that the volume expansion ratio is the ratio of the minimum and maximum volumes of the system. Though the maximum volume of the inextensible pouch is fixed (i.e., ~7.3 mL) based on the pouch geometry, the minimum volume is set by the starting liquid volume. As such, to maximize volume expansion ratio, we identified the minimum liquid volume required to complete a flip without full vaporization (i.e., 0.8 mL) and filled all pouches with this amount. The result is a maximum volume expansion ratio of 9.13, which maximizes the volume expansion within our design constraints.

2.2.1.3 Designed Compliance

Load-dependent compliance was designed into the roller frame to enable sufficient stiffness during operation to ensure robust locomotion but also provide sufficient softness to deform and not break in the case of an unexpected, large force. Under its body weight and light compressive loads, the combination of composite structures (carbon fiber beams, fiberglass plates) and dynamic hinges (Fig. 3D) render the roller functionally stiff (see Supplementary Materials, Fig. S17). This stiffness allows for repeatable lens positioning with respect to the sun and efficient transduction of energy from the pouch to the leg. However, under higher compressive loads, these hinges can either buckle flat (i.e., ~0°) or open (i.e., 180°) to accommodate the differing angular deflections in a compressed hexagon (see Supplementary Materials, Fig. S17). Finally, small pads of damping foam (McMaster

Carr, 86195K31) were added to the legs of the roller (Fig. 3D) to dampen any excess kinetic energy from flipping and maintain constant alignment with the sun.

2.2.2 Roller Demonstrations

2.2.2.0 Locomotion

We demonstrate our roller completing more than a full rotation using only sunlight (Fig. 9, Supplementary Video 1). A full rotation consists of six flips—requiring that each of the six legs open and close sequentially as a result of vaporization and condensation in the irradiated and non-irradiated states, respectively. To achieve this, the roller was placed outdoors in Santa Barbara, CA at a time of day when sunlight could be bent through the lenses onto the corresponding pouches for actuation. Thereafter, the roller was allowed to locomote autonomously and completed seven flips at an average speed of 0.764 cm s^{-1} using ~870 W m^{-2} of sunlight. The STAPAs powering the roller achieved an average efficiency of 0.0274% during operation with a standard deviation of ± 0.0176% (see Supplementary Text S15). The large standard deviation can be attributed to varying environmental conditions (e.g., wind speed) that affect heat losses.

Fig. 9. Demonstration of solar-powered locomotion. The robot was placed outdoors in Santa Barbara, CA and allowed to roll autonomously as it harvests sunlight. This composite figure illustrates the robot completing seven flips, rolling an average speed of 0.764 cm s^{-1} using roughly 870 W m^{-2} of sunlight (see Supplementary Video 1).

2.2.2.1 Compliance & Resilience.

The inherent compliance of the roller creates resistance to falls and mechanical crushing. We demonstrated that the roller can be compressed nearly flat, after which it immediately springs back to its original shape (see Supplementary Text S16). Further, the roller can endure substantial mechanical loading and continue its operation. We demonstrate this (1) by manually manipulating the roller mid-cycle and illustrating its ability to continue operation (Supplementary Video 2), (2) by kicking the roller down a set of stairs, after which the roller is able to continue rolling (Supplementary Video 3), and finally (3) by demonstrating a drop from 92 cm that the roller is able to sustain and then roll away from (Supplementary Video 4).

2.3 Discussion

Herein, we investigated the dominant sources of losses inherent to soft heat engines, identified accessible methods for improving their thermodynamic efficiency, validated these methods through experiment, and finally demonstrated the utility of these insights via a compliant roller capable of locomotion using only modest solar flux. In developing the theory, several simplifying assumptions had to be made. For example, our model assumes a constant heat loss coefficient throughout the work cycle of the STAPA; however, we have observed that the loss coefficient varies with deflection angle (see Supplementary Text S10). While convenient for calculation, these simplifications are likely partially responsible for differences in the magnitudes of trends between the theory and experiment observed in Fig. 2. We quantify the losses observed in our experiments and discuss their potential root causes in Supplementary Text S11. Future work might include theoretical models that include a higher number of parameters that are accurate the experimental system. However, the congruence of trends predicted by theory and observed in experiment confirm the validity of the three insights we propose for minimizing losses in soft heat engines.

We then sought to demonstrate the utility of these insights via a compliant roller capable of locomotion using only the modest flux of sunlight. The roller should be considered a proof-of-concept rather than a ready-to-deploy robot. At present, the

roller includes no electrical sensors, uses no feedback, and only operates when the sun is at an elevation angle of 30º ± 5º. A truly deployable robot might include sensors for solar-tracking and mechanisms for alignment with the sun and steering. Note, however, sunlight was chosen to demonstrate that our proposed three key insights can enable new functionality in soft robots—i.e., harvesting a universally accessible, low flux source of energy for locomotion. More generally, we believe the importance of the work is found in the foundation it lays for efficient use of STAPAs in applications beyond solar harvesting.

Insights from our analysis have the potential to catalyze a new generation of soft robots that interface with the human body as well as unpredictable natural environments. For example, minimizing losses in active prostheses and smart textiles that leverage soft heat engines [4] in turn minimizes the size of the requisite energy sources (e.g., batteries) and can extend operation times. In another example, soft robots with minimized losses have the potential to increase their power output (e.g., lifting) or can operate for longer time periods (e.g., locomotion). Moreover, our demonstration of an autonomous solar-powered roller made from simple, low-cost, and accessible materials and hints at possibilities for automation and exploration in resource-constrained environments or for high-volume production at low cost. Lastly, the unique requirements for robotics being delivered to extraterrestrial planets (e.g., robustness to vibration, light weight, resistance to corruption by static electricity) and the environmental conditions therein (e.g., longer sun exposure times, extreme

temperature swings, thin atmospheres) present unique opportunities in which STAPA-driven soft robots might thrive over their rigid counterparts.

2.4 Materials & Methods

2.4.0 Theoretical Model & Assumptions:

To analyze the impact of design constraints, operation modes, and materials on STAPAs, we model one as a control mass (i.e., system with no mass exchange) inside a piston and cylinder assembly (Fig. 10A) undergoing quasistatic operation. We assume all operations occur within the vapor dome (i.e., region of vapor-liquid coexistence), because full vaporization may damage the system if the heater is not completely wetted throughout operation.

We assume that temperature and pressure inside the control volume are homogenous and described by an effective temperature T and effective pressure P. The system operates between a minimum and maximum specific volume, measured with respect to the mass of the fluid, of v_{min} and v_{max}, respectively, and a pressure range between $P_{min} = P(T_{min})$ and $P_{max} = P(T_{max})$. Note that during single component phase change, pressure varies only with temperature. The temperature and pressure ranges considered in this analysis are determined by material and efficiency considerations.

At the piston, changes in internal fluid pressure due to liquid-vapor phase change drive volumetric expansion and compression. To expand, vapor pushes against the

piston, which is resisted by the load pressure (P_L), elastic pressure ($P_\mathcal{E}$), and dissipative pressure (P_D). The load pressure is the pressure exerted by an external load. Useful work is done to it. The elastic pressure restores the piston to the original position and comes from atmospheric pressure and the elasticity of the walls; this is modeled as a spring in Fig. 10A. The dissipative pressure comes from internal friction (i.e., hysteresis); this is shown as a damper in Fig. 10A.

A heater supplies heat to the fluid inside the STAPA and acts as the hot reservoir for the heat engine. When on, it supplies heat at a rate of $\dot{q}_{in}$. A portion of this is lost to the environment of temperature T_∞ through the walls either through direct heater wall contact or indirect contact via the fluid. The temperature of the heater, T_h, thus depends on the rate of heat loss and rate of work. For our analysis, we assume that our heater makes no direct contact with the walls.

The control mass undergoes a thermodynamic cycle consisting of four general processes (Fig. 10B). At point 1, an external load is applied to the actuator while heat is introduced to the system by way of a heater. From states 1 to 2, the system undergoes isochoric (i.e., constant volume) heating to build up pressure and overcome the added load; this step can be arbitrarily small, and no pressure-volume work is done. From 2 to 3, the system expands against pressure $P_{23}(v)$. We assume the heater remains on and that this process never rejects heat. At point 3, the system is at maximum volume and cannot, or is designed not to, expand further. Once maximum volume is reached, the external load is instantaneously removed. From 3 to 4, the heater is shut off and the system immediately undergoes isochoric

cooling—doing no work as even as pressure drops. From 4 to 1, a restoring force, $P_{41}(v)$, is enough to do work to the system—compressing it back to its initial state. These processes occur within the specific volume and pressure (or temperature) bounds of operations for the control mass. For the below analysis, we consider a rectangular version of this cycle (dashed black rectangle in Fig. 10B.), due to its relatively simple implementation with STAPAs.

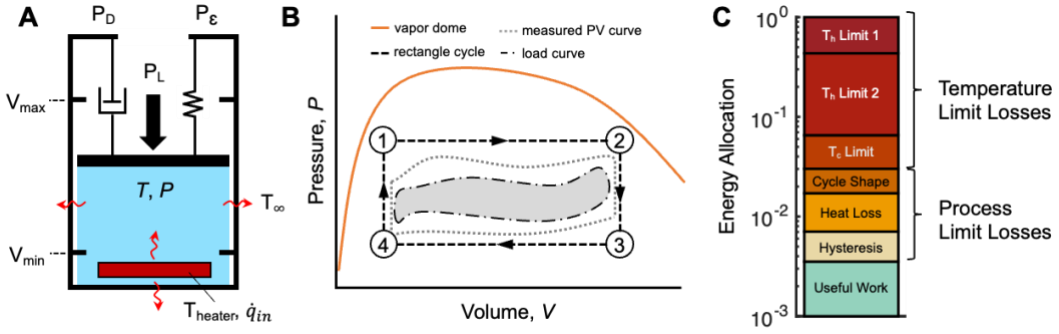

Fig. 10. Insights from a theoretical thermodynamic framework. (A) A schematic of a theoretical piston which represents a STAPA doing work. A liquid-vapor mixture of phase change fluid (blue rectangle) changes temperature (*T*), pressure (*P*), and (*V*) as heat is input into the system via a heater (T_{heater}) or rejected to ambient (T_∞). As volume changes, the piston head glides between a minimum and maximum volume state—i.e., V_{min} and V_{max}, respectively. To expand, vapor pushes against the piston head, which is resisted by the load pressure (P_L), elastic pressure ($P_\mathcal{E}$), and dissipative pressure (P_D). **(B)** A pressure-volume plot that illustrates simultaneous thermodynamic phenomena. The orange curve represents the saturation curve for the working fluid. The dark dashed curve represents the loading curve—i.e., the net pressure felt by the working fluid. **(C)** An example of energy allocation analysis. This analysis illustrates dominant sources of energy loss. Note that the y-axis uses a logarithmic scale.

2.4.1 Experiment: Actuator fabrication.

Bellows-like pouches were created by heat sealing Mylar film (WeVac, Vacuum Sealer Bags) with a disk of black conductive fabric (EonTex, NW170-PI-20) and working fluid (3M, Novec 7000) inside (see Supplementary Information). Mylar was chosen for its relatively good transmissivity (**Error! Reference source not found.**). B lack conductive fabric was chosen to serve as a flexible/soft heater with high wetted surface area. Novec 7000 was chosen for its low boiling point at ambient conditions (i.e., 34 ℃ at 1 atm), low toxicity and broad compatibility with soft polymer materials.

2.4.2 Experiment: Actuator testing setup.

A custom testing apparatus was fabricated to quantify the efficiency of a soft pouch under a variety of loading conditions (Fig. 11). As the working fluid is vaporized by the heater, the STAPA does pressure-angle work against a loaded hinge whose mechanical load can be programmed via the removal/addition of masses. Different loading conditions (i.e., expansion and compression curves observed in the pressure-angle cycles) could be programmed via a combination of an “offset mass” and a “constant-torque mass” (Fig. 11A, see Supplementary Text S7). To create work cycles in which positive work is done, the hinge is loaded with more mass (i.e., load) during the expansion than during the compression step.

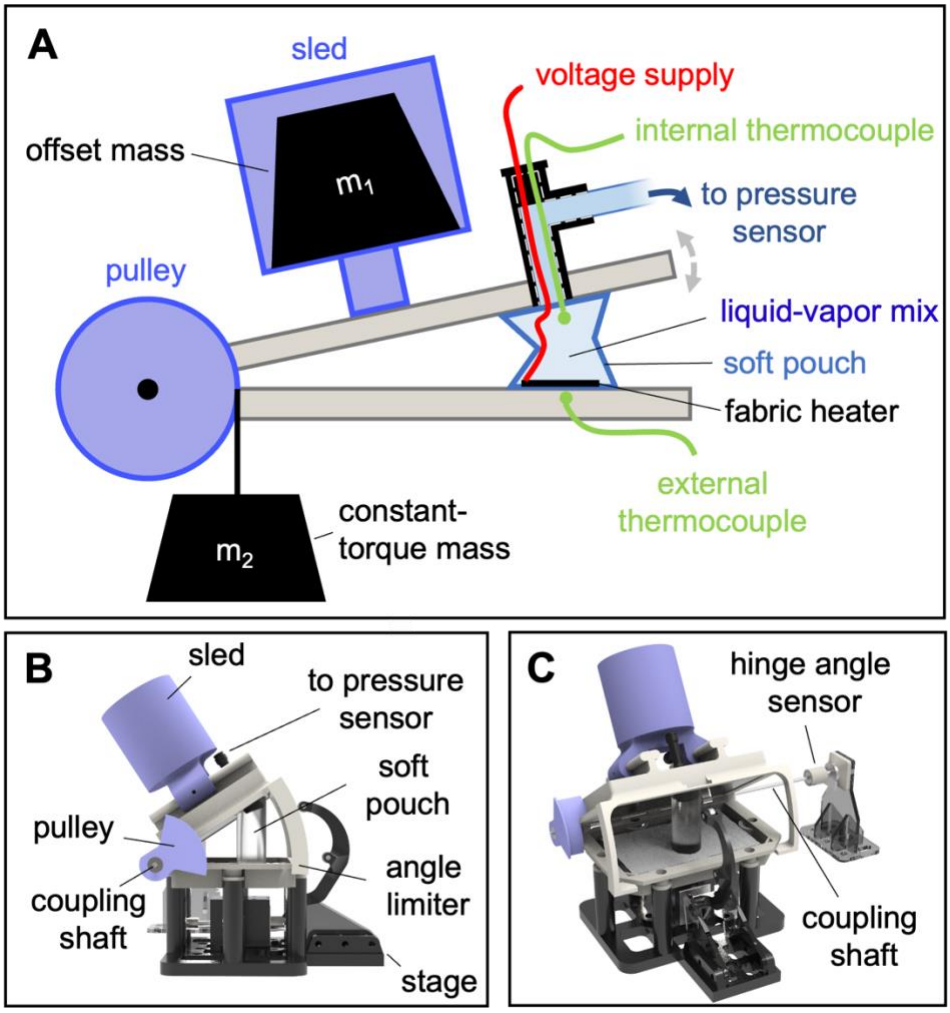

Fig. 11. Details of the experimental setup. (**A**) A schematic illustrating the testing setup mechanism. A soft pouch containing a conductive fabric heater and low-boiling point fluid (Novec 7000) does pressure-volume work against a loaded hinge. Voltage is supplied to the heater to incite liquid-vapor phase change, and thus pressure-volume work against the hinge. The combined load of the offset (m_1) and constant-torque (m_2) masses dictates the pressure-volume conditions of the loaded pouch. Varying the magnitude of the masses prior to expansion or compression steps of a work cycle results in a broad variety of curves (e.g., **Error! Reference source not found.**C). P ressure, temperature, power, and angle are measured using a pressure sensor, thermocouples, a power meter, and a potentiometer coupled to hinge shaft, respectively. (**B**) A 3D rendering of the setup illustrates the same principles in (A), with the addition of an angle limiter to prevent the pouch from doing work beyond the desired angle. (**C**) An isometric rendering of the setup illustrates a steel

shaft that rotates freely inside of bearings in the structure, but couples the rotating the hinge to a potentiometer for hinge deflection angle measurement.

To characterize the thermodynamic state of our system we measure pressure, hinge deflection angle, electrical energy supplied, and temperature (Fig. 11B,C). Pressure quantifies the internal vapor pressure of the pouch. Hinge deflection angle is linearly related to volume for most angles (see Supplementary Text S8) and was thus used as an accessible proxy. Electrical energy input is monitored and quantified using a power sensor. The mechanical work done by the pouch is calculated by measuring the torque required to complete a given cycle (see Supplementary Text S7). Unless otherwise noted, reports of efficiency are quantified by calculating the ratio of mechanical work output to heat input. Mechanical work is known by measuring torque-angle relationship for both the expansion and compression loads and integrating the area between the two.

Temperature inside of the pouch describes the state of the working fluid and temperature outside provides qualitative information about thermal gradients. Unless otherwise noted, all experiments were performed in a temperature-controlled room at ~20 $\pm$ 0.25 ℃. A lumped convection coefficient of the setup was calculated and incorporated into our theoretical calculations (see Supplementary Text S10).

2.4.3 Roller Fabrication.

The roller body is composed of six panels—i.e., 12 cm x 15 cm polyvinyl chloride (PVC) asymmetrical Fresnel lenses—framed by thin (4.5 mm x 1.1 mm cross section) carbon fiber beams. These lenses are made asymmetrical by cutting a commercially available Fresnel lens (Cz Garden Supply Store, 8.3" x 11.75" Fresnel Lens, Amazon.com) in half. The panels are joined by flexible hinges and to form a hexagon-shaped roller (side length, 12cm). These hinges were 3D printed from flexible filament (Ultimaker 2, NinjaFlex) and equipped with 28.6 N neodymium magnets (see “hinge magnets” in Fig. 7, K&J Magnetics B662). The dynamic hinges create maximum stiffness in the hexagon conformation, but compliance when deformed into other shapes (see Supplementary Text S14).

Each side is equipped with a Mylar pouch containing a disc of black fabric and ~0.8 mL of low boiling point fluid (3M, Novec 7000), backed by a 30 mm x 30 mm x 3.4 mm pad of polystyrene foam. Black fabric here was chosen for its broadband light absorptivity. During vaporization and condensation of the fluid, a hinged fiberglass leg deflects—flipping the roller as part of a rolling sequence. A thin piece of Nylon fabric serves as the hinge connecting the fiberglass leg to the roller body. A combination of latex bands and 10.3 N neodymium magnets (K&J Magnetics, B841) provide restoring force (see “hinge magnets” and “latex bands” in Fig. 7). All components of the roller are fastened to one another using cyanoacrylate glue (LocTite 40140), save for the flexible hinges which are adhered to the Fresnel lenses using flexible adhesive (LocTite 1360694).

2.4.4 Roller Locomotion Test.

The roller was placed outdoors at a time of day such that the collector (i.e., Fresnel lens) was perpendicular to the collimated rays of the sun. Thereafter, the roller was allowed to roll autonomously until completion of the test. Weather conditions (i.e., wind, solar flux, air temperature) were measured using a weather station (Ambient Weather Falcon WS-8480, see Supplementary Text S17 for details). The video and stills were taken using a mobile phone camera (iPhone 13 Pro).

III. Self-regulating photochemical Rayleigh-Bénard convection using a highly absorbing organic photoswitch

This chapter was adapted a publication in *Nature Communications* DOI: 10.1038/s41467-020-16277-7.

3.0 Abstract

We identify unique features of a highly absorbing negatively photochromic molecular switch, donor acceptor Stenhouse adduct (DASA), that enable its use for self-regulating light-activated control of fluid flow. Leveraging features of DASA's chemical properties and solvent-dependent reaction kinetics, we demonstrate its use for photo-controlled Rayleigh-Bénard convection to generate dynamic, self-regulating flows with unparalleled fluid velocities (~mm s-1) simply by illuminating the fluid with visible light. The exceptional absorbance of DASAs in solution, uniquely controllable reaction kinetics and resulting spatially-confined photothermal flows demonstrate the ways in which photoswitches present exciting opportunities for their use in optofluidics applications requiring tunable flow behavior.

3.1 Introduction

Autonomous control of liquid motion is vital to the development of new actuators and pumps in fluid systems. Recently, light has been recognized as a formidable tool for non-invasive, wavelength-selective, remote control over liquid motion with high spatial and temporal resolution. Recent studies have sought to harness light energy for mixing[48], [49], particle arrangement[50], [51], and actuation[5,6] in solution. Typical systems for such applications make use of photothermal plasmonic nanoparticles and complex nanostructures[7–10], electrochemically activated substrates[58], [59], or rely on interfacial control to drive fluids.[60]–[63] Though these current systems provide effective control over flow, autonomous control of fluid motion (i.e., without external manipulation) is inaccessible *via* the chemistries used in these approaches. Self-regulated fluid pumping is, in its current form, most commonly accomplished *via* the establishment of local gradients of solutes resulting from a chemical reaction.[64], [65] However, many of these systems are limited by the depletion of the chemical source which is used to generate flow, production of harmful byproducts, and their working environment. Self-regulation is advantageous where manipulation of flow is desirable without external manipulation or complex chemistry. As such, we investigate here how high-absorbing, negatively photochromic molecular switches might be used to overcome these limitations.

Generally, irradiating highly-absorbing particles or molecules in a solution locally heats the solution, and in turn can result in Rayleigh-Bénard convection, in which thermal gradients generate buoyancy-driven flow. However, in the case of such

photothermal Rayleigh-Bénard convection under constant, continuous irradiation (i.e., a constant rate of energy input) of an otherwise closed system, establishing a steady state requires negative feedback that retards the rate of Rayleigh-Bénard convection as the total energy in the system increases over time. In the case of a high-absorbing, non-bleaching dye or particle, where a photothermal gradient is established, the negative feedback is the heat loss to the surrounding environment due to heat transfer through the confining walls. Absent this external energy loss, there is no mechanism by which to dynamically decrease the amount of irradiant photon energy that is converted to heat (other than to externally decrease the intensity of incident light). By contrast, the use of negatively photochromic molecules, which can reversibly switch from high-absorbing and colored state to non-absorbing and clear state upon irradiation provides an internal negative feedback mechanism: as the light intensity increases, more bleaching occurs, which limits the total amount of irradiant energy that can be converted to heat and, therefore, produce a temperature gradient. These negative feedback properties critically rely on the reversibility of the bleaching reaction and its ability to establish and sustain a concentration gradient of the photothermal material and enable spatially varying absorbance in solution that is dynamically maintained. As such, self-regulation can be established and maintained internally by the photoswitching properties of the molecule. Furthermore, variable extrinsic factors (e.g., concentration) known to alter characteristics of the photoreaction (e.g., reaction rate) serve as control “knobs” that, in turn, also enable control over the behavior of the

Rayleigh-Bénard convection by dynamically tuning the bleaching profile of the photochrome.

The opportune development of an emerging class of negative photoswitches, donor-acceptor Stenhouse adducts (DASAs), with highly tunable reaction kinetics in a range of solvents allows us to understand and exploit the factors that govern self-regulated fluid flow. DASAs undergo a transformation from a colored, extended open form to a bleached, compact, closed form upon irradiation with visible light (Fig. 1a) and have been leveraged by us[66]–[69] and others[70]–[74] for their synthetic modularity, wavelength tunability, and negative photochromic properties. In addition, previous studies of DASAs in solution have shown that their switching kinetics are highly dependent on the polarity of the solvent, concentration, and the architecture of the donor and acceptor groups.[68], [69], [75], [76] Herein, we report how combining our understanding of DASAs' photoswitching kinetics with an ability to control physicochemical conditions such as molarity, solvent, and light intensity enables both controlled and self-regulating fluid motion in organic solutions. The system operates as follows: by irradiating a solution containing DASA with visible light (Fig. 1b) a controlled bleaching front (i.e., a growing non-absorbing region) is generated, which enables the local manipulation of solution temperature (Fig. 1c) which in turn incites a time-varying thermal gradient and thus Rayleigh-Bénard convection (Fig. 1d). These convective flows are inherently self-regulated via the complex interplay between the photochemical conversion kinetics and high absorption, enabling a novel method of control over fluid motion. The careful manipulation of the reaction kinetics of a photoswitch uniquely enables the bleaching front progression to dictate

the flow behavior observed in solution. This degree of control is presently inaccessible via other methods and, thus, using a negatively photochromic molecular photoswitch such as DASA opens new avenues for the use of high-absorbing photoswitches in applications for self-regulated fluid pumping and mixing.

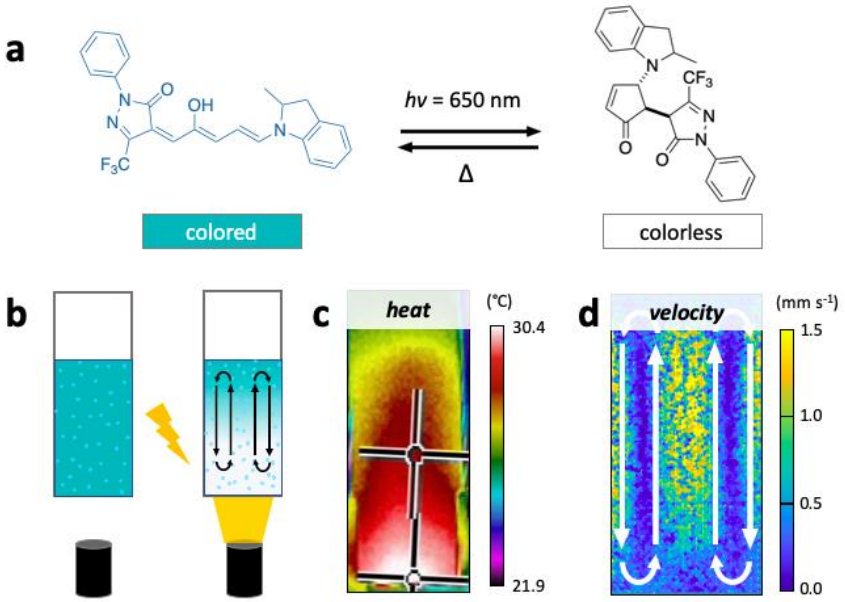

Fig. 1. Donor-acceptor Stenhouse adducts for photothermal control of fluid flow. a, DASA-CF_3-PI switching under visible light irradiation from an extended, colored, open form to a compact, colorless, closed form. **b**, Schematic of experimental setup for convective particle tracking. Light shone on the bottom of a quartz cuvette causes DASAs to switch to the colorless form, while also generating **c**, heat gradients and **d**, fluid flows due to convection in toluene.

3.2 Results

3.2.0 DASA switching kinetics.

In order to drive dynamic, photochemically-regulated fluid flows we focused on the newly developed third generation DASA bearing a CF3 pyrazolone-based acceptor and a 2-methyl indoline donor[69] (referred to hereafter simply as DASA-CF3-PI) due to its high molar absorptivity and tunable forward and reverse switching kinetics in organic solvents. Though DASA-CF3-PI switches from its colored, open form to a bleached, closed form (Fig. 1a, 2a) in both toluene and chloroform, the tunability of this behavior arises from solvent- and concentration-dependent photoswitching kinetics. The following studies highlight the dynamic control of flow behavior by varying solvent, concentration, and light intensity. Specifically, this DASA derivative exhibits a faster backward photoreaction in toluene than in chloroform, as evidenced by reverse rates of reaction (kback) of 0.046 s-1 and 0.035 s-1 in toluene and chloroform, respectively, at 10 μM (Fig. 2b, Supplementary Note 1). This difference in kback is intensified at high concentrations—as DASA-CF3-PI exhibits a stronger concentration-dependence in toluene than in chloroform—leading to an even faster back reaction.[77] The bleaching front velocity (Fig. 2c) and solvent-dependent switching combined with DASA's high molar absorptivity (Fig. 2d), can be exploited to generate sharp thermal gradients at the interface between the bleached and non-bleached portions of the solution that drive convective flows (Fig 2a). Varying light intensity also has an effect on the magnitude of observed thermal gradients.

3.2.1 Molar absorptivity drives thermal gradient.

In its colored form, the high molar absorptivity of DASA enables the effective conversion of light energy to heat, which in turn drives fluid motion. Using UV/Vis spectroscopy, we determined the molar absorptivity of DASA-CF3-PI in toluene, chloroform, and dichloromethane to be 118,820 ± 516 M-1 cm-1, 88,867 ± 300 M-1 cm-1, and 129,190 ± 490 M-1 cm-1, respectively (Supplementary Fig. 2). For comparison, we determined the molar absorptivity of highly-absorbing, commercially available organic dye Nile Red to be 38,000 M-1 cm-1 and that of a non-bleaching DASA analog to be 70,500 M-1 cm-1 (Supplementary Fig. 3). To demonstrate the dramatic changes in temperature enabled by the absorbance of DASA-CF3-PI, solutions of varying concentration in chloroform were irradiated for ten minutes using a 214 mW cm-2 white light source (Fig. 3a). From these experiments, we observe 2 °C temperature changes in solvent without dye due to the heat from the light source and up to 12 °C in the presence of DASA-CF3-PI (Fig. 3b). Furthermore, infrared imaging illustrates a temperature gradient established throughout the solution within tens of seconds of irradiation (Fig. 3c). Above 2 mM, however, increasing the DASA-CF3-PI concentration fails to further increase the solution temperature, as a rapid back reaction impedes the penetration of light and thus absorbance of the small molecules responsible for generating heat.

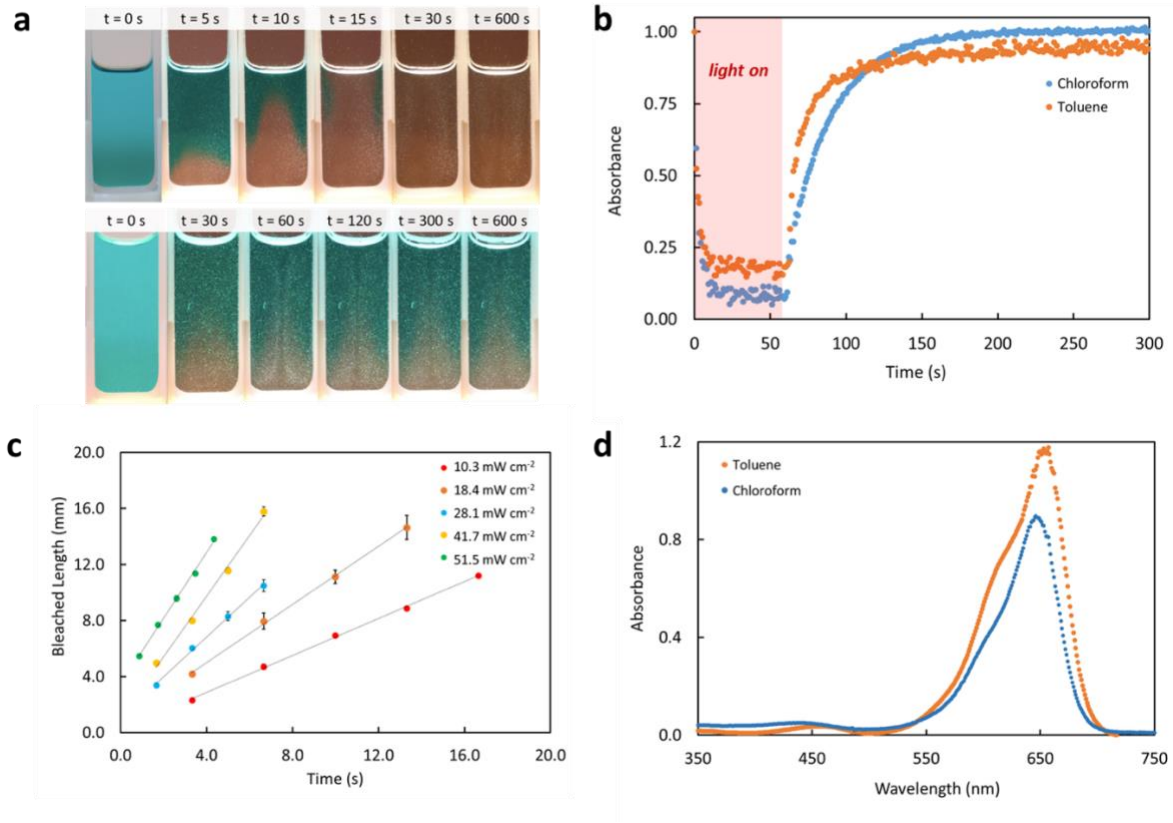

Fig. 2. Photochemical properties of DASA-CF_3-PI in chloroform and toluene. a, Bleaching front progression through 0.25mM DASA-CF_3-PI in chloroform stabilized with 0.75% ethanol (top) and toluene (bottom) irradiated with 25 mW cm^{-2} light. **b**, Reversible switching kinetics of DASA-CF_3-PI in chloroform and toluene at 10 μM. **c**, Bleaching front length versus time for 0.125mM DASA in chloroform, where the slope provides a measure of the front velocity. **d**, Absorbance of DASA-CF_3-PI in toluene and chloroform at 14 μM.

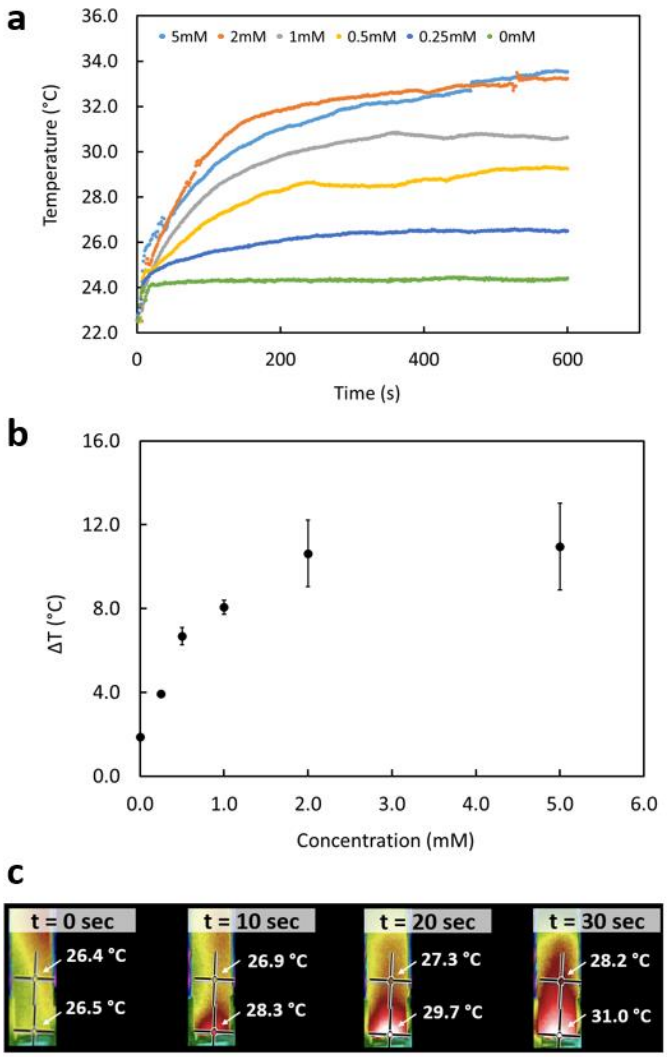

Fig. 3. Photothermal temperature changes due to DASA-CF_3-PI in solution. a, Average heating of chloroform solutions with varying concentrations of DASA-CF_3-PI using 214 mW cm^{-2} white light. **b**, Change in temperature as a function of DASA-CF_3-PI concentration from *t*=0s to *t*=600s. Average values are plotted with error bars calculated from the standard deviation of replicate measurements (*N*=3). **c**, Thermal images of heat gradient established in the first 30 seconds of irradiation of 2mM DASA-CF_3-PI in chloroform, as measured with an IR camera. Note, the camera's auto-adjust feature prevents the use of a consistent legend for the temperature, so numeric values for two locations are shown.

3.2.2 Control of bleaching front.

Using the experimental configuration depicted in Supplementary Fig. 1, we found that solutions of DASA-CF_3-PI in chloroform at low concentrations (e.g., 0.25 mM) exhibit a well-defined bleaching front (i.e., a growing zone of bleached solution) that propagates through the entire volume of the solution similar to those previously studied.[78] However, this behavior is different from that in toluene, where the bleaching front begins to propagate through the solution but is then halted at some non-zero height due to a competitive back reaction (Fig 2a). Understanding the bleaching behavior is critical, as DASA's absorbance—and thus, its ability to generate heat—falls steeply once it has transitioned from the colored to colorless state (Fig. 2b). The time- and length-scales over which these solutions bleach can be analyzed to predict characteristics of the flow behavior and tune the system for self-regulation.

The bleaching profile corresponds to a sharp gradient in concentration of the open form of DASA-CF_3-PI between a bleached zone (A) and unbleached zone (B). Because of the large disparity in photoabsorption efficiency between the open and closed forms of DASA-CF_3-PI (Fig. 2b), the heat generation that drives the convective flow is primarily produced in the unbleached (i.e., colored) zone where the concentration of the open form is significantly greater than the closed form. As such, we expect that the total rate of energy input that drives photothermal convection will be proportional to the average net rate of photoreaction in the bleached zone and the fraction *f* of the container volume occupied by the unbleached zone, $f = (H - h_I)/H$, where H is the total fluid height and h_I the height

of the bleaching front (i.e., colorless zone). Therefore, to a first approximation, we also expect that the time variation of the magnitude of the maximum convective velocity will qualitatively track with the speed at which the bleaching front advances—i.e., $dv_{max}/dt \propto df/dt \propto -dh_I/dt$. It is therefore of critical importance to understand the kinematics of the bleaching front, and the influence of the various coupled transport processes present in the system.

The velocity of the front depends on the net rate of reaction (forward and backward), mass transport to and from the bleaching front, and convection due to flow and diffusion. By restricting the analysis to only the bleaching front itself, we expect that concentration gradients in the bleached and unbleached regions will be small, such that the diffusive flux is negligible compared to the convective flux. Making this and other simplifying assumptions and solving for the interface velocity yields Eq. (1) (full derivation, Supplement Note 2).

$$\boldsymbol{v}_I = \boldsymbol{v}_{fluid} + \frac{\delta r_{I,open}}{\Delta N_{I,open}} \tag{1}$$

Here, $\Delta N_{I,open} = N_{A,open} - N_{B,open}$ is the change in open DASA-CF_3-PI molar concentration across the bleaching front, δ is the thickness of the transition in concentration between the bleached and unbleached regions, and $r_{I,open}$ is the net rate of the reaction, defined in Eq. (2).[77]

$$r_{I,open} = \sigma\left(N_{I,open}\right) \cdot \phi_{OC}\left(N_{I,open}\right) \cdot I(h_I) \cdot N_{I,open} - k_{back}\left(N_{I,open}\right) \cdot \left[N_o - N_{I,open}\right] \quad (2)$$

Note that the forward reaction rate is governed by the absorption cross-section σ, the quantum efficiency for photoconversion between the open and closed form $\phi_{OC,}$ the irradiation intensity at the bleaching front I, and the concentration of open DASA-CF_3-PI at the bleaching front $N_{I,open}$. The back reaction is dictated by the rate constant of the backward photoconversion k_{back} and the concentration of the closed form of DASA-CF_3-PI ($N_o - N_{I,open}$). The reverse rate constant is calculated by fitting the experimental absorbance recovery of DASA after irradiation is ceased to a decaying exponential function.[77] Substituting Eq. (2) into (1) results in Eq. (3).

$$\boldsymbol{v}_I = \boldsymbol{v}_{fluid} + \frac{\delta}{\Delta N_{I,open}}\left\{\sigma \cdot \phi_{OC} \cdot I(h_I) \cdot N_{I,open} - k_{back} \cdot \left[N_o - N_{I,open}\right]\right\} \quad (3)$$

Eq. (3) reveals the unique features that are imparted to the photothermal convection due to a reversible photochemical reaction such as that enabled by DASA-CF_3-PI. When k_{back} is small (e.g., in chloroform) the velocity of the bleaching front (which is distinct from, but is influenced by, the underlying convective fluid velocity, as indicated in Eq. (1)) is always positive and the bleaching front will grow to fill the volume of the container. Once completely bleached, no further energy due to photothermal processes is generated—allowing the thermal gradient to dissipate

and convective flow to be “turned off.” By contrast, if k_{back} is sufficiently large (e.g., in toluene) the location of the bleaching front can reach a dynamic steady state dictated by the self-regulating balance between 1) the photothermal convection and forward reaction in the unbleached zone, and 2) the back reaction in the bleached zone. Thus, using toluene and chloroform, we demonstrate distinct flow behaviors that take advantage of differences in DASA’s back reaction rates. Unlike other photothermal systems, DASA’s solvent-dependent back reaction kinetics offer unique modular control over dynamic and self-regulating flows in solution.

3.2.3 Nonlinear relationship between concentration and fluid velocity.

Examining the fluid motion in quartz cuvettes containing identical concentrations of DASA-CF_3-PI to those used in the temperature studies, we observed a nonlinear relationship between the strength of convection at early times and DASA-CF_3-PI concentration. This relationship arises as a result of the coupled relationship between the back-reaction kinetics of DASA-CF_3-PI and Beer’s Law. As solutions containing DASA-CF_3-PI are irradiated with visible light, the drastic changes in temperature depicted in Fig. 3a incite buoyancy-driven Rayleigh-Bénard convection. The strength of this convection can be analyzed by quantifying the speed of flows generated in solution using particle image velocimetry (PIV) to track the motions of neutrally buoyant silica spheres (average diameter = 10 μm). Specifically, 400 μL of solution was pipetted into a cuvette, allowed to settle in the absence of light, and then illuminated from below and recorded using a digital camera (Supplementary Video 6). Velocity fields were then calculated from the video using open source PIV software (Supplementary Figs. 4, 5).[79] These experiments allow us to quantify

DASA's remarkable ability to increase fluid motion in a given solution to several mm s^{-1} using only millimolar concentrations of DASA-CF_3-PI and commercially available solvents.

Although DASA demonstrates efficient photoswitching capabilities in both toluene and chloroform at low concentrations, the rate of back reaction drastically increases above an optimal concentration.[80] This increased rate implies the rapid reversion of DASA-CF_3-PI molecules from a closed, colorless to an open, colored form even in the presence of constant light. With most of the species in the high-absorbing open form, a masking effect is observed (Fig. 4a) which limits light penetration in the depth of the solution and thus the population of irradiated/switched species. This effect is reflected in the PIV analysis as a continuous decrease in maximum fluid velocity with increasing concentration of DASA-CF_3-PI (Fig. 4b). As a result, there exists an optimal concentration for which light can fully penetrate a solution to establish appreciable convective flow. We estimate this concentration to be 0.5 mM, where the convective flow reaches maximum fluid velocity of ~3.1 mm s^{-1}. While differences in experimental conditions make direct comparison challenging, this fluid velocity is orders of magnitude higher than those reported for common plasmonic particle systems which sustain micrometer per second velocities at similar photon fluxes.[54], [61] These experiments establish that light attenuates exponentially as the concentration of the absorbing species increases, and highlight concentration as yet another tunable parameter by which fluid velocity may be controlled.

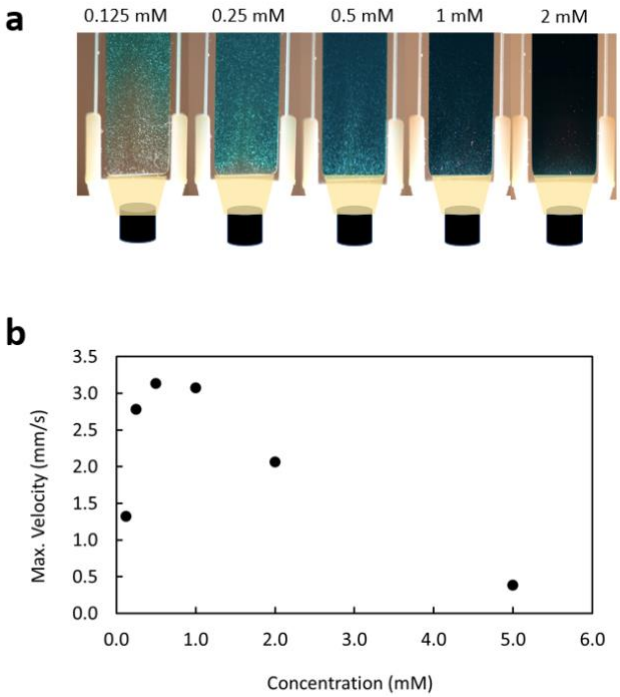

Fig. 4. Non-linear concentration dependence of particle velocity. a Concentrations ranging from 0.125 mM to 2 mM of DASA in toluene shown from left to right after 10 s of irradiation with 46 mW cm^{-2} light. **b**, Particle velocities as a function of concentration show the nonlinear dependency on concentration. Above 0.5 mM, the dark solution exhibits a masking effect that limits light penetration and, as a result, limits particle velocity.

3.2.4 Bleaching front dictates self-regulating fluid motion.

The nonlinear coupling of both solvent- and concentration-dependent photoswitching kinetics and high absorption properties enables unprecedented self-regulation of photothermal flows. Irradiating a solution of a given concentration and solvent incites a photothermally-driven flow which creates a dynamic equilibrium at the bleaching front in which the consumption of photoreactants is stoichiometrically replenished by the flux of regenerated photoreactants from the bleached zone. To illustrate this balance, we present two distinct self-regulating flow behaviors using 0.25 mM solutions of DASA-CF_3-PI in chloroform and toluene, respectively, irradiated using variable light intensity (Supplementary Fig. 6, 7).

In chloroform, an effective self-extinguishing behavior enabled by the careful tuning of the reaction kinetics of DASA-CF3-PI dictates the self-regulating flow behavior. Specifically, the rate of forward reaction is significantly greater than that of the reverse reaction—allowing the bleaching/photoswitching front to propagate through the solution unimpeded. As such, the bleached zone will eventually grow to fill the fluid volume, and the photothermal convection will cease after the thermal gradient dissipates—providing an effective “off-switch” for the photothermal convective flows, even as the light remains on (Fig. 2a, 5c). The time at which the “switch” occurs can be approximated from the bleach front velocity using Eq. (3) and changes in temperature. In the first eight seconds, the temperature of the solution rises as the bleaching front progresses through the cuvette (Fig. 5b, inset). At roughly the same time (~10 seconds), the maximum velocity and the maximum temperature difference are achieved. The brief, initial rise in temperature (Fig. 5b,

inset) is due to the high absorbance of DASA. However, as the solution bleaches (Fig. 5a) and the light input remains constant, the temperature gradually decreases and eventually plateaus. This characteristic behavior in chloroform—i.e., a steep rise followed by a decrease in maximum velocity and temperature—occurs irrespective of light intensity (Supplementary Fig. 7), although the intensity variations enable control of fluid flow dynamics. Increased light intensity leads to faster absorption and thus higher peaks in maximum velocity, but also a faster bleaching of the DASA solution. This repeatable behavior combined with control over tunable parameters (e.g., light intensity), make this type of switch uniquely amenable to systems in need of dynamic pumping under constant light irradiation and/or spatially precise zones of light penetration. The self-extinguishing behavior is achieved without additional stimuli or changes in concentration and can thus be leveraged for applications that require a fluidic feedback loop.

By contrast, in toluene, where k_{back} is sufficiently fast and $N_{I,open}$ is large everywhere, the front accelerates due to both the large net forward reaction and induced photothermal convection due to absorption by the open form. As the rate of the forward reaction (dictated by the quantum yield of DASA-CF_3-PI in toluene) is less than the rate of back reaction, however, the convective fluid velocity term (v_{fluid}) is balanced by the reaction velocity term. This balance results in a static bleaching front (i.e., $v_I = 0$, see Fig. 5a), which in turn allows for a steady state thermal gradient, and thence a constant fluid velocity that is maintained over ten minutes (Fig 2a, 5c). In measuring the temperature changes in the system, we

similarly find an initial increase in temperature of approximately 0.6 °C within the first two minutes that rapidly stabilizes to a steady-state value for over ten minutes of study. This self-regulation is uniquely imparted by the reversibility of the photoreaction of the DASA-CF_3-PI system and a matching of forward and backward reaction kinetics. Other high-absorbing dyes and DASAs are presented for comparison (Supplementary Figs. 8, 9) to demonstrate the rapid rate and magnitude of convective flow uniquely imparted by using a negative photoswitch with tunable backward kinetics. This second characteristic fluid behavior—i.e., a dynamically stabilized fluid velocity—is amenable to fluid systems in need of controlled, constant velocity. Further, the magnitude of the velocity plateau can be adjusted by tuning the light intensity (Supplementary Fig. 7).

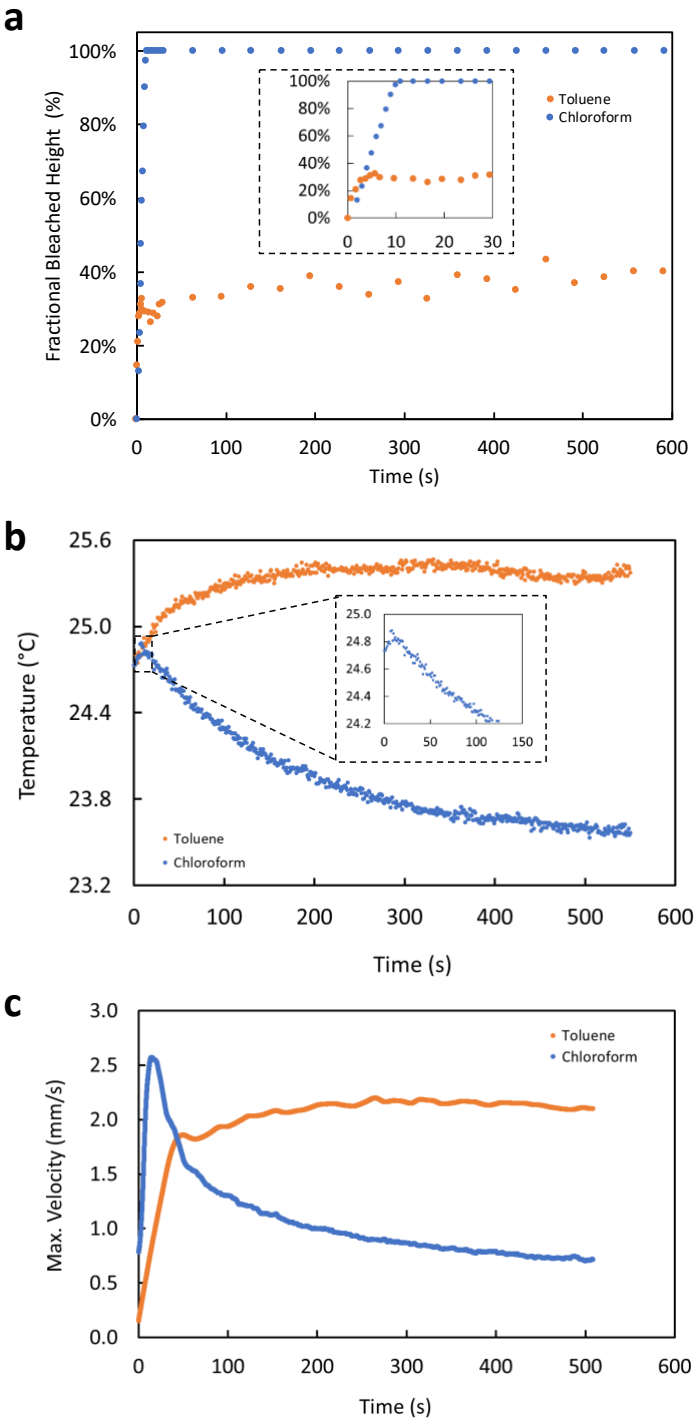

Fig. 5. Comparison of fluidic and thermal behavior of 0.25mM DASA in chloroform and toluene irradiated with 46 mW cm^{-2} white light. **a**, Percent of bleached volume (i.e., height of the bleach front / total wetted length) versus time. Inset depicts the same curves from 0 to 30s. **b**, Temperature changes over time for toluene and chloroform. Inset depicts the initial spike and then

decline in temperature exhibited by DASA in chloroform. **c**, Maximum velocity vs. time plots illustrate characteristic velocity trends. See Supplementary Note 3 Percent of bleached volume (i.e., height of the bleach front / total wetted length) versus time. Inset depicts the same curves from 0 to 30 s.

3.2.5 Localized fluid motion.

By localizing the light intensity to a point of interest, we create a pathway by which particles can be advected via a spatially addressed photothermal gradient. To demonstrate this effect, we show the locally directed motion of particles using a red LED (λ = 617 nm, 21 mW cm^{-2}) to illuminate a 0.25 mM solution of DASA-CF3-PI in chloroform. Visual inspection of particle trajectories demonstrate that we can direct particles along the path of light propagation with just a few seconds of irradiation (Fig. 6, Supplementary Video 7). Due to a heat-induced decrease in local fluid density, buoyancy effects enable spatially-localized flow, irrespective of the spatial orientation of the light source. As a result of these buoyancy effects, we see from the bleaching that an upward flow is established within seconds after the light source has been removed. The fast reverse kinetics allows for the color to return almost immediately, thus enabling the use of the same solution to direct particles along multiple trajectories.

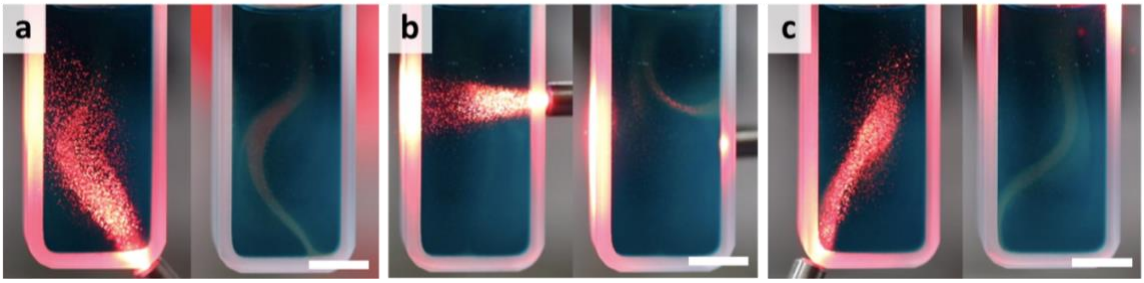

Fig. 6. Spatially precise convective flows. a-c (left panels), Irradiating one portion of the cuvette using a red LED light. **a-c** (right panels), convective flows that ensue due to irradiation. The same solution was used for all experiments depicted above (Supplementary Video 7).

3.3 Discussion

By leveraging our understanding of DASA's reversible switching kinetics, we have demonstrated the ability to harness the photochemical response of a negatively photochromic switch to control bleaching and consequently photo-thermal gradients in differing solvents to drive programmed fluid motion. The tunable rate of the back reaction of DASA offers a unique handle by which we can control the self-regulatory properties of the system. Additionally, we can estimate the timescale over which a maximum velocity may be achieved as a function of the relative rates of the photochemical reaction and the propagation of the thermal gradient it produces. As such, we unlock a powerful mechanism by which fluid motion can be controlled using a negatively photochromic molecular switch with highly tunable reaction kinetics. For solvents in which DASA-CF_3-PI has a fast back reaction, the dynamic steady state achieved in solution produces a self-regulating thermal gradient that can drive fluid flow at a constant velocity. In solvents in which DASA bleaches

rapidly and has a slow back reaction, it enables as an effective “off-switch” after the solution has entirely bleached and the thermal gradient dissipates. To our knowledge, this is the first system to demonstrate a self-regulatory degree of control as a result of a photochemical reaction. With careful tuning of reaction kinetics, other high-absorbing negatively photochromic switches can be similarly tailored, providing access to self-regulating control using different wavelengths of irradiation and solvents (Supplementary Fig. 9). This versatile control and tunability provides unrivaled access to fluidic applications requiring high fluid velocities (~mm s^{-1}), controllable fluid behaviors, and operation in a range of chemical environments—all achievable using low intensity visible light.

3.4 Materials & Methods

Chemical selection. Chloroform stabilized with 0.75% ethanol and toluene (99.8%) were purchased and used without further purification from Sigma Aldrich. Donor-acceptor Stenhouse adducts were synthesized as described in the procedure previously reported in literature.[69] For each experiment, the compound was dissolved in solutions from fresh bottles of chloroform stabilized with ethanol or toluene and diluted to the desired concentrations.

Light source. A Schott Ace 150 W fiber optic white light source was chosen for all experiments herein due to its broad coverage of the absorbance spectrum of DASA-CF_3-PI and other molecules discussed in this work (Supplementary Fig. 3). In

addition, it supplied light fluxes otherwise inaccessible with the use of LEDs available to us.

Characterization. Molar absorptivity of photoswitches and dyes were calculated using spectra obtained with UV/Vis spectrophotometry in triplicate for five concentrations of dye/switch in solvent. Each stock concentration of DASA was prepared 24 hours in advance in order to ensure that the photostationary state was reached. All measurements were taken using a standard quartz cuvette with 1 cm pathlength. The photoinduced optical absorption kinetics were measured using a pump-probe setup following previously reported procedures.[69]

Temperature analysis. Heat changes were obtained using a Phidget 4-Input Temperature Sensor in conjunction with the K-Type Teflon Bead Probe Thermocouple (accurate to ± 2 °C). Temperatures were measured at the top, middle and bottom of the cuvette to calculate the absolute and temperature differentials over the course irradiation. Infrared images were obtained using a FLIR E60 IR camera accurate to ± 2% of reading.

Particle tracking and analysis. For all particle tracking experiments, neutrally buoyant hollow spherical silica particles (Davg = 10 μm, TSI Inc.) were added to 400 μL of solution in a quartz cuvette (path length 2 mm, inner dimensions: 40 x 12 x 2 mm^3). Samples were irradiated 2 cm from the bottom at which distance the maximum irradiance was determined to be 214 mW cm^{-2}. All samples were

irradiated with Schott ACE Halogen Light Source with intensities determined using Field Max II TOP Laser Power Energy Meter. Videos were then divided into grayscale images using MATLAB code and analyzed using open-source particle image velocimetry software (see SI, “Experimental Section”).

IV. Engineering crack tortuosity in printed polymer–polymer composites through ordered pores

This chapter was adapted with author permission from *Materials Horizons* DOI: 10.1039/D0MH00331J.

4.0 Abstract

Nature offers a wealth of composites that exploit hierarchically organized stiff-soft motifs to achieve impressive mechanical properties that have long inspired materials design. Despite their desirable properties, natural materials are challenging to replicate due to their finely arranged and interfaced domains with distinct compositions/properties. While multimaterial 3D printing offers a promising route for emulating the structure, composition, and performance of such natural materials, state-of-the-art processes to produce multimaterial parts are prohibitively complex, costly, and slow for wide adoption by researchers. We present a new approach: by leveraging solution mask liquid lithography (SMaLL), a recently-developed light-controlled single-step multimaterial printing process, we create polymer-polymer composites that capture the key features of porous and multiphasic natural materials. We print structures comprising a stiff exterior surrounding a soft, porous core that are naturally bonded at molecular scales, eliminating defects and suppressing delamination at the interface. Through varying the size and packing of the pores, materials that undergo dramatic crack deflection can be produced. These

findings offer design rules for creating resilient polymer-polymer composites while demonstrating the potential of SMaLL for manufacturing mechanically complex materials.

4.1 Introduction

Nature is replete with materials that exhibit mechanical properties that are desirable, yet challenging to emulate. For example, simultaneous toughness and strength can be achieved by using strong interfaces to join soft (e.g., biopolymer) and hard (e.g., mineral) domains[81]–[83]. Despite knowledge of these motifs, synthetic strategies for replication/emulation remain inaccessible via traditional manufacturing methods due to the complex synthesis of constituent materials, their hierarchical organization, and a lack of robust techniques to couple mechanically and chemically distinct material domains. The ability to precisely control the structure, composition, and interfaces[84], [85] in multimaterial composites is vital for developing useful synthetic mimics.

New methods for polymer-polymer composite fabrication offer attractive routes for such synthesis—providing control over composition, processability, and manufacturability. For example, researchers have demonstrated enhanced mechanical properties by interfacing macroscopic elastomer structures[86], [87] and woven fibers[88], [89] with polymer gel networks. However, the stepwise synthetic strategies (e.g., casting) used in these works fail to replicate the fine structure of many natural materials. To achieve these demanding designs, much attention has been given to multimaterial 3D printing, which has been used to produce structures that draw bio-inspiration from subjects such as mantis shrimp claws[90], nacre[91],

bone[92], and a suite of other desirable natural materials[93], [94]. Yet even mature multimaterial 3D printing technologies suffer from significant drawbacks such as cost, complexity, and slow build rates that hinder greater exploration of bio-inspired structures. While a number of new strategies for the rapid production of 3D printed parts15–18 have recently been introduced, these technologies often rely on the use of a single resin stock and thus are incapable of producing multimaterial parts without the need to stop a print to exchange resins. Generally, single-source approaches can be altered for multi-material printing capabilities via variable light intensity[95], aligned filler particles[96], or microfluidic printheads[97]. However, the materials properties of the printed products are usually dictated and/or limited by a single curing chemistry.

4.2 Results

4.2.0 SMaLL: A Novel Printing Technique

To address these shortcomings, a new approach was developed, solution mask liquid lithography (SMaLL), that uses different wavelengths of light to control localized curing chemistries, enabling one-step multimaterial 3D printing.[98] SMaLL boasts rapid print speeds (50 cm h^{-1}), high lateral resolution (~100 µm), and importantly the ability to generate polymer-polymer composites with spatially specific and well-defined mechanical properties. As such, SMaLL is uniquely positioned to enable the study of nature-inspired composites with finely-featured and mechanically distinct (stiff-soft) domains. Here, we exploit this advantage to design and test

composites composed of a stiff outer layer, soft interior core domain, and controlled pore packing / distribution. Our findings demonstrate that the high fracture-resistance of porous natural composites can be captured in such synthetic mimics and moreover, reveal trends that can be generalized for the design of resilient polymer-polymer composites.

The key innovation in our manufacturing technique is that the single resin used in SMaLL can undergo orthogonal curing reactions triggered by exposure to different wavelengths of light. Here, green (530 nm) and blue (470 nm) light are used to induce different photopolymerizations, resulting in radical and radical plus cationic cured (crosslinked) networks, respectively (full details of formulations and printing conditions can be found in the Supporting Information). Green wavelengths excite the HNu_{535} photosensitizer, triggering solely the radical polymerization of methyl acrylate (MA) monomers and triethylene glycol diacrylate (TEGDA) crosslinkers, while blue light excites the camphorquinone (CQ) photosensitizer, triggering the dual curing of 3-ethyl-3-oxetanemethanol (OXA) monomers and 3,4-epoxycyclohexylmethyl 3,4-epoxycyclohexanecarboxylate (ECC) crosslinkers as well as MA and TEGDA through cationic and radical curing (Fig. 1a,b). Importantly, a small amount (~5 wt%) of network compatibilizer, 3-ethyloxetan-3-yl)methyl acrylate (OXA-A), with both acrylate and oxetane functionalities, is used to prevent phase separation between the radical and cationic networks formed during exposure to blue light. After printing, the samples are swollen several times in acetone/isopropanol, and are subsequently dried, to remove any unreacted molecules. This strategy of dual-wavelength control has recently been extended to

operate under UV and visible light, highlighting the flexibility of orthogonal photochemistries for simplified multi-material printing.[99] Critically, the wide range of available polymer and curing chemistries provides a broad palette for materials design, thus enabling a number of tunable properties to be captured in the printed composites.

In addition to providing wavelength-selective polymerization and crosslinking, SMaLL provides exceptionally fast and high-resolution printing through the addition of absorbing species (solution masks) overlapping in absorbance with the photosensitizing species. By using photochromic molecules that switch from highly-absorbing to inert (transparent) states upon light absorption as solution masks, well-defined photobleaching fronts 24–26 are forced to move through the resin under the control of a user-defined light field, thus allowing for the production of complex multimaterial samples without the need of a moving build stage. In this work, two diarylethene switches, 1,2 - bis(2-methyl-1-benzothiophen-3-yl)perfluorocyclopentene (DAE530) and 1,2-bis(3-methyl-1-benzothiophen-2-yl)perfluorocyclopentene (DAE470), were mixed with the resin described above (Fig. 1a) to mask –and thereby control the propagation of– green and blue light, respectively. Exposure to green light for and subsequent dialysis and drying afforded elastomeric radical-only networks with elastic moduli of 470 kPa and ultimate strains of over 1000%. In contrast, exposure to blue light led to stiffer, and much less extensible, materials with elastic moduli of 950 kPa and ultimate strains of approximately 100% (Fig. 1c). Using color templates comprised of blue and green regions and a commercially-available projector, materials consisting of both

components can be readily produced in a single step (see Supporting Information Section 1E). Importantly, this single step fabrication creates multiphase composites without the need to bond two dissimilar materials and thereby minimizes the presence of defects at the interface that tend to nucleate cracks and undermine strength.

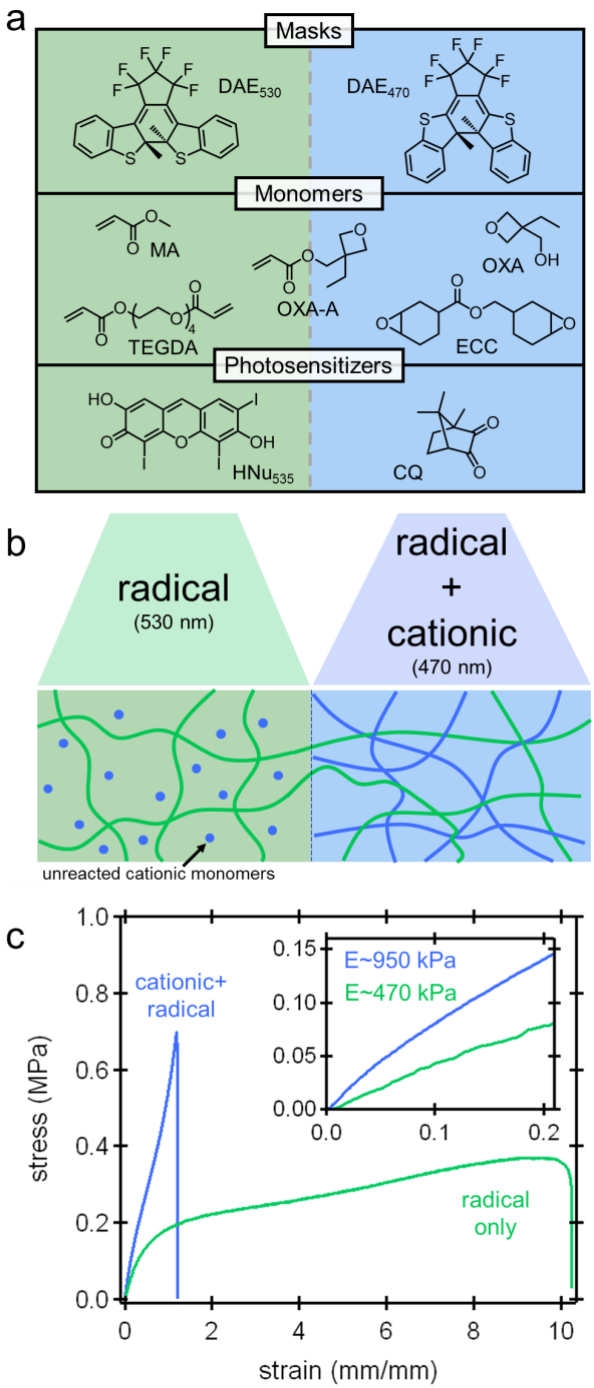

Fig. 1. a) Chemical structures of the major resin components used in this work. b) Schematic network structures resulting from irradiation of the resin with green (530 nm) or blue (470 nm) light. c) Representative (nominal) stress-strain plots of resulting materials after removal of unreacted species.

4.2.1 Design & Mechanical Testing of Bio-Inspired Multimaterial 3D Prints

Examples of hierarchical multiphase materials are ubiquitous in biology. Notable examples include stiff and fracture-resistant trabecular bone[100], [101], the resilient soft solids that comprise multicellular tissues[102]–[104], complex biofilms comprising microbes in a soft matrix[105], and the extracellular adhesives produced by marine mussels[106]. In particular, the natural materials produced by mussels have garnered significant interest for their relative strength and remarkable ability to adhere to a variety of surfaces in wet, turbulent intertidal zones. The structure-property relationships of the mussel's holdfasts have been examined [107]–[109], and their unique toughness[110], [111], adhesion ability [112]–[115], and biochemistry [114], [116] have been thoroughly characterized and mussel-inspired materials with notable mechanical performance[117], [118] have been developed. However, prior designs of mussel-mimetic materials rarely consider the material composition and structure of the natural material (Fig. 2a), despite its hypothesized role in the toughness of the mussel's load-bearing holdfasts.[110], [119], [120] Inspired by such design motifs, polymer-polymer composites comprising a stiff 'shell' and a soft porous 'core' with defined pore sizes and packing orientations (Fig. 2b) were designed, printed using SMaLL, and tensile tested. The stiff and soft domains exhibit distinct mechanical responses—i.e., a two-fold difference in elastic moduli, a nearly ten-fold difference in extensions to failure, and distinct yield behaviors—yet are covalently linked through a shared radically-cured acrylate network.[98] Based on these design features, samples with an outer shell defined by blue light and an interior core with porosity defined by green light were prepared. In addition, the pore

size and pore packing order were varied to uncover structure-property relationships that in turn inform fracture-resistant composite design. To this end, samples with mean pore diameters of 1600, 1300, and 1000 μm were patterned into either hexagonal- or square-packed lattices (Fig. S2). To simplify the comparison between samples, the area fraction of pores was held constant (51 ± 3%).

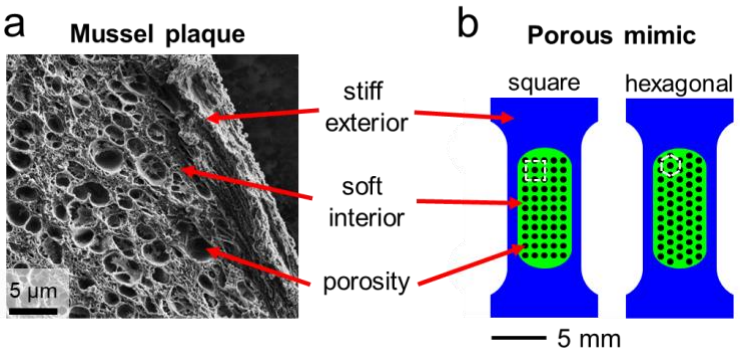

Fig. 2. a) Micrograph of a sectioned mussel plaque, with distinct design elements, such hierarchical and multiphase features are ubiquitous in biological materials. **b)** Mimetic templates with blue, green and black regions to define a stiff outer shell, soft interior core, and controlled pores using SMaLL. White shape to emphasize packing of pores.

To establish a benchmark mechanical response, samples devoid of pores were first examined. For all specimens, at some critical load, cracks in these samples consistently initiated at the exterior of the sample and rapidly propagated linearly across the sample, perpendicular to the axis of load, until they exited through the opposite side (Fig. S8 and Supplementary Video S8). The lack of porosity in the soft interior of the sample eliminates any possibility for crack blunting or stress dissipation—allowing the crack to propagate through the sample uninhibited.

Conversely, samples containing patterned pores exhibit a large degree of crack deflection. Further tensile tests revealed that porous samples experience highly non-linear or tortuous crack propagation (Fig. 3a) based on pore size and orientation (Fig. S3). An extreme case of this behavior is seen in a hexagonally-packed, 1000-μm pore sample whose fatal crack pivots ninety degrees twice before exiting the sample (Fig. 3b and Supplementary Video S9). In this example, a crack forms at 250% strain near the bottom of one end of the sample, followed shortly thereafter by a nearly-identical, diagonally-opposed crack in the exterior shell at the opposing end. Instead of leading to the immediate failure of the sample, however, the pores momentarily halt crack propogation and the sample rotates and shear in the soft porous core of the fracturing specimen forces the diagonally-opposed cracks to pivot ninety degrees until they meet in the middle of the soft core, causing failure nearly 100% strain after the point of initiation (Fig. 3c). Despite the encouraging changes in failure behavior and remarkable reorganization enabled by deformation and scission of the thin struts forming the pore walls of the inner core, tests investigating the relationship between crack tortuosity and pore size/packing were inconclusive due to the stochasticity of crack initiation (Fig. S3-S4).

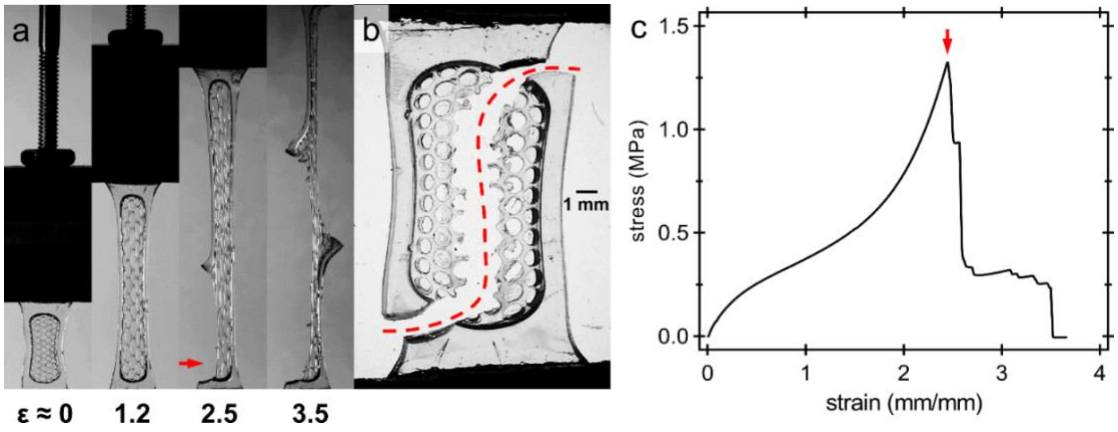

Fig. 3. Results from the uniaxial loading of a pristine sample with hexagonally packed 1000 µm voids. **a)** Still-frames of the sample under increasing strain. **b)** Optical microscope image of the fractured part, demonstrating a high degree of crack tortuosity. **c)** The (nominal) stress-strain plot corresponding to parts a/b, showing distinct failure events after the onset of crack propagation (arrow) that correspond to the breaking of individual ligaments within the material.

To more accurately assess the impact of porosity and multimaterial composition, notches were designed and printed into in the outer shell of each sample near a centrally-located pore, thus creating a controlled point of crack initiation. Using notched samples, systems with square-packed pores were found to undergo less tortuous crack paths when compared to their hexagonally-packed counterparts (Fig. 4a,b, and Figs. S6-7). Furthermore, the increased tortuosity in the hexagonally-packed samples often led to enhancements in strains to failure (Fig. 4c and Supplementary Video S10). In each case, we quantify the degree of tortuosity of the crack paths by dividing the length of the crack by the width of the sample at its notch point (i.e., c_{norm}). For example, a crack that propagates from its notch point straight across the sample will have a normalized crack length value of $c_{norm} = 1$, while a crack that deviates from this linear path will have a $c_{norm} > 1$. Using this metric, it was

found that, irrespective of pore size, all samples with square-packed pores endured near-linear crack paths (Fig. 5), similar to the results obtained in the pore-free samples. Conversely, cracks in the hexagonally-packed samples showed a clear increase in tortuosity with decreasing pore size.

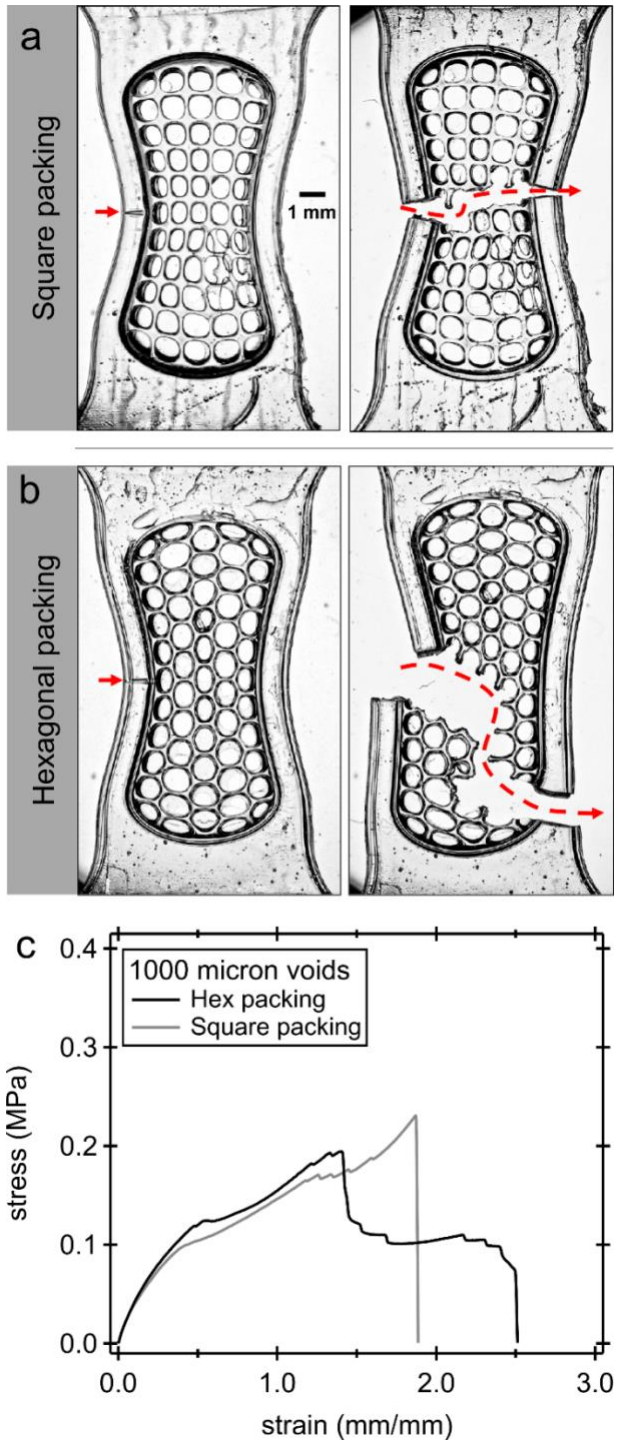

Fig. 4. Summary of results from notched samples, giving access to controlled crack initiation. Optical microscopy images of a) a notched square packed sample and **b)** a notched hexagonally packed sample with 1000-µm pores before and after being strained to failure. Initial

notches and crack paths denoted by arrows and dashed lines, respectively. **c)** Representative (nominal) stress-strain plot of the two samples, additional results are shown in Fig. S9.

4.2.2 Finite Element Analysis

To probe the underlying mechanisms connecting packing geometry and crack tortuosity we turned to 2-D finite element (FE) modelling of square- and hexagonally-packed porous samples to which tension was applied from 0 to 100% strain in increments of 20% (full details available in the Supporting Information). The principal stresses on the surfaces of the hexagonally- and square-packed samples (pore size = 1600 μm) strained to 100% are illustrated in Fig. 6. The distribution of principal stresses remains roughly unchanged even for smaller pore sizes (Figs. S12-S15). For both geometries, we hypothesize that the regions of highest stress in the porous core guide the crack path, as these are more likely to fracture than low-stress regions, and thus influence the degree of crack tortuosity.

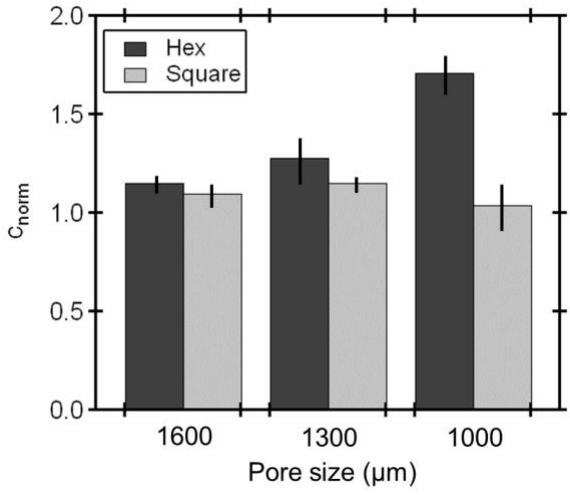

Fig. 5. Impact of pore size and packing of voids on crack tortuosity. Error bars are the result of triplicate runs.

As expected we see packing-dependent differences in maximal stress distribution around each pore. For the square-packed sample strained to 100%, the highest stresses within the core are located at the mid-section of the ligaments perpendicular to the loading axis (Fig. 6a). As such, once a crack traverses the stiff shell and enters the soft core, the thin ligaments between pores bear increasing load and are likely to fail consecutively—leading to linear crack paths perpendicular to the strain axis with little tortuosity. Conversely, the hexagonally-packed specimens display the highest stresses in ligaments oriented at an angle $\theta \approx \pm 60°$ to the axis of strain (Fig. 6b), where the maximum stress between pores was found to be significantly reduced relative to the square-packed example (0.97 and 1.54 MPa respectively). Thus, once a crack traverses the shell into the soft core, it has equal likelihood of fracturing one of two ligaments at either ±60° as they bear increasing load. We believe that this initial “fork” in the crack path leads to the deviation from linear crack paths in hexagonally-packed samples and increased tortuosity, as observed. As the crack propagates and encounters additional pores, the stress distribution likely becomes more asymmetric and random, thereby increasing the crack tortuosity as a function of an increasing number of pores encountered across the sample. In an effort to identify possible mechanisms controlling the crack tortuosity in these designs, a simple model was developed (see Supporting Information Section 4C), that demonstrates the important role stochastics likely play

in the high degrees of tortuosity observed for hexagonal samples. A full treatment of the crack propagation problem would require analysis of the non-linear mechanical responses, as well as in-plane rotation of the sample during extension, which is beyond the scope of this initial investigation; in the future, such analysis could enable predictive programming of the failure dynamics using structured material design.

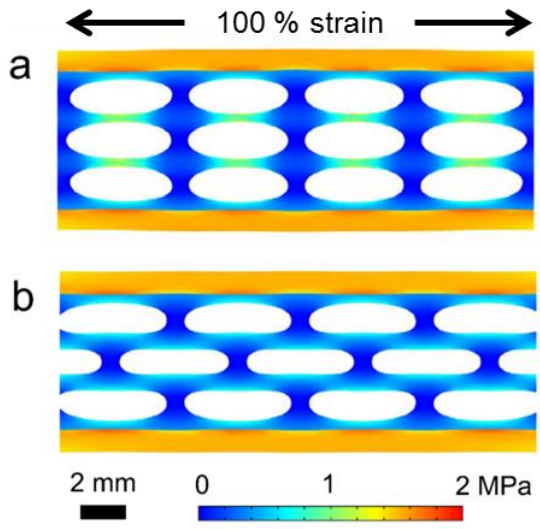

Fig. 6. Summary of results from finite element methods analysis at 100% strain. Color maps of principal stresses on the surface of the **a)** square-packed and **b)** hex-packed samples. These results are illustrative of the 1600-μm pore diameter samples. The full results for the 1600-μm and 1000-μm pore diameter samples can be seen in Figs. S12-S15.

4.3 Conclusions

In summary, we employed a novel strategy for multimaterial additive manufacturing to produce polymer-polymer composites with design motifs inspired

by nature. By exploiting wavelength-selective polymerization and curing chemistries we printed polymer-polymer composites comprised of a spatially resolved stiff exterior shell and a soft core with well-defined pore sizes/packing. In tension, samples with hexagonally-packed pores of decreasing size demonstrated increased crack tortuosity when compared to samples with square-packed pores, highlighting the importance of pore packing on material performance. The manufacturing strategies and mechanical insights advanced through this work are valuable for the design and development of future resilient multimaterial, polymer-polymer composites. Ongoing research includes the incorporation of micron-sized porogens and hydrogel microparticles into SMaLL resins to further understand property enhancement from three-dimensionally defined, multimaterial systems.

4.4 Materials & Methods

Details of resin preparation, sample production, and sample design are described in Appendix III, Sections 1-2. Experimental protocol and data analysis methods are included in Appendix III, Section 3. Details of FE simulations are presented in Appendix III, Section 4.

V. Future Directions & Concluding Remarks

Let’s take a moment to talk about bubbles. The concept of a “bubble” can happen anywhere, but let’s start with financial bubbles due to their current relevance to the U.S. economy. A financial bubble is characterized by a fast, large climb in the

price of an asset (e.g., stock in a company), usually driven by buyer speculation or the optimistic belief that the price will continue to rise. However, this rapid growth is relatively short-lived and (often without warning) abruptly reverses course, dragging the price of the asset down with it—much like a bubble popping. One popular example is the burst of dot-com bubble in the early 2000s.

Academia—a marketplace of ideas—is equally prone to bubbles. In fact, Hawkes and co-workers identified characteristics of a bubble in the blossoming field of soft robotics—pointing out that "growth [of a new academic field] can be followed by an equally rapid decline if concerted efforts are not made by the community." [121] In their paper, Hawkes and co-workers argued that in order for the field of soft robotics to grow sustainably over the next decade, every research study must offer a meaningful contribution (i.e., demonstrating unique utility or intrinsic advantage by leveraging softness) to the field of soft robotics and, more broadly, adjacent engineering fields. Looking forward, I foresee soft robotics offering meaningful contributions in five key areas: external therapeutics (i.e., wearables, prosthetics, etc.), internal therapeutics, navigation of unmapped environments for exploration (i.e., extraterrestrial, terrestrial, sub-terrain, and aquatic) and in emergency situations (e.g., building on fire), bio-inspired force transduction and energy storage (e.g., jumping robots that emulate biological organisms), and finally softness for safety (e.g., human-robot interaction, delicate handling of objects, flora, and fauna). Concerted effort focused on creating application-specific innovations in these areas are sure to advance our understanding of the natural world and our ability to navigate it—as individuals (e.g., via prosthetics) or remotely (e.g., via autonomous

soft robots). The studies presented in this thesis are merely steppingstones that advance the field towards achieving some of these feats. Below, I offer thoughts on how each of the studies presented herein might be extended for higher impact.

In Chapter II, we identified the primary sources of loss in soft heat engines and offered practical methods for improving their efficiency. Improving the efficiency of soft robots increases their functionality—e.g., performing high-power-output maneuvers given a fixed input power, traveling longer distances using finite on-board energy sources, and much more. Yet the question lingers: in what scenario might a soft, efficient robot offer greater utility than its rigid counterpart? There isn't a catch-all answer, but below I discuss two exemplary answers on two different length scales.

On the macro-scale (>cm), the combination of softness and efficiency bode well for soft wearables and therapeutics interfacing with the human body. An increasing number of investigations detail the development of soft, smart, skin-mounted sensors [122], [123] and phase-change-enabled wearable assistive technologies [4], [124]. Our investigation in Chapter II offers new analysis of phase-change-powered soft robots and sensors that enable efficient untethered operation. On the meso-scale (mm-cm), it was recently demonstrated that soft-bodied robots could burrow through granular media (e.g., sand) an order of magnitude faster than any rigid counterpart to date [125]. While this robot remained tethered to a base station, future iterations might be completely untethered from any surface-based stations for autonomous subterrain exploration. Here, efficient use of on-board energy as well as

geothermal energy harvesting may enable further subterranean exploration inaccessible to rigid robots.

In Chapter III, we explore the solvent-dependent photokinetic properties of a photoswitch. We found that the negative photochromism and high absorbance in donor-acceptor Stenhouse adducts (DASAs) combined with our growing understanding of their kinetics yield interesting self-regulating behavior. This self-regulating change in absorbance might constitute the basis of a thermal switch that sets the hot and cold operating temperatures of a soft heat engine. However, two obstacles need to be hurdled to realize this mechanism. The first hurdle is DASAs' ability to produce enough heat to incite phase change. DASA 3.0, while high-absorbing, demonstrate concentration-dependent kinetics that limit good switching performance to low concentrations (<1 mM) which in turn limit light-to-heat conversion. A work-around might comprise a solution containing two solutes: a photothermal heating agent (e.g., Carbon Black) whose function is to convert light to heat and warm the solution to just below its saturation (i.e., boiling) temperature, and DASA 3.0 whose function is to supply the rest of the heat in its absorbing/non-switched state and reject heat in its non-absorbing/switched state. The second obstacle in realizing a thermal switch for soft heat engines is enforcing stepwise switching of DASA 3.0 in solution. At present, incident light of sufficient intensity and flux instantaneously triggers the switching reaction of DASA 3.0 at low concentrations. This instantaneous switching prevents significant heat generation. Ongoing research investigates the use of chemical additives to hold DASA 3.0 in its non-switched/absorbing state until sufficient heat is generated. The combination of

these two innovations might enable thermal-switching behavior that enables self-regulating heat engines for soft robots.

In Chapter IV, we leveraged a recently developed light-controlled single-step multimaterial printing process (SMaLL) to create polymer-polymer composites that capture the key features of porous and multiphasic natural materials. In testing these materials, we found that templated porosity inside of a stiff-soft structure enhances fracture strain. While our study focused on enhanced material properties, enhanced robot performance has been realized by designing a combination of stiffness and softness into a soft robot body. For example, Boddeti and co-workers have demonstrated that topological optimization of a stiff-soft batoid-inspired robot body yields 50% faster swimming speeds [126]. 3D-printing technologies such as SMaLL, capable of printing materials of vastly different moduli side-by-side and with strong interfaces, are critical to further investigations of enhanced performance derived from stiff-soft robot bodies. Furthermore, SMaLL's resin-based printing process may be amenable to suspending critical fabrication components (e.g., sensors, tubing, etc.) in resin for rapid, one-step fabrication of "smart" soft robots.

In summary, these investigations offer small but innovative steps in advancing the field of soft robotics. However, continued development of new power sources, energy-harvesting schemes, materials, and fabrication schemes are necessary to stave off a bubble-like collapse of the field of soft robotics, and instead cement its value to adjacent fields of engineering as well as society. It is here, with great joy, that I pass the torch on to the next wave of soft robotics researchers and conclude the final chapter of this thesis.

Appendix I: Supplementary Information, Chapter II

Text S1. Key differences between soft heat engines & industrial heat engines.

Due to size and material constraints, the thermodynamic behavior of soft heat engines differs from that of large industrial systems. These differences warrant new thermodynamic analysis. First, size must be considered as all objects exhibit decreasing surface area relative to volume as they increase in size. Simultaneously, heat losses—i.e., convective, conductive, and radiative—scale linearly with surface area and thus larger systems tend to incur relatively fewer heat losses. Second, the construction materials of soft heat engines must be carefully considered. While steam-driven plants benefit from continued materials research (e.g., insulating materials, superalloys) that allow them to operate between 500-700 °C, soft heat engines are typically composed of thin-walled (i.e., ~0.5-5 mm) polymers & elastomers that undergo undesirable property changes (e.g., melting, glass transition, degradation) at much lower temperatures (> 100 °C), necessitating relatively low-temperature operation. Furthermore, the thin walls and low failure stresses of these same polymers and elastomers necessitates the use of pressures (<50 kPa) that are orders of magnitude lower than large industrial applications such as a water boiler. Third, the use of cyclic pressure-volume processes that deform the walls of the soft heat engine pose a unique challenge. Condensers in industrial power plants often leverage rigid pipes and containers to condense their fluid at pressures well below ambient, resulting in low condensation temperatures that

improve efficiency. By contrast, the deformable walls of soft heat engines are always being compressed by atmospheric pressure. Thus, condensing at pressures below atmosphere in a soft constraint result in further compression by atmosphere, which must later be overcome before vaporization can occur. As such, atmosphere acts as an unwanted restoring force on the system which incites additional losses. The combination of these unique constraints necessitates thermodynamic analysis of soft heat engines in an effort to improve their efficiency.

Text S2. Methods for addressing temperature limit losses.

As stated in the main text, temperature limit losses are inefficiencies due only to temperature and can be identified by examining the Carnot efficiency:

$$\eta_C = 1 - \frac{T_c}{T_h} \tag{9}$$

Here, T_c and T_h are the cold and hot reservoir temperatures, respectively. Losses are minimized when T_c/T_h approaches 0; however, several material constraints (e.g., thermal degradation of soft materials) make it challenging to achieve this. Heat engine operation at temperature extremes poses serious engineering challenges in rigid systems, and even more so in soft systems. For example, to achieve high temperature operation in a soft heat engine, the ideal wall material should have low heat loss (e.g., low thermal conductivity), stable mechanical properties at high

temperatures, and resist rupture at high pressures. Simultaneously, to minimize other losses, such a material should have minimal resistance to deformation during volume change, minimal hysteresis, near-zero gas/vapor permeability, and good chemical compatibility with the working fluid. To our knowledge, commercially available materials that meet these criteria presently do not exist. As such, commercially available soft heat engine construction materials pose constraints on accessible operating temperatures.

First, the theoretical upper bound of T_h is limited by the maximal temperature that the soft heat engine's heater can achieve. We term this loss "T_h Limit 1." In practice, however, STAPAs seldom reach these temperature bounds due to deleterious heat losses or material constraints (e.g., system melting temperature). We term the actual temperature that the system can reach "T_h Limit 2."

The final temperature limit loss is incurred due to an elevated cold reservoir temperature, T_c. As it is impractical to modify the surroundings, T_c is usually equivalent to the ambient temperature, T_∞. However, for liquid-to-vapor phase change to occur and the STAPA to do work against atmospheric pressure, the effective fluid temperature must at minimum equal its saturation temperature (i.e., boiling point) at ambient pressure. Below the boiling point, atmospheric pressure compresses the walls of the STAPA and condenses any vapor back to liquid. As such, a fluid with a boiling point that exceeds ambient temperature raises the cold reservoir temperature from ambient (e.g., $T_c = T_\infty = 20$ °C) to the boiling point of the

fluid (e.g., for water, $T_c = T_{boil} = 100$ ℃), thus decreasing the Carnot efficiency. Lowering T_c can be achieved via a few methods: (1) synthesizing a working fluid that boils close to ambient, (2) operating in a low-atmosphere environment (e.g., space), and/or (3) operating at a sub-ambient temperature (e.g., via radiative cooling). However, these solutions either pose significant engineering challenges or impractical environmental constraints.

Text S3. Derivation of the efficiency of the rectangular cycle with no losses.

Assumptions and Setup

Given the popularity of liquid-gas phase change, we focus our analysis on single component liquid-gas phase change systems. For simplicity, we assume that all processes occur within the vapor dome; this is a reasonable assumption since soft heat engines usually have an excess of liquid working fluid. Furthermore, we assume reversible quasistatic processes, closed systems, well mixed mixtures, and uniform temperatures within the heat engine (i.e., lumped capacitance model). For our working fluid, we use Novec 7000.

To keep our analysis within the vapor dome, we set $v_{min} \geq v_f(T)$ and $v_{max} \leq v_g(T_2)$. v_f and v_g are the saturated liquid and vapor specific volume, respectively. Typically,

we set $v_{min} = v_f(T_2)$. We set $T_1 = 308\ \mathrm{K}$, a temperature slightly higher than the boiling point of Novec 7000.

Note that although our analysis focuses on liquid-gas systems, our results can be applied to any single component phase change system where internal energy increases with volume and temperature. The change of internal energy can be written as

$$du = c_v\, dT + \left(T\left(\frac{dP}{dT}\right)_v - P\right) dv$$

u, c_v,T,P, and v are the specific internal energy, specific constant volume heat heat capacity, temperature, pressure, and specific volume respectively. Internal energy is guaranteed to increase with volume and temperature if

$$\left(T\left(\frac{dP}{dT}\right)_v - P\right) > 0$$

which is generally true for liquid-gas phase change. If this is true for the region of analysis, then constant pressure and increasing pressure processes will have a net positive change in internal energy. An example of a system, where this is not true is the liquid water to ice transition.

Derivation of Efficiency

The solid lined rectangle in **Error! Reference source not found.**A shows the rectangular cycle.

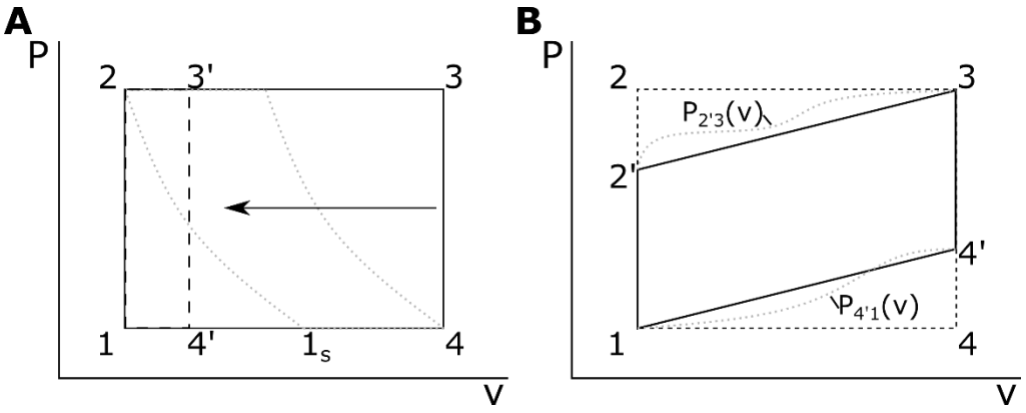

Fig. S1. Sketch of different cycle shapes. (A) The rectangular cycle is in the solid lined rectangle. The grey dotted curves are the isentropic curves of a Carnot cycle that fully span the pressure and specific volume range of rectangular cycle. The dashed, black-lined rectangle (points 1, 2, 3', 4') is a rectangle in which a Carnot cycle cannot fit. **(B)** The black solid-lined parallelogram shows an upward sloping parallelogram cycle. The dashed black rectangle is a rectangular cycle with the same volume and pressure limits as the upward parallelogram cycle. The dotted grey curves represent arbitrary simple upward sloping processes.

To derive the ideal efficiency, we begin with the thermodynamic first law:

$$\delta q = du + \delta w$$

δ represents a path dependent differential and d represents a state dependent differential. q and w represent specific heat input and specific work output respectively.

The process from 1 to 2 is isochoric and requires no work, so the heat input, q_{12}, required is

$$q_{12} = u_2 - u_1$$

The process from 2 to 3 isobaric, so the heat input, q_{23}, required is

$$q_{23} = u_3 - u_2 + P_2(v_3 - v_2) = \hbar_3 - \hbar_2$$

Where $\hbar$ is specific enthalpy. The work done by that process, w_{23}, is

$w_{23} = P_2(v_3 - v_2)$

From 3 to 4, the system undergoes isochoric cooling. This requires no heat input.

From 4 to 1, the system undergoes isobaric compression. No heat input is required, but the environment does work on the system; thus, the net produced specific work, w, is

$$w = (P_2 - P_1)(v_3 - v_2)$$

The total heat input, q_{in}, is

$$q_{in} = q_{12} + q_{23} = u_3 - u_1 + P_2(v_3 - v_2) = \hbar_3 - \hbar_2 + u_2 - u_1$$

Therefore, the ideal rectangular cycle efficiency, η_R, is

$$\eta_{R,ideal} = \frac{w}{q_{in}} = \frac{(P_2 - P_1)(v_3 - v_2)}{u_3 - u_1 + P_2(v_3 - v_2)} = \frac{(P_2 - P_1)(v_3 - v_2)}{\hbar_3 - \hbar_2 + u_2 - u_1}$$

The right-hand side shows that the efficiency of the rectangular cycle is limited by the isochoric heating. Efficiency is maximized when $u_2 - u_1 \ll \hbar_3 - \hbar_2$.

Error! Reference source not found.A plots the ideal efficiency as a function of m aximum specific volume and as a function of maximum temperature. As expected, efficiency improves with increased vaporization (i.e., increasing $\hbar_3 - \hbar_2$) and as temperature increases.

Error! Reference source not found.B compares the rectangular cycle efficiency to t hat of a Carnot cycle operating within the same temperature bounds. Somewhat surprisingly, for a wide range of maximum volumes and temperatures, the efficiency is close to that of the Carnot cycle. In general, Carnot efficiencies are approached if $u_2 - u_1 \ll \hbar_3 - \hbar_2$. Note that while η_R/η_C values illustrate how close a cycle is to the thermodynamic ideal, high values do not necessarily guarantee high efficiencies.

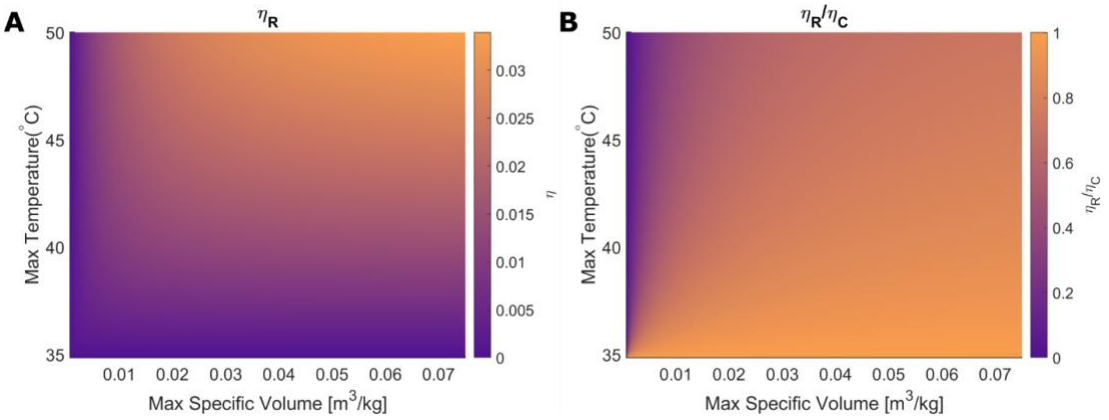

Fig. S2. (A) Ideal rectangular efficiency as the maximum specific volume and temperature are varied. **(B)** Efficiency comparison between the rectangular cycle and the Carnot cycle operating between the same temperature bounds as the maximum specific volume and temperature of the rectangular cycle is varied. For the analysis, $T_1 = 308\,K$ and $v_1 = 7.5 \times 10^{-4} m^3/kg$.

While **Error! Reference source not found.** shows a wide range of maximum s pecific volumes, it can be more illustrative to show results for a smaller range of maximum specific volumes (**Error! Reference source not found.**). Expanding to l arger specific volumes can pose some engineering challenges. For example, if a

system has too little liquid, then the vapors might condense in areas away from the heater, making it harder to cycle the system.

Error! Reference source not found.A shows the rectangular cycle efficiency for a s maller range of maximum specific volumes. In general, the efficiency limits are lower. The decrease in efficiency limits is most severe for systems operating at higher temperatures (i.e., $u_2 - u_1 \sim \hbar_3 - \hbar_2$). **Error! Reference source not found.**B c ompares rectangular cycle efficiency to that of the Carnot cycle for smaller maximum specific volume limits. High η_R/η_C values are possible, but in general most systems in this regime have low η_R/η_C values.

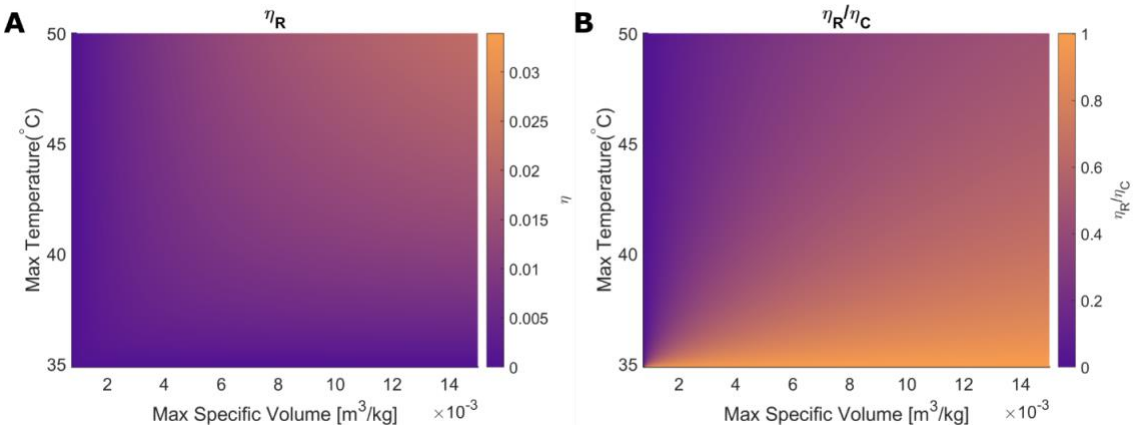

Fig. S3. (A) Rectangular cycle efficiencies for lower maximum specific volumes. **(B)** Efficiency comparison between the rectangular and Carnot cycles for lower maximum specific volume values.

One interesting thing to analyze is whether a Carnot cycle with the same working substance can fully span the pressure and specific volume range of a rectangular cycle. **Error! Reference source not found.**A sketches the problem. A Carnot cycle can span the same bounds if the following constraint is met:

$$s(T_2, v_2) < s(T_4, v_4)$$

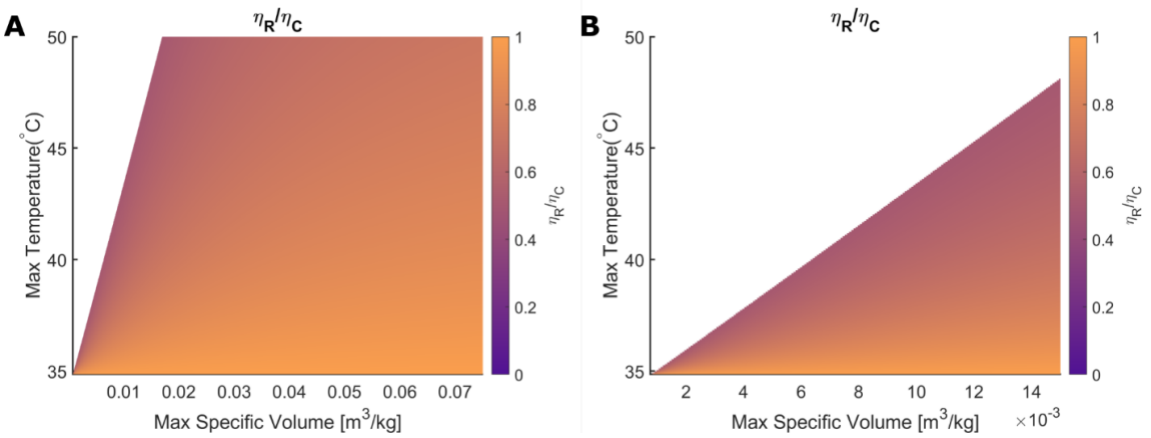

Fig. S4. Efficiency comparison between the rectangle and Carnot cycles. The blank regions show regions where Carnot cycles fail to span the same temperature and specific volume range as a rectangular cycle with the same working fluid. (**A)** shows a larger range of specific volumes and (**B)** shows a smaller range.

The blank regions in **Error! Reference source not found.** shows where a Carnot c ycle with the same working fluid fails to satisfy the inequality. These regions lie in areas with low η_R/η_C values, and cycles with the same working fluid that span those bounds will be inherently inefficient. Additionally, unlike the shaded regions, the

optimal cycles in the blank regions that satisfy the temperature and specific volume constraints are not necessarily Carnot cycles.

Text S4. Derivation of the efficiency of the rectangular cycle with heat losses.

Based on the low measured efficiencies and the long time scales in preliminary experiments, we hypothesize that heat loss is the dominant source of losses in soft heat engines. To analyze its effects, we incorporate a simplified convective heat loss model into our theory.

Differentiating the first law with time, we obtain

$$\frac{du}{dt} = \frac{dq}{dt} - \frac{dw}{dt}$$

Incorporating a simple heat loss model, results in the following expression for heat input rate:

$$\frac{dq}{dt} = \dot{q_{in}} - h(T - T_{\infty})$$

$\dot{q}_{in}$ is the rate of heat input into the heating element, h is the heat loss coefficient, and T_{∞} is the environmental temperature. For simplicity, we assume h is configurationally independent.

No net heat input is possible when the temperature of the system exceeds the equilibrium temperature. The upper limit for the temperature is

$$T_{2,max} = T_\infty + \frac{\dot{q_{in}}}{h}$$

The time it takes from point 1 to point 2 can be determined by solving the differential equation:

$$\frac{du}{dt} = \dot{q}_{in} - h(T - T_\infty)$$

Temperature is determined from the internal energy state function, $u(T, v)$.

For our application, the change in internal energy can be modeled by

$$\frac{du}{dt} \cong c_v \frac{dT}{dt} = \dot{q_{in}} - h(T - T_\infty)$$

Given the small temperature range, c_v can be assumed to be constant.

The solution to the differential equation is:

$$T = \frac{e^{-\frac{ht}{c_v}}\left(\left(e^{\frac{ht}{c_v}} - 1\right)\dot{q_{in}} + h\left(T_1 + T_\infty\left(e^{\frac{ht}{c_v}} - 1\right)\right)\right)}{h}$$

The time it takes to reach state 2 is:

$$t_{12} \cong \frac{c_v \ln \frac{\dot{q_{in}} - h(T_1 - T_\infty)}{\dot{q_{in}} - h(T_2 - T_\infty)}}{h}$$

Thus, the heat input from state 1 to 2 is:

$$q_{12} \cong \dot{q_{in}} \frac{c_v \ln \frac{\dot{q_{in}} - h(T_1 - T_\infty)}{\dot{q_{in}} - h(T_2 - T_\infty)}}{h}$$

The energy balance for a quasi-static expansion from point 2 to point 3 is

$$\frac{d\hbar}{dt} = \dot{q_{in}} - h(T_2 - T_\infty)$$

Therefore, the time it takes to expand from state 2 to 3 is

$$t_{23} = \frac{\hbar_3 - \hbar_2}{\dot{q_{in}} - h(T_2 - T_\infty)}$$

Thus, the total heat input from 2 to 3 is

$$q_{23} = \frac{\hbar_3 - \hbar_2}{\dot{q_{in}} - h(T_2 - T_\infty)} \dot{q_{in}}$$

Thus, the estimated heat input is:

$$q_{in} = q_{12} + q_{23} \cong \frac{\hbar_3 - \hbar_2}{\dot{q_{in}} - h(T_2 - T_\infty)} \dot{q_{in}} + \dot{q_{in}} \frac{c_v \ln \frac{\dot{q_{in}} - h(T_1 - T_\infty)}{\dot{q_{in}} - h(T_2 - T_\infty)}}{h}$$

Thus, the approximate efficiency of the rectangle cycle with heat transfer is:

$$\eta_{R,ht} \cong \frac{(P_2 - P_1)(v_3 - v_2)}{\dot{q_{in}} \left(\frac{\hbar_3 - \hbar_2}{\dot{q_{in}} - h(T_2 - T_\infty)} + \frac{c_v(T_2 - T_1)}{\dot{q_{in}} - h(T_1 - T_\infty)} \right)}$$

In comparison, the idealized efficiency is:

$$\eta_R = \frac{(P_2 - P_1)(v_3 - v_2)}{\hbar_3 - \hbar_2 + u_2 - u_1} \cong \frac{(P_2 - P_1)(v_3 - v_2)}{\hbar_3 - \hbar_2 + c_v(T_2 - T_1)}$$

Thus,

$$\eta_{R,ht} \cong \frac{\hbar_3 - \hbar_2 + c_v(T_2 - T_1)}{\frac{\hbar_3 - \hbar_2}{\dot{q_{in}} - h(T_2 - T_\infty)} + \frac{c_v(T_2 - T_1)}{\dot{q_{in}} - h(T_1 - T_\infty)}} \eta_R$$

Expanding the prefactor about $T_2 = T_1$ yields the simplified efficiency:

$$\eta_{R,hts} = \frac{\dot{q_{in}} - h(T_2 - T_\infty)}{\dot{q_{in}}} \eta_R = \eta_{ht} \eta_R$$

To first order, we see that with heat transfer, the efficiency of the rectangle is composed of two terms a heat transfer efficiency term, η_{ht}, and the ideal term. The heat transfer efficiency term always decreases with temperature, but the ideal efficiency term generally increases with temperature. Thus, there is some optimal temperature. One interesting thing to note is that the heat transfer efficiency term is volume independent, which means it still benefits to expand as much as possible.

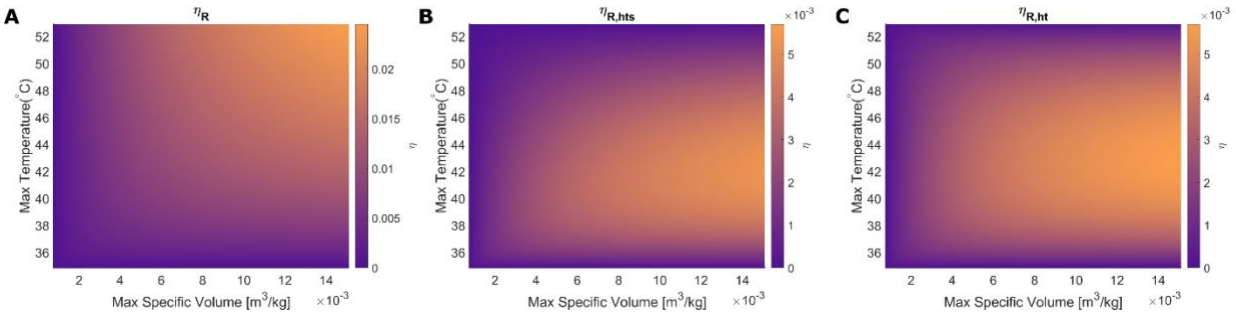

Fig. S5. Comparisons of the different rectangle cycle efficiencies. (**A)** without heat transfer. (**B)** simplified model. (**C)** exact model. For the model, $\dot{q}_{in} = 150\ W/kg$, $T_\infty = 296.15\ K$, and $h = 5\ W/kg/K$

Error! Reference source not found.A, B, and C plots the rectangle cycle efficiency w ithout heat transfer, with the simplified heat transfer equation, and the exact form, respectively. For the model, $\dot{q}_{in} = 150\ \mathrm{W/kg}$, $\mathrm{T}_\infty = 296.15\ \mathrm{K}$, and $h = 5\ \mathrm{W/kg/K}$. The presence of heat transfer significantly reduces the efficiency of the rectangular cycle. There is good agreement between the simplified efficiency form and the exact form, but the simplified form slightly underpredicts the efficiency. **Error! Reference s**

ource not found. plots the effect of varying heat input. Increasing heat input increases efficiency.

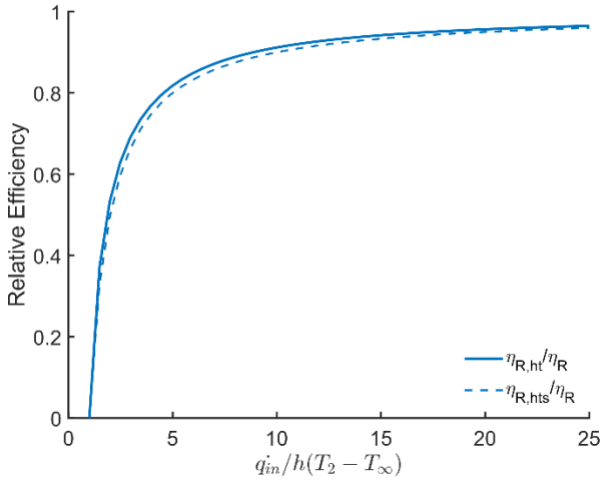

Fig. S6. Effect of varying heat input. $T_2 = 320\ K$, $T_\infty = 296.15\ K$, $v_1 = 7.63 \times 10^{-4}\ m^3/kg$, $v_3 = 1.53 \times 10^{-2} m^3/kg$, and $h = 5\ W/kg\ /$.

Text S5. Fabric heater fabrication and testing.

The heater used in all benchtop experiments described in the main text is comprised of conductive fabric (EonTex, NW170-PI-20) laser cut (Trotec, Speedy 100) into a disk with a couple of additional features. Four holes, 0.5 mm in diameter, were cut around the perimeter of the disk to allow fine gauge wire to be thread through. Drawing upon insights from an earlier investigation[127], an array of slits was cut through the center of the fabric to improve the even flow of current through the heater.

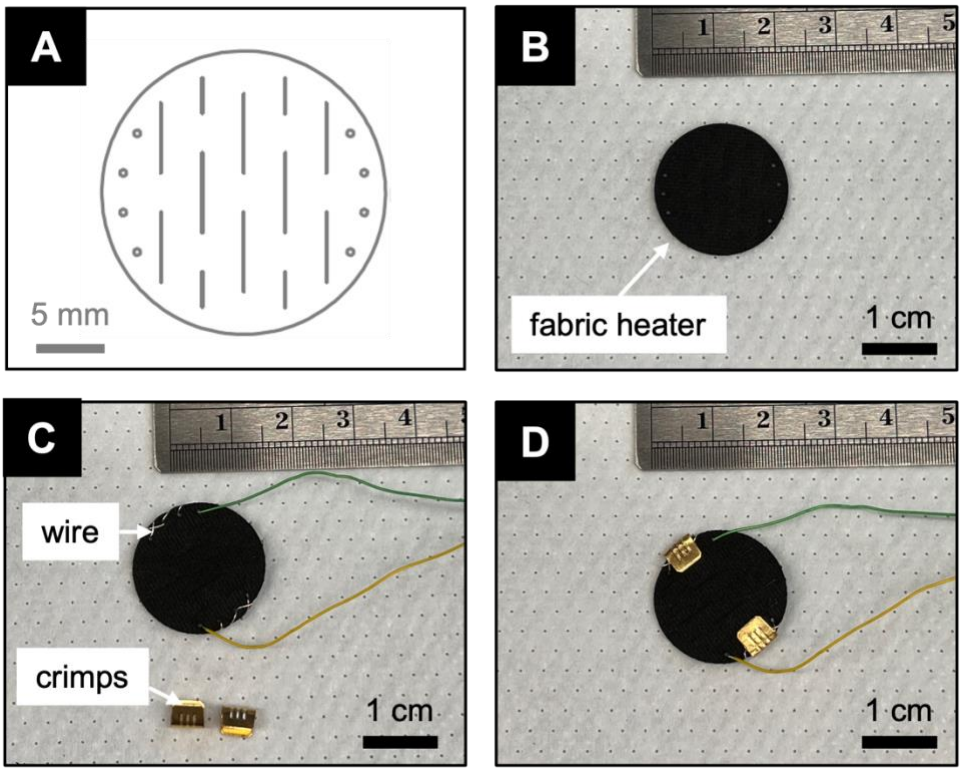

Fig. S7. Heater design and fabrication. (A) A computer-aided design drawing used to laser cut the fabric disks for the heater. **(B)** The fabric heater before assembly. **(C)** Fine wire (30 gauge) was then thread through 0.5 mm holes around the disk perimeter to allow current to flow from the benchtop voltage source to the fabric heater. **(D)** Crimps were then clamped onto the wire stitching, to ensure good electrical contact between the wire and the fabric.

Text S6. Actuator fabrication for benchtop testing.

Pouches used both in the roller and in the benchtop experiments were composed of commercially available multi-ply polymer sheets (consisting primarily of Mylar) for vacuum sealed food storage (Wevac Vacuum Sealer Bags, Amazon.com). As

purchased, each roll consists of two sheets of material—one scalloped and one non-scalloped—heat sealed to each other. We discard the scalloped sheet and use only the non-scalloped sheet due to its high transmissivity across a broad range of wavelengths (Fig. S8), robustness to puncture, relatively low gas permeability, and amenability to heat sealing. The steps for fabricating the actuator for benchtop testing can be found in the caption of Fig. S9.

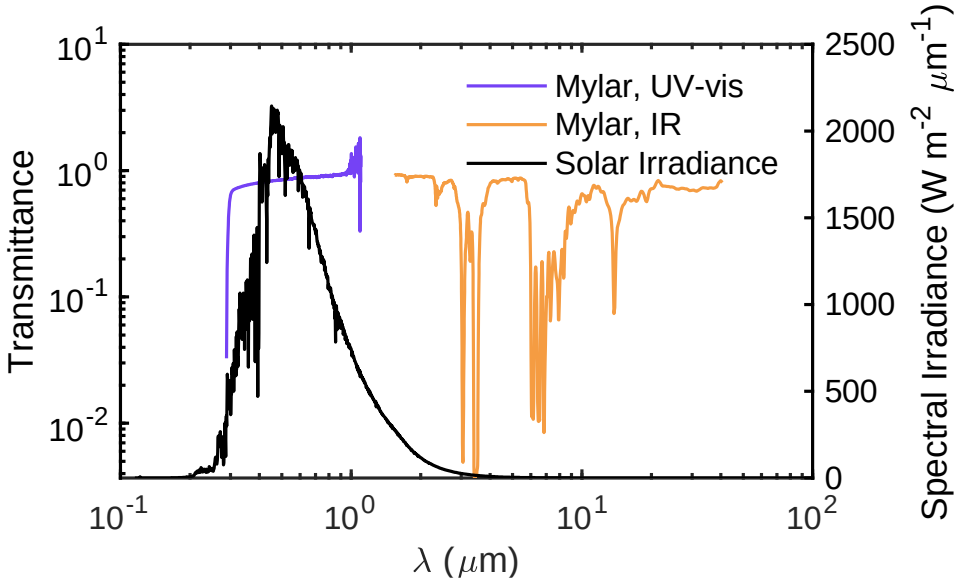

Fig. S8. Spectroscopy data of the pouch material. Transmissivity in the ultraviolet (UV) and visible electromagnetic spectrum were measured using an UV-visible spectrophotometer (Agilent G1103A). Transmissivity in the near-infrared region was measured using a [Charles what did you use]. Spectral irradiance data for the sun was adapted with permission from [128].

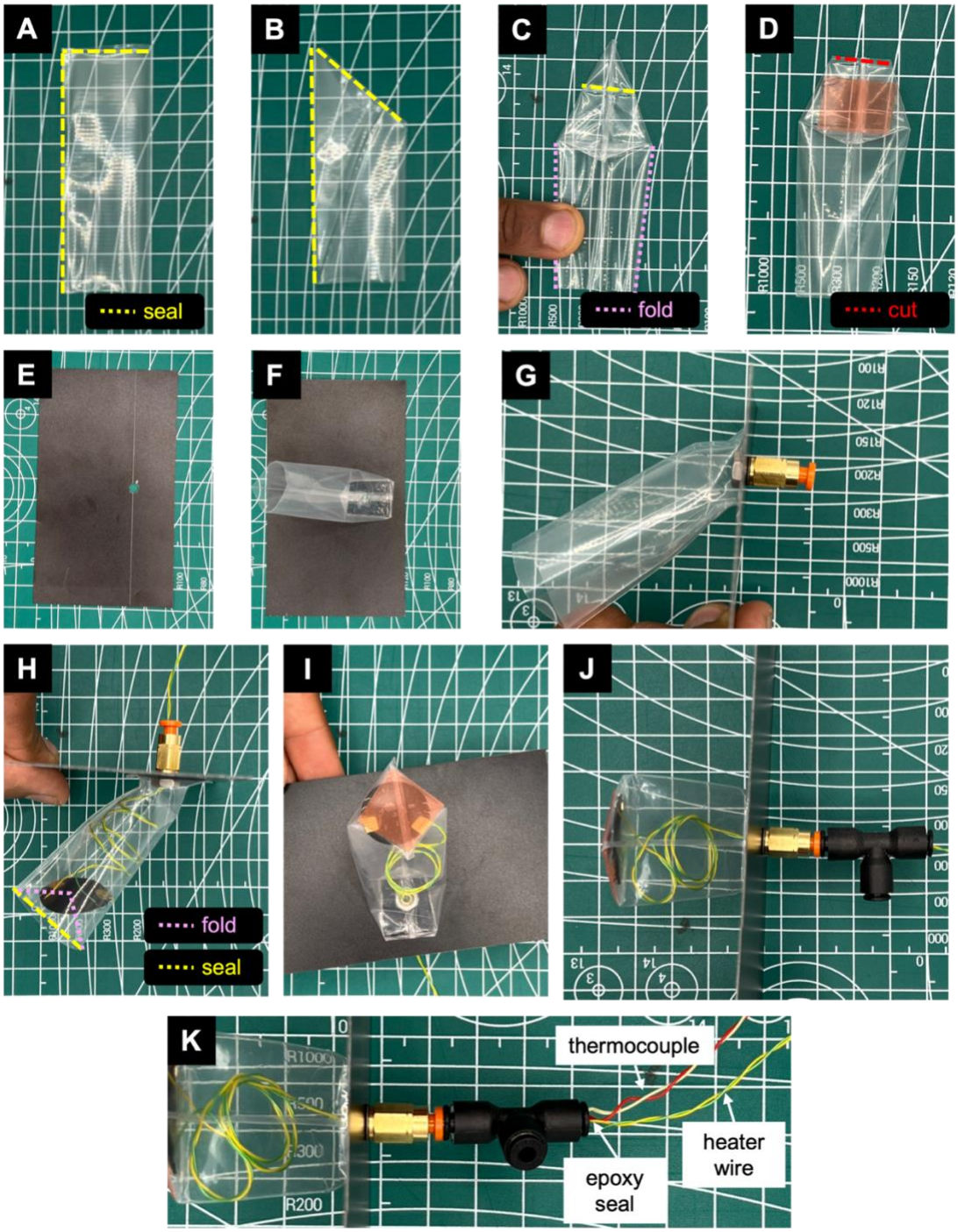

Fig. S9. Steps for fabricating the actuator for benchtop testing. (A) A 6.5 cm x 8.0 cm sheet of Mylar film was folded lengthwise and heat sealed along its length and at one end. **(B)** Thereafter, the pouch was heat sealed (Metronic, 8" Impulse Sealer) at a 45º angle from the lengthwise seal. **(C)** Pressing into the shorter (non-

heat-sealed) seam of the pouch, the pouch is then folded into a new shape. A heat seal is made 1 cm from the top of the pouch. **(D)** Mylar film above the heat seal in (C) is then cut off and a square of double-sided tape is applied just below the seal. **(E)** Then, 0.381 mm thick fiberglass was cut into a 6.5 cm x 11 cm rectangle. A hole was drilled at 2.0 cm x 5.5 cm from one corner of the rectangle. **(F)** The center of the pouch face with double-stick tape on it was aligned with the center of the hole in the fiberglass and adhered using the double-stick tape. Thereafter, a soldering iron was used to burn through the Mylar and double-stick tape—forming a hole of equivalent diameter to the hole in the fiberglass. **(G)** A threaded push-to-connect tube adapter (McMaster Carr, 5779K241) was then screwed into the fiberglass-facing side, and a 10-32” nut was threaded onto the end of the fitting on the Mylar-facing side**. (H)** The fabric heater described in Supplementary Text S5 was then inserted into the pouch and its wires fed through the tube fitting. The bottom of the pouch was then heat sealed with the heater inside. By pinching in against the seams of the pouch perpendicular to this heat seal, the bottom of the pouch was folded into a square shape. **(I)** The heater was nestled into this square shape—forming a small reservoir for liquid. **(J)** Then, a short piece of flexible PVC tubing, 1/8” in diameter (McMaster Carr, 5233K51) was used to connect the threaded push-to-connect tube adapter to a tee adapter (McMaster Carr, 5779K31). The heater wire was feed through the top of this tee adapter. (K) Finally, a fine gauge K-type thermocouple wire (Thermoworks, K-36X) was feed through the top of the tee adapter until the probe was flush with the 10-32” nut face. Thereafter, the top of the tee was filled with epoxy (Devcon, 5-

minute Epoxy) to prevent gas from escaping. One end of the tee was left unobstructed to later serve as a connection to the pressure transducer.

Text S7. Useful work measurement and efficiency calculations.

Using a combination of loads (i.e., “constant-torque” and “offset” mass in main text, Materials & Methods), the pressure-angle curve of the loaded pouch can be programmed. The free-body diagram in **Fig. S10**A illustrates this. Indeed, the combination of loads yields a variety of pressure-angle curves (**Fig. S10**B) that correspond with various temperatures of expansion (**Fig. S10**C). The mechanical work associated with each of these cycles is known by measuring the torque required during both the expansion (orange curves, **Fig. S10**D) and compression (blue curve, **Fig. S10**D) phases of the work cycle and integrating the area between the two. The experimental expansion and compression curves in **Fig. S10**D were measured by loading the testing setup with the desired loads and measuring the torque required to lift the load at discrete angles. Torque was measured using a force gauge (Mark-10, M3-100) attached to the hinge’s pulley via inextensible string.

All reported efficiencies, unless otherwise noted, are the percent ratio of output mechanical work to input electrical energy. Power is supplied to a conductive fabric heater via a benchtop voltage source (Kungber, 30V 10A DC Supply). Electrical energy input is known via the time integral of the product of voltage and current supplied (i.e., power) supplied to the conductive fabric heater. An Arduino Mega

2560 sampled current and voltage from an integrated power meter (Adafruit INA219) once every 50 ms with 1% full-scale precision. The time integral of this data was taken in MATLAB to determine energy input.

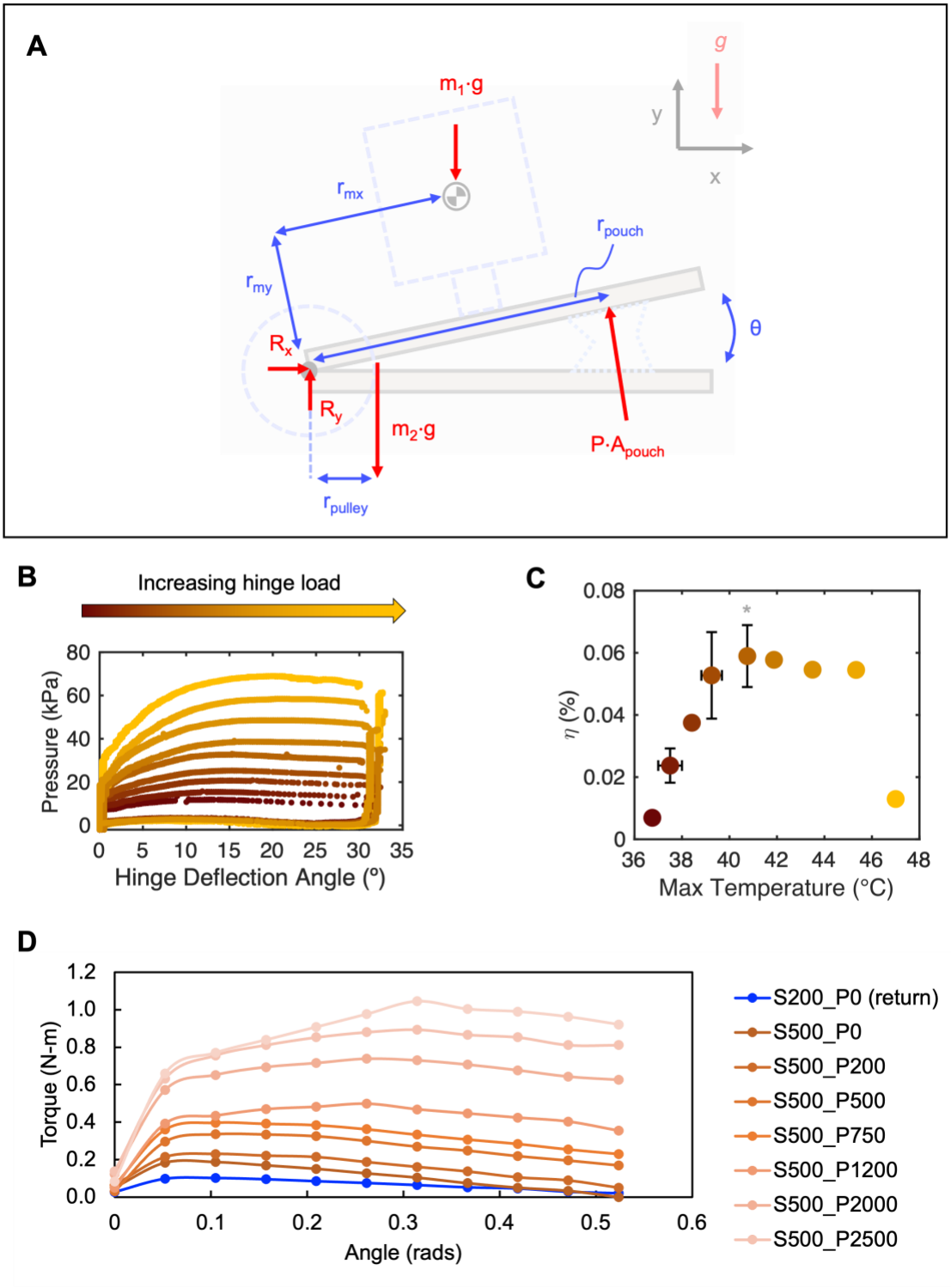

Fig. S10. Varying mechanical load enables cycle shape and operation temperature variance. (A) A free-body diagram of the purpose-built experimental

setup. This setup comprises a pouch inside of a loaded hinge. The pouch does pressure-volume work to lift the masses against gravity. The red arrows indicate reaction forces due to the offset mass ($m_1 g$), the constant-torque mass ($m_2 g$), reaction forces to the shaft (R_x, R_y) that allows the hinge to rotate freely, and the pressurized pouch (PA_{pouch}). The blue arrows indicate dimensions used to calculate deflection (θ) and torques (r). **(B)** Increasing hinge load results in increasing pressures of expansion and thus a pressure-angle curve with greater internal area. **(C)** The result of increasing pressure of expansion are increasing temperatures of expansion. **(D)** The torque required to complete both the varying expansion loads (orange curves) and the singular compressive load (blue curve) were measured experimentally to accurately determine the mechanical work completed in each pressure-angle cycle. In the legend, the numbers that follow “S” and “P” indicate the offset mass and the constant-torque mass in grams.

Text S8. Volume-angle correlations

Measuring vapor volume in a rigid syringe is relatively simple: the diameter of the syringe is constant and the height of the syringe plunger can be measured to determine volume. Conversely, measuring the volume of vapor in a soft/deformable constraint is challenging. As such, the purpose-built testing apparatus described in the main text measures angle as a convenient proxy for volume. Fig. S11 illustrates the relationship between fluid volume inside of the loaded actuator and the

measured hinge deflection angle. Here, angle is known by coupling a potentiometer to the hinge by way of a steel shaft (see main text, Materials & Methods). The dispensed/siphoned volume is known with ±1% accuracy by using a programmable syringe pump (New Era, NE-1000).

The data in Fig. S11 was collected by first loading the hinge with the desired expansion load, and then programming the syringe to dispense the desired volume of Novec 7000. Once full expansion (i.e., hinge angle deflection to 30º) is complete, the syringe was programmed to pause for 2 seconds while the offset and constant-torque masses were manually changed to their compression values. Thereafter, the compressive loads acted on the pouch as Novec 7000 was siphoned out of the pouch back to the initial starting volume.

In all tests, the expansion load on the hinge was varied while the compressive load was held constant. During expansion, an offset mass of 500 g was used, while the constant-torque mass was varied. In the legend of Fig. S11, the numeric values that follow “P” indicate what constant-torque mass was used during expansion. During compression for all runs, an offset mass of 200 g and a no constant-torque mass were used. The loads tested correspond directly with those used to produce the curves in Fig. S10B.

Curves in Fig. S10 suggest that volume and angle are linearly correlated over most of hinge deflection. However, there is some hysteresis observed (e.g., <4 mL) which

can likely be attributed to a combination of stretching of the pouch walls and/or volume inaccuracies due to deformation of the soft rubber syringe plunger responsible for dispensing/siphoning.

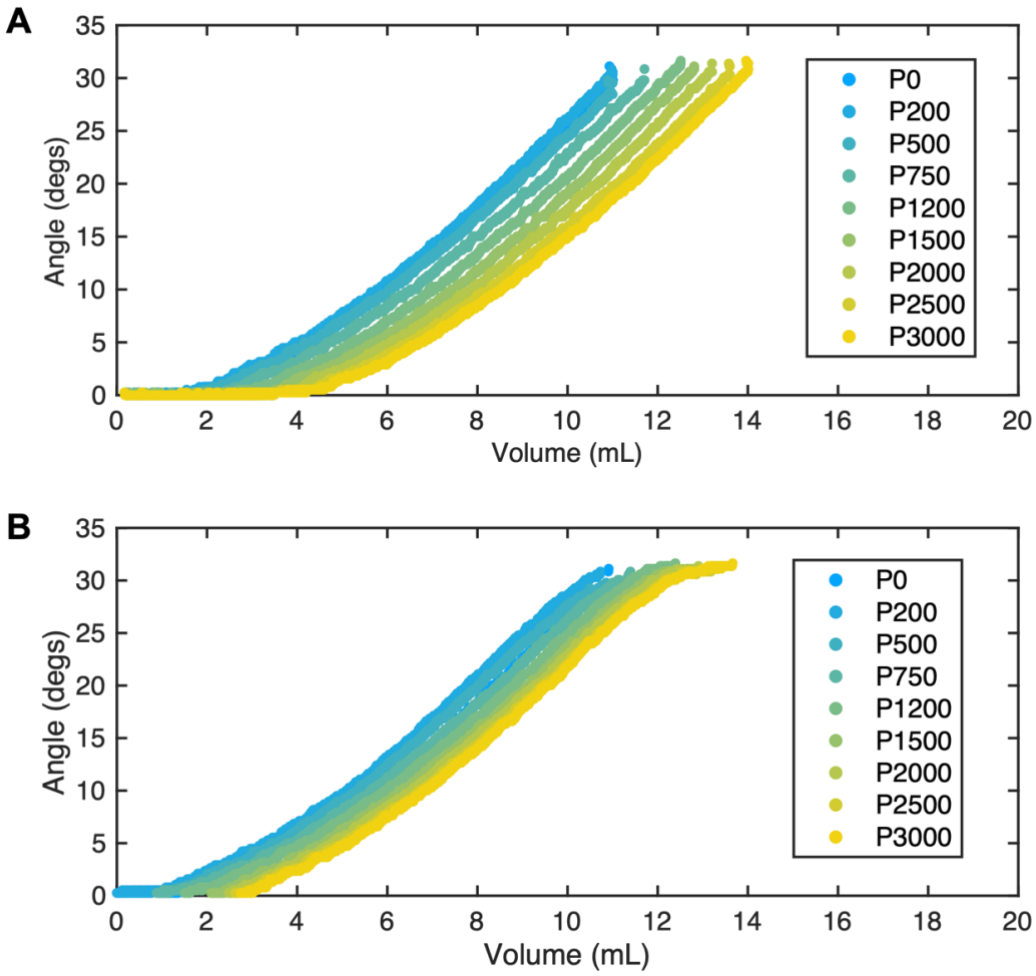

Fig. S11. Volume-angle correlations for various mechanical loads. The angle-volume relationship is linear over most values, however, there is some load-dependent hysteresis exhibited by the system. This hysteresis may be attributed to mild stretching of the soft pouch used in testing and/or volume inaccuracies due to deformation of the soft rubber syringe plunger responsible for dispensing/siphoning.

Text S9. Actuator fabrication for the solar-powered roller.

Each leg of the solar-powered roller is equipped with a pouch. Instructions for creating these pouches can be found in Fig. S12.

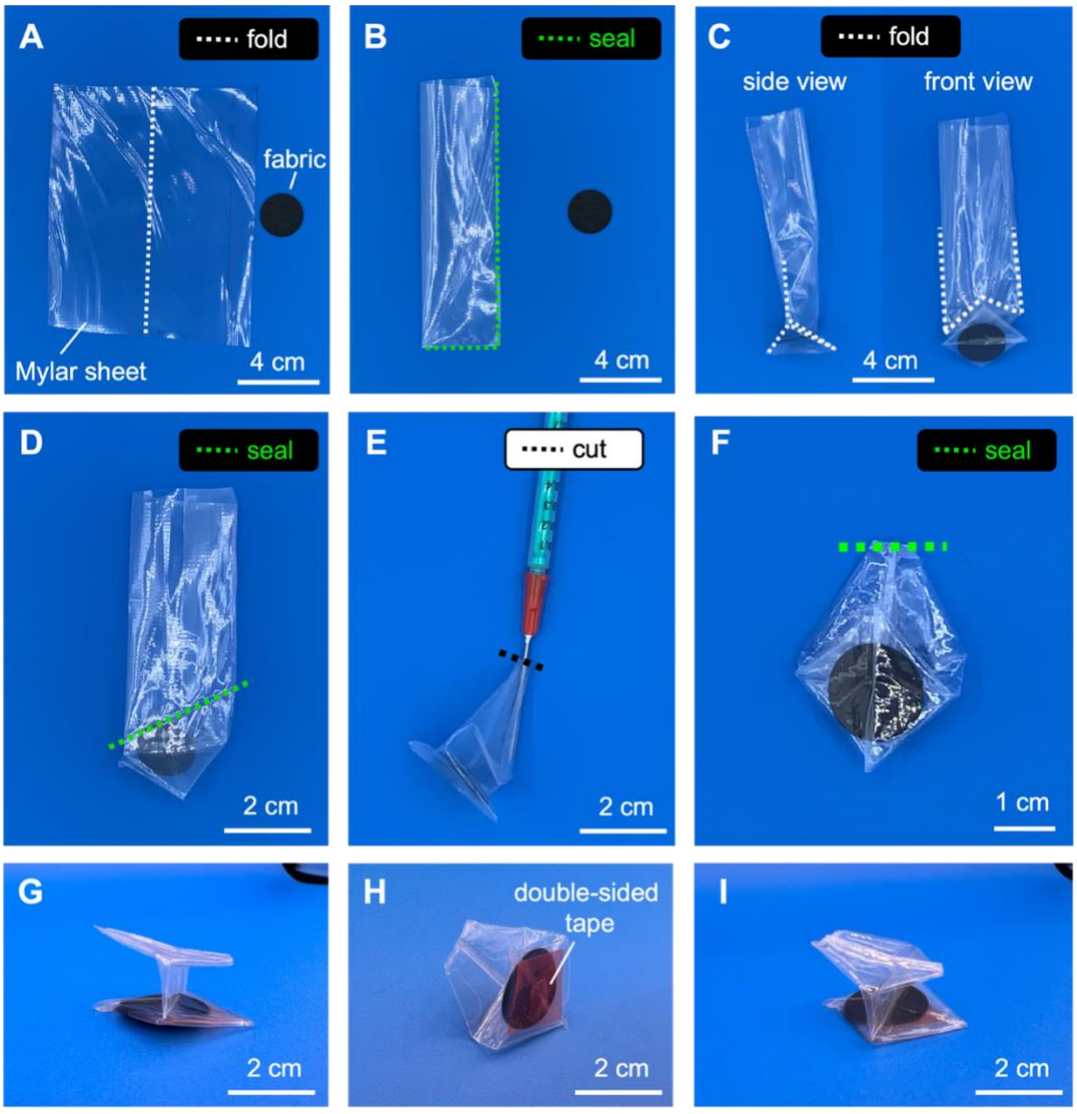

Fig. S12. Pouch fabrication for the solar-powered roller. (A) A 6.5 cm x 13 cm rectangle of Mylar film was folded lengthwise, and then **(B)** heat-sealed (Metronic, 8”

Impulse Sealer) along a long edge and a short edge to form a tube with one open end. **(C)** Thereafter, the bottom of the pouch was folded to create a square bottom by pressing in at each of its long sides. The black disk of fabric responsible for sunlight absorption was nestled into the square chamber at the bottom of this pouch. **(D)** By pressing into the newly folded long seams (white dashed lines in (C)) another square chamber just above the previous one was then formed. A heat seal was then made at 45º from one of the edges of the long seam. **(E)** Then all heat seal seams were aligned with one another by massaging the pouch material just below the new heat seal. The result of this step is a diamond-like chamber, parallel to the bottom square chamber, which has one long triangular end and one short triangular end. The longer triangular end was cut ~2 mm from its tip to allow for ~0.8 mL of Novec 7000 to be injected. **(F)** Then air was pressed out of the pouch manually and the pouch was heat sealed at the cut end. **(G)** Image depicting a side view of the finished product. **(H)** Double-sided tape was placed both on the bottom and top of the pouch to allow it to adhere to the fiberglass leg and the acrylic plate used in the roller (see main text Materials & Methods). **(I)** An isometric view of the finished product.

Text S10. Convection coefficient characterization.

One of the simplifying assumptions that enables the derivation of the rectangular cycle with heat losses above is that has constant lumped heat loss coefficient. Through experiment, however, we found that the STAPA (i.e., the Mylar pouch used

in testing) used actually behaves like a thermal switch—transitioning from a low loss to a high loss state depending on the hinge deformation angle, and more specifically on the exposed surface area of the pouch during deflection.

To characterize the angle-dependency of the convection coefficient, the pouch was filled with 2.64 mL of Novec 7000. The fabric heater the pouch encapsulated was supplied with 1.3 W of energy. The experiment took place in a climate-controlled room (T_{amb} = 19 ± 0.25 ºC). Three angles were tested consecutively by blocking the hinge at each (Fig. S13A). The pouch temperature was observed until it reached a constant saturation value (Fig. S13B). We found that the convection coefficient increases roughly linearly with increasing hinge deflection angle (Fig. S13C).

The lumped loss coefficient is known by taking the ratio of the input power and the difference in temperature between the pouch and the ambient environment:

$$h_{loss} = \frac{\dot{q}_{in}}{T - T_{\infty}}$$

We note, however, that the convection coefficient values vary based on which temperature is used for its calculation. In Fig. S13B “T_in” is the temperature measured by the thermocouple that is at the top of the interior of the pouch. “T_out” is the temperature measured by the thermocouple on the bottom exterior of the pouch—closest to the fabric heater inside of the pouch. These temperatures correspond to the curves in Fig. S13C. For our theoretical calculations, we averaged

across both temperature and hinge angle, using a nominal loss coefficient value of 0.0629 W K^{-1}.

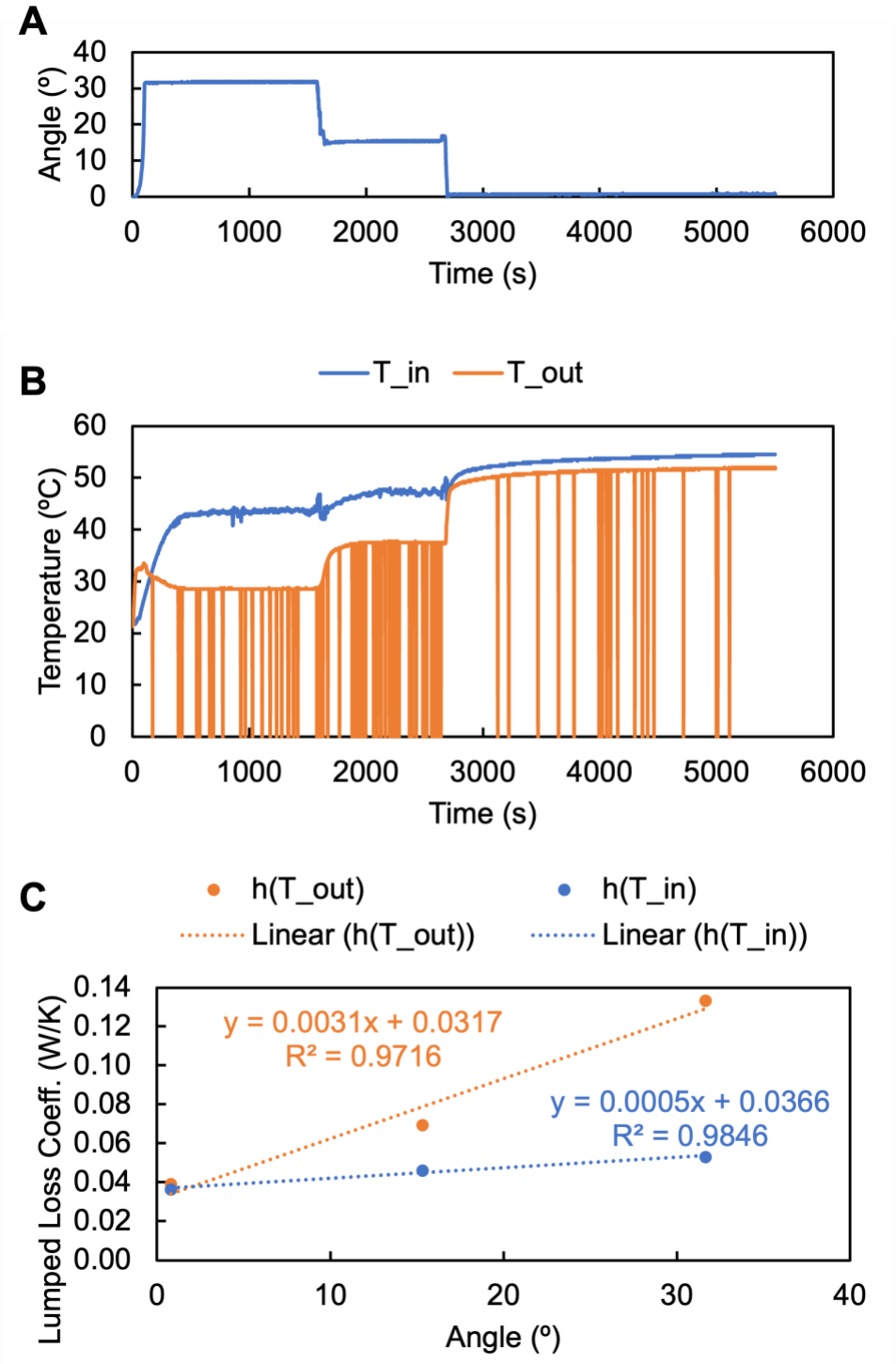

Fig. S13. Lumped heat loss coefficient characterization. (A) The pouch was loaded inside of the purpose-built mechanical testing apparatus described in the

Materials & Methods in the main text and fixed at three discrete angles: 0.791, 15.3, and 31.6º. **(B)** Thereafter, temperature at each angle was measured until it reached saturation. “T_in” is the temperature measured by the thermocouple that is at the top of the interior of the pouch. This thermocouple undergoes significantly more temperature fluctuation due to fluid condensing on it. “T_out” is the temperature measured by the thermocouple on the bottom exterior of the pouch—closest to the fabric heater inside of the pouch. Note that zero values on this curve are the result of “NaN” values produced by the thermocouple. Differences between “T_in” and “T_out” are large at large angle values due to thermal gradients between the top and bottom of the pouch; however, these gradients diminish as the hinge angle approaches zero and the pouch is compressed nearly flat. **(C)** The lumped loss coefficient varies linearly with hinge deflection angle. Note also that the value of the lumped loss coefficient depends on what temperature is used to calculate it. A nominal curve between the two may be more representative of actual losses.

Text S11. Loss accounting for the benchmark STAPA tests.

In the main text, we describe three methods for minimizing losses in soft heat engines for robotics: (1) identify and operate at the temperature optimum of the system, (2) maximize power input, and (3) maximize volume expansion. These three methods can be leveraged to minimize cycle shape losses and heat losses. In Fig. S14, we quantify how energy is allocated to losses versus useful work using

representative values. Generally, percent efficiencies are first calculated and then multiplied by the input energy to determine energy allocation to each loss.

"T_h Limit 1" is the loss attributed to operation in contact with a non-infinite heat reservoir. Instead, the hot reservoir temperature, T_h, is set by the thermal degradation (i.e., maximum) temperature of the conductive fabric used in the benchtop experiments—i.e., 250 ºC. "T_h Limit 1" is the product of input energy and the Carnot efficiency using this maximum temperature for the hot reservoir temperature and a cold reservoir temperature, T_c, equal to 20 ºC. "T_h Limit 2" is the loss attributed to operation at the actual system temperature. Here, the hot reservoir temperature, T_h, is known by reverse calculating temperature based on the vapor pressure relationship for the working fluid, Novec 7000:

$$P = EXP\left(-\frac{3548.6}{(T + 273.15)} + 22.978\right)$$

Where P is the system's absolute pressure, and T is the system temperature in degrees Celsius. "T_h Limit 2" is the product of input energy and the Carnot efficiency of a heat engine operating between the system temperature and a cold reservoir temperature, T_c, equal to 20 ºC. "T_c Limit" is a loss due to a working fluid whose boiling temperature is above ambient. When this is the case, the cold reservoir temperature is now equivalent to the boiling temperature of the fluid. "T_c Limit" is the

product of input energy and the Carnot efficiency where T_h is the system temperature and T_c is the fluid's boiling temperature.

"Cycle Shape" loss is the loss associated with a cycle shape that deviates from the Carnot cycle. This is calculated via the product of the input energy and the difference in efficiency between the Carnot cycle and the rectangular cycle with equivalent high and low pressures. "Heat Loss" is the loss associated with adding heat losses to the rectangular cycle. "Heat Loss" is calculated via the product of the input energy and the difference in efficiency between the ideal rectangular cycle and the rectangular cycle with heat losses. "Useful Work" is the mechanical work that was experimentally measured necessary to lift the masses that load the hinge in the experimental setup (see main text, "Materials & Methods" for details). "Non-Useful Work" is the difference between the pressure-volume work and the "Useful Work"; it may be attributable to material hysteresis, friction, or other parasitic forces. The pressure-volume work is known by calculating the area inside of the pressure-volume curve. Finally, "Unmodeled Loss" is the remainder of energy that has not been accounted for. The sum of these losses is the input energy, which sets the upper bound for each stacked bar plot in Fig. S14 below.

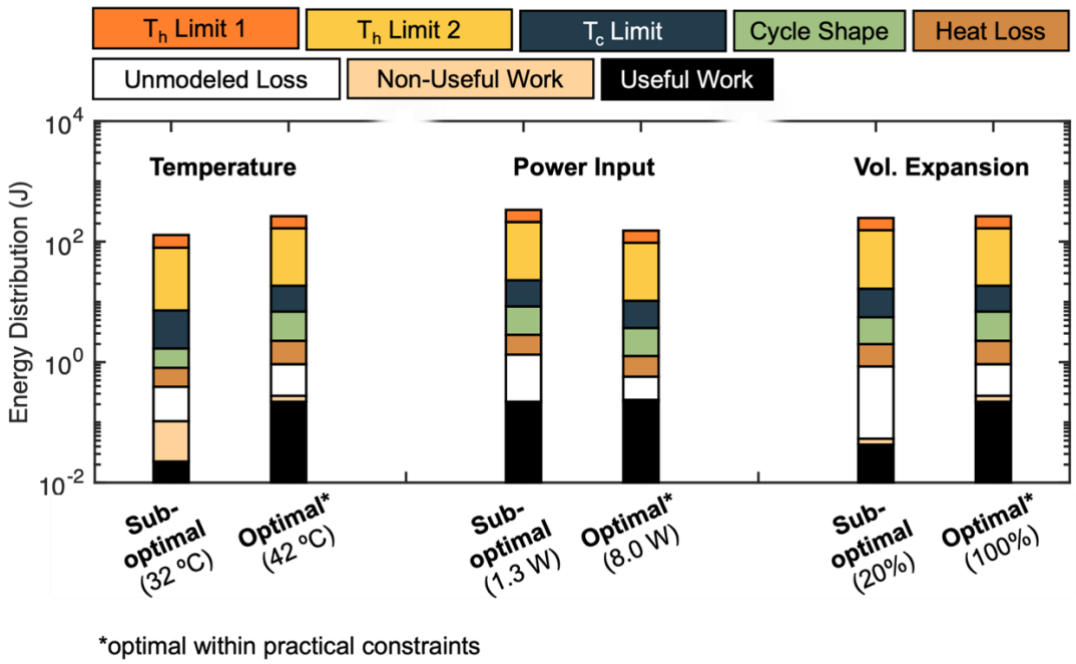

Fig. S14. Energy distribution in the sub-optimal versus optimal (within practical constraints) cases for each of the three tested variables: temperature, power input, and volume expansion ratio. As the mechanical load (and thus, temperature) was varied, power input was fixed at 1.3 W and the volume expansion ratio was fixed at 4.63. As power input was varied, the mechanical load was held constant and the volume expansion ratio was fixed at 4.63. As volume expansion ratio was varied, the power input was fixed at 1.3 W and the expansion load was held constant.

Several conclusions can be drawn from Fig. S14. First, temperature limit losses (i.e., “Th Limit 1,” “Th Limit 2,” and “Tc Limit”) comprise >97% of losses in all cases. As is discussed in Supplementary Text S2, minimizing these losses offers the greatest opportunity for efficiency improvement, however, it is challenging to do so. Second, going from the “Sub-optimal” to “Optimal*” case for all three variables improves

efficiency. This further illustrates the utility of the three predicted insights discussed in the “Results” section of the main text. For the case of varying power input, no change in useful work is observed because the same mechanical load cycle is tested in both cases, however, the “Optimal*” case requires less input energy to do the “Useful Work.” Third, “Cycle Shape” losses and “Heat Loss” remain relatively constant for both the “Sub-optimal” and “Optimal*” case across all variables. Finally, both “Unmodeled Loss” and “Non-Useful Work” decrease when going from the “Sub-optimal” and “Optimal*” case across all variables. Unmodeled loss is potentially attributable to heat losses not captured by the theoretical model. For example, we assumed a nominal loss coefficient of 0.0629 W K^{-1} in theory, however, we show in Fig. S13 that the loss coefficient varies as a function of hinge deflection angle. The “Non-Useful Work” may be material hysteresis or system friction whose relative energy consumption we predict would decrease with increasing load—as is the case for the temperature “Sub-optimal” versus “Optimal*” case.

Text S12. Conservation of predicted trends between experiment and roller.

In our benchtop, lab-based experiments we used an input power of 1.3 W and estimate a lumped loss coefficient of roughly 0.0629 W K^{-1}. Conversely, the roller which was tested outdoors uses significantly more power from solar harvesting and is subject to higher losses due to wind. We estimate the robot intakes 15.66 W of power and endures a loss coefficient of 0.314 W K^{-1}. The trend between the actuator

the roller is still conserved and as such the predicted insights from theory (discussed in the Results section of the main text) still apply.

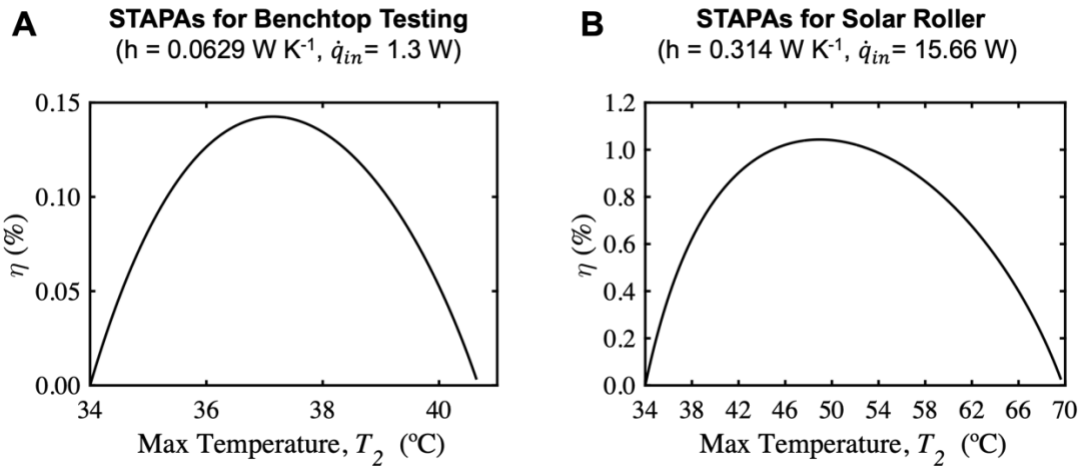

Fig. S15. Comparison between the predicted temperature optimum for the STAPA used in benchtop testing and that in the solar roller. Despite differing input parameters *h* and $\dot{q}_{in}$, the trend/existence of a temperature optimum is conserved. (A) Using a nominal loss coefficient of 0.0629 W K^{-1} and a measured input power of 1.3 W, we find a temperature optimum ~37 ºC. **(B)** Using an estimated loss coefficient of 0.314 W K^{-1} and a measured input power of 15.66 W, we find a temperature optimum ~49 ºC.

Text S13. Identifying the temperature optimum of the roller.

We tested the influence of pouch contact area on roller efficiency by building a weight-matched cardboard replica of our solar-powered roller (Fig. S16A-C) and

measuring its flip time when using different pouch sizes under artificial light (Fig. S16D,E). The roller replica was placed roughly 50 cm from the base of the light and the light was angled such that it could be concentrated through the Fresnel lens and onto the pouch of interest.

Care was taken to ensure that the weight was axisymmetric. The pouch dimensions working fluid volume were scaled based on the lay-flat tube width as shown in Table S1. The same light intensity and diameter disk of absorbing fabric was used in all tests to ensure equal energy input. Each pouch was inserted into the leg of the replica roller and taped into place using double-sided tape on both the top and the bottom of the pouch. The light was turned on and the flip time was measured as the time from when the light was turned on to the time when the roller performed one flip.

Table S1. Properties used to test the effect of pouch contact area on roller flip time.

LayFlat Width (cm)	Contact Area (cm^2)	Novec Vol. (mL)	Avg. Flip Time (s)
2.00	4.0	0.50	47.9
4.00	7.6	1.19	46.6
5.00	11.6	2.32	90.5
7.45	26.0	7.66	122.3

The results of this investigation suggest the potential existence of a temperature optimum (Fig. S16E); however, the right side of the efficiency peak could not be tested due to practical manufacturing constraints. The plot in Fig. S16E is analogous to the temperature versus efficiency plots presented in the main text. Pressure and temperature directly correlated by the vapor pressure relationship for our working fluid (Novec 7000). As such, increasing the inverse of pouch contact area should track roughly linearly with increasing temperature. The frequency of a a flip is linearly related to efficiency by the following equation:

$$\eta = \left(\frac{1}{t_{flip}}\right)\frac{W_{flip}}{\dot{q}_{lamp}}$$

Here, $\dot{q}_{lamp}$ is the power of the lamp supplying light energy, W_{flip} is the fixed amount of work required for a flip, and t_{flip} is the measured amount of time for the robot to flip.

While we attribute the potential presence of an optimum to operating at the ideal temperature, we also scaled the input volume with the increasing pouch size (see Table S1). The additional thermal mass associated with increasing volume may be a competing effect that sets the flip time.

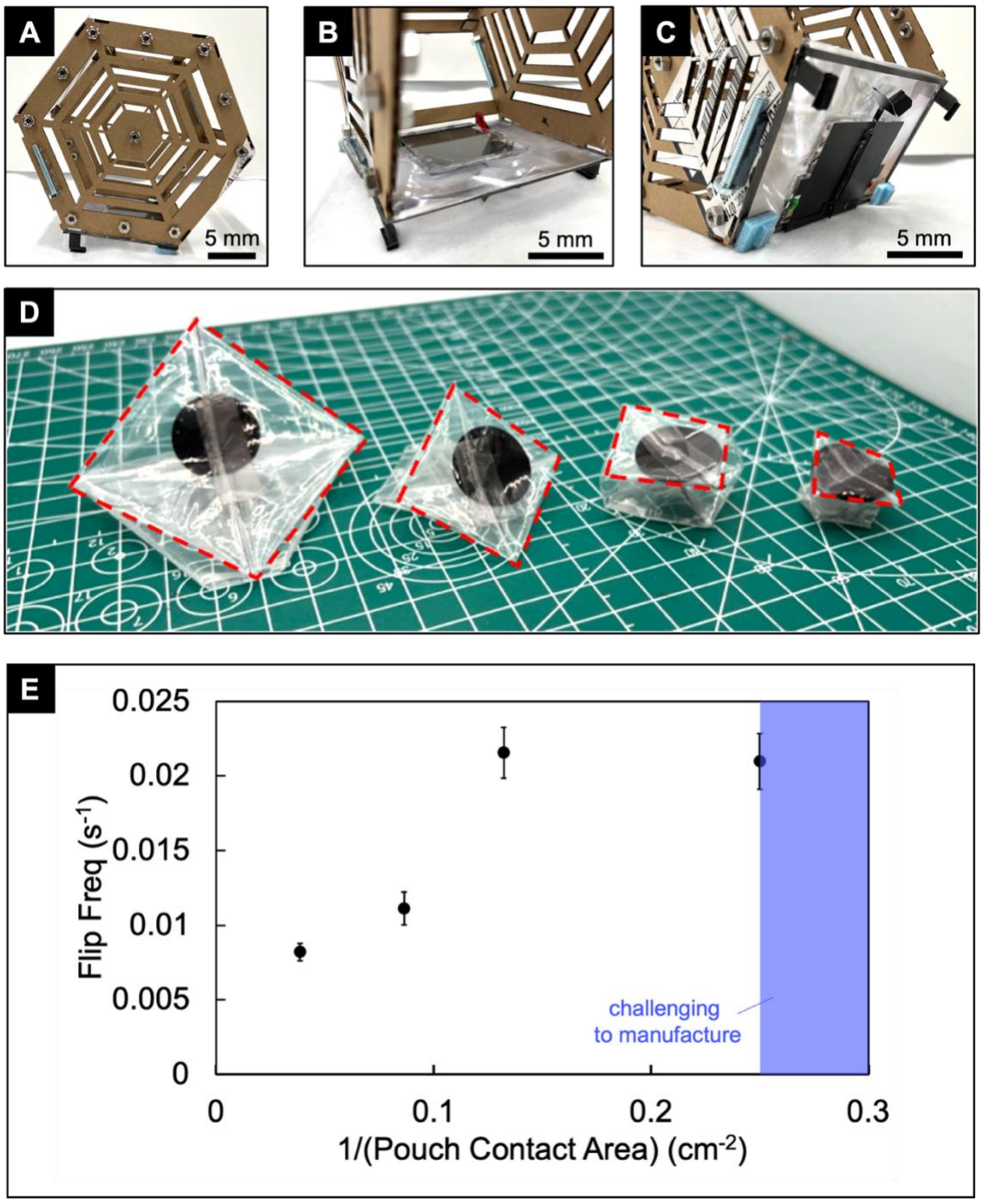

Fig. S16. A weight-matched cardboard replica of our roller enables testing of efficiency versus operating temperature. (A) Side view of the weight-matched replica illustrates the use of nuts and bolts to distribute weight evenly around the rolling axis (as is the case in the real roller). (B) A closeup view of the replica's leg

from the top. (C) A closeup view of the roller's leg from the bottom. The fiberglass leg was made large to accommodate the large pouch sizes. (D) Image depicting the various pouch contact areas tested. Each square on the green mat is 1 cm x 1 cm. (E) Results of this investigation suggest a potential temperature optimum for the solar-powered roller. On the y-axis, flip frequency serves as a proxy for efficiency. On the x-axis, the inverse of pouch contact area serves as a proxy for temperature. We were unable to test below a critical pouch size due to practical manufacturing constraints.

Text S14. Dynamic hinge design and testing.

Dynamic hinges in the shape of gingko leaves were designed to give the roller stiffness that allows it to maintain alignment with the sun and transduce force during a flip, but also load-dependent compliance to resist mechanical crushing and deformation (Fig. S17). These hinges were 3D printed from flexible filament (Ultimaker 2, NinjaFlex) and equipped with 28.6 N neodymium magnets (K&J Magnetics B662). In compression—i.e., $\theta_{hinge} < 120°$ in Fig. S17A—thin slits in the hinges allow them to fold nearly flat. In its undeformed state, the hinge rests at $\theta_{hinge} = 120°$ (Fig. S17B). In extension——i.e., $\theta_{hinge} > 120°$ in Fig. S17C—the magnets resist that initially hold the hinge flaps together are separated and the pouch can deform nearly to $\theta_{hinge} = 180°$.

Fig. S17D depicts the torque versus angle of deflection, θ_{hinge}, curve. Fig. S17E illustrates the method used to collect the data in Fig. S17D. The torque-angle curve illustrates the effects of buckling and magnet force in compression and extension, respectively. In compression (i.e., $0° < \theta_{hinge} \leq 120°$) the walls of the dynamic hinge perpendicular to angular deflection initially resist compression. At some critical deflection angle (~ $\theta_{hinge} \sim 55°$), small slits allow the walls to buckle out of plane however, resulting in a drop in torque. The rise in torque that follows is the result of the walls being compressed against the rest of the hinge.

In extension (i.e., $120° < \theta_{hinge} \leq 180°$), the attractive force of the magnets inside the hinge initially resist angular deformation. However, at some critical deflection angle (~ $\theta_{hinge} \sim 145°$), the magnets begin to separate, causing a drop in torque. The rise in torque that follows this drop is due to the resistance of the spine that joins the two parts of the hinge.

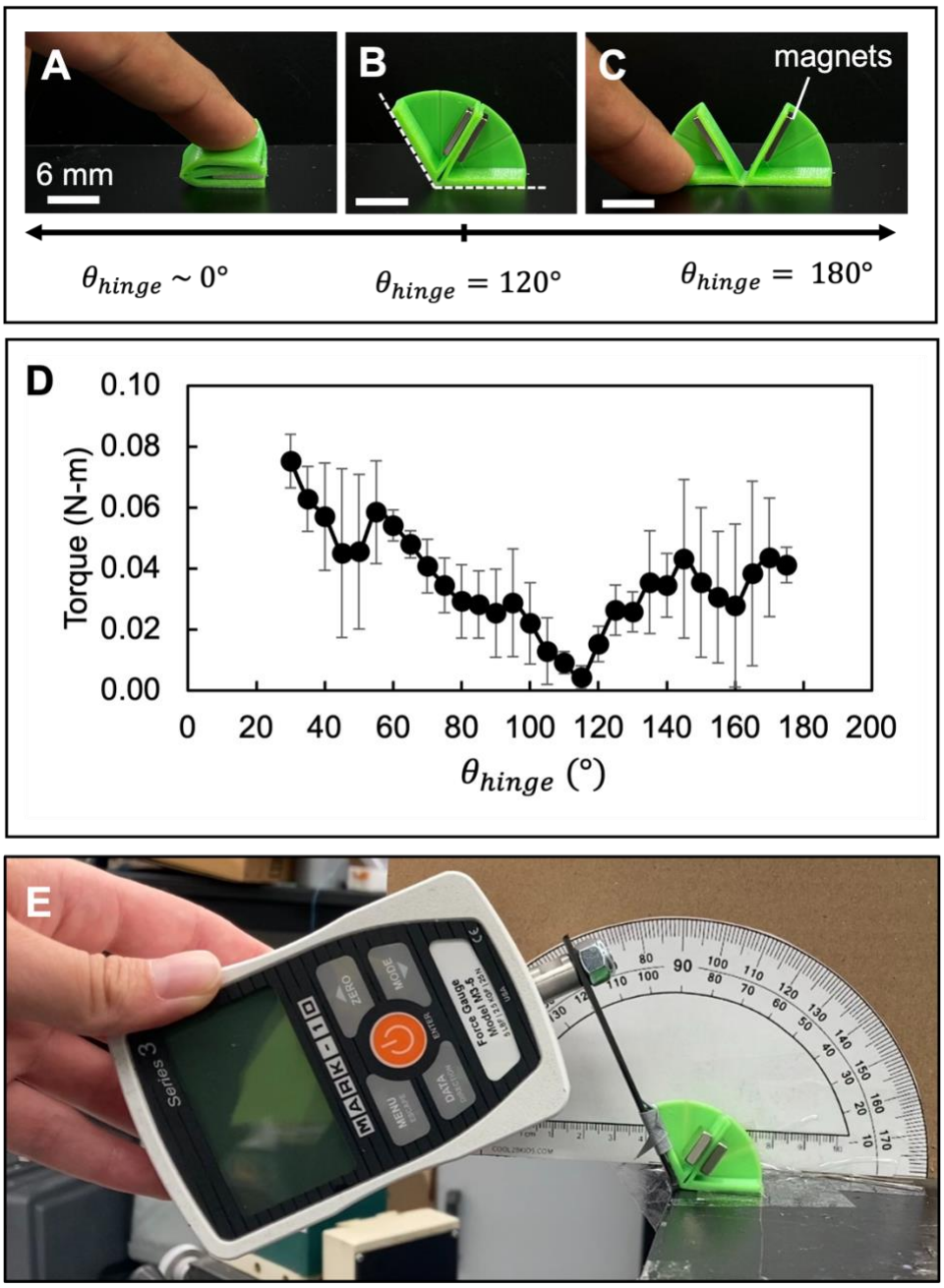

Fig. S17. Mechanical testing of the dynamic hinges used in the solar-powered roller. (A) Illustrating the hinge in compression, (B) with no load, and (C) in extension. (D) The torque-angle curve of the hinge reveals two dips in torque that correspond with designed events. In extension (i.e., $120° < \theta_{hinge} \leq 180°$), this is due to the magnets separating. In compression (i.e., $0° \leq \theta_{hinge} < 120°$), this is the

result of walls of the hinge buckling. (E) Method for gathering torque-angle data. Torque measurements were performed using a Mark-10 M3 force gauge. This force gauge was bolted to a stiff carbon fiber beam that was then adhered using superglue to one face of the hinge. A video of deflecting the hinge was recorded on an iPhone 13 video camera. Torque values from the force gauge as well as angles observed on a protractor just behind the hinge were recorded to produce the data in (D).

Text S15. Calculation of roller average efficiency.

The solar-powered roller described in the main text was set outdoors and allowed to flip over the course of several minutes (see Supplementary Video 1). To provide an estimate of the average efficiency of the roller, the power inputs and outputs are quantified. Power input is known based on the solar flux measured by a weather station (Ambient Weather WS-8480 FALCON, see Supplementary Text S17 for details). The power output is ratio of the work required for a flip (Fig. S18A,B) and the amount of time each flip takes (Fig. S18C). The efficiency is calculated via the following equation:

$$\eta_{pouch} = \left(\frac{W_{flip}}{t_{flip}}\right)\frac{1}{\dot{q}_{sun}}$$

Here, W_{flip} is the work required for a flip, t_{flip} is the amount of time required for a flip, and $\dot{q}_{sun}$ is the input power of the sun.

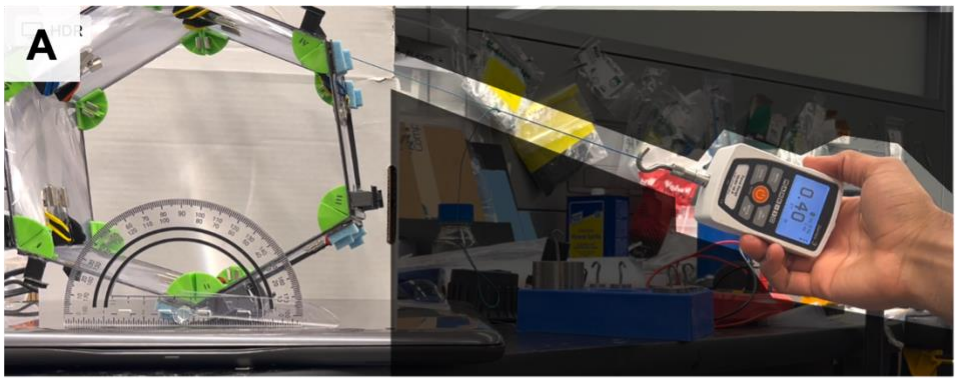

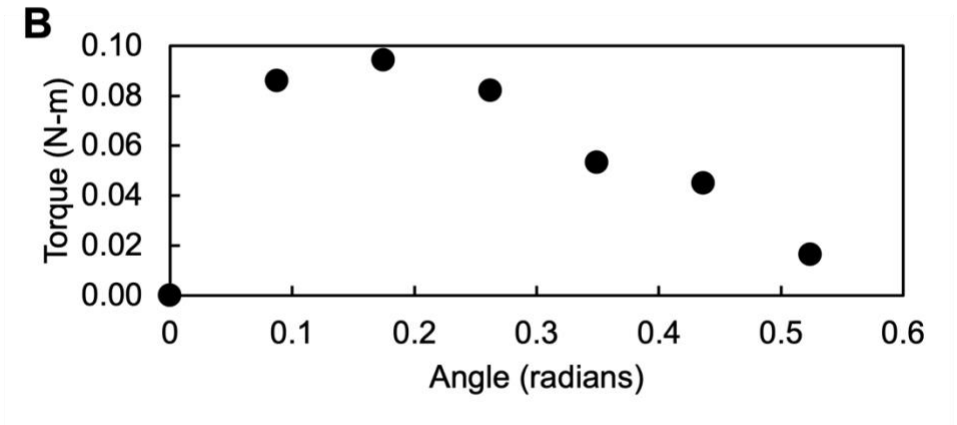

C

Flip No.	Heating Time (s)	Flip Time (s)	Work of Flip (J)	Flip Power (mW)	Efficiency (%)
1	17.53	13.23	0.0322	2.43	0.0155%
2	17.68	3.31	0.0322	9.73	0.0621%
3	31.50	13.53	0.0322	2.38	0.0152%
4	29.21	7.92	0.0322	4.07	0.0260%
5	27.84	8.58	0.0322	3.75	0.0240%
6	21.21	9.57	0.0322	3.36	0.0215%
				Average Efficiency:	***0.0274%***

Fig. S18. Roller efficiency calculation. (A) Method for calculating the torque-angle curve of a robot flip. Torque was measured using a force gauge (Mark-10, M3) connected to the robot body via inextensible string. Great care was taken to ensure the string was always parallel with the robot face—ensuring a perpendicular lever arm. A video of the experiment allows both force readings from the force gauge and angle measurements from the protractor to be recorded simultaneously. (B) A plot of

the torque-angle curve of a robot flip. The integral under the curve is equivalent to the work required to complete a flip. (C) A table of values used to calculate the efficiency of each actuator in the roller demonstration. “Heating time” is the amount of time that the pouch was irradiated before any motion was observed. “Flip time” is the amount of time required for the roller to complete the flip. “Work of Flip” is the integral under the torque-angle curve in (B). “Flip Power” is the “Work of Flip” value over the “Flip Time” value. “Efficiency” is the “Flip Power” over the solar input power—i.e., a constant value of 15.6 W, estimated based on solar flux measurements described in Supplementary Text S17.

Text S16. Demonstrations of compliance and robustness.

The dynamic hinges described in Text S14 enable load-dependent deformation of the solar-powered roller. This enables robustness to mechanical deformation such as drops or crushing (Fig. S19).

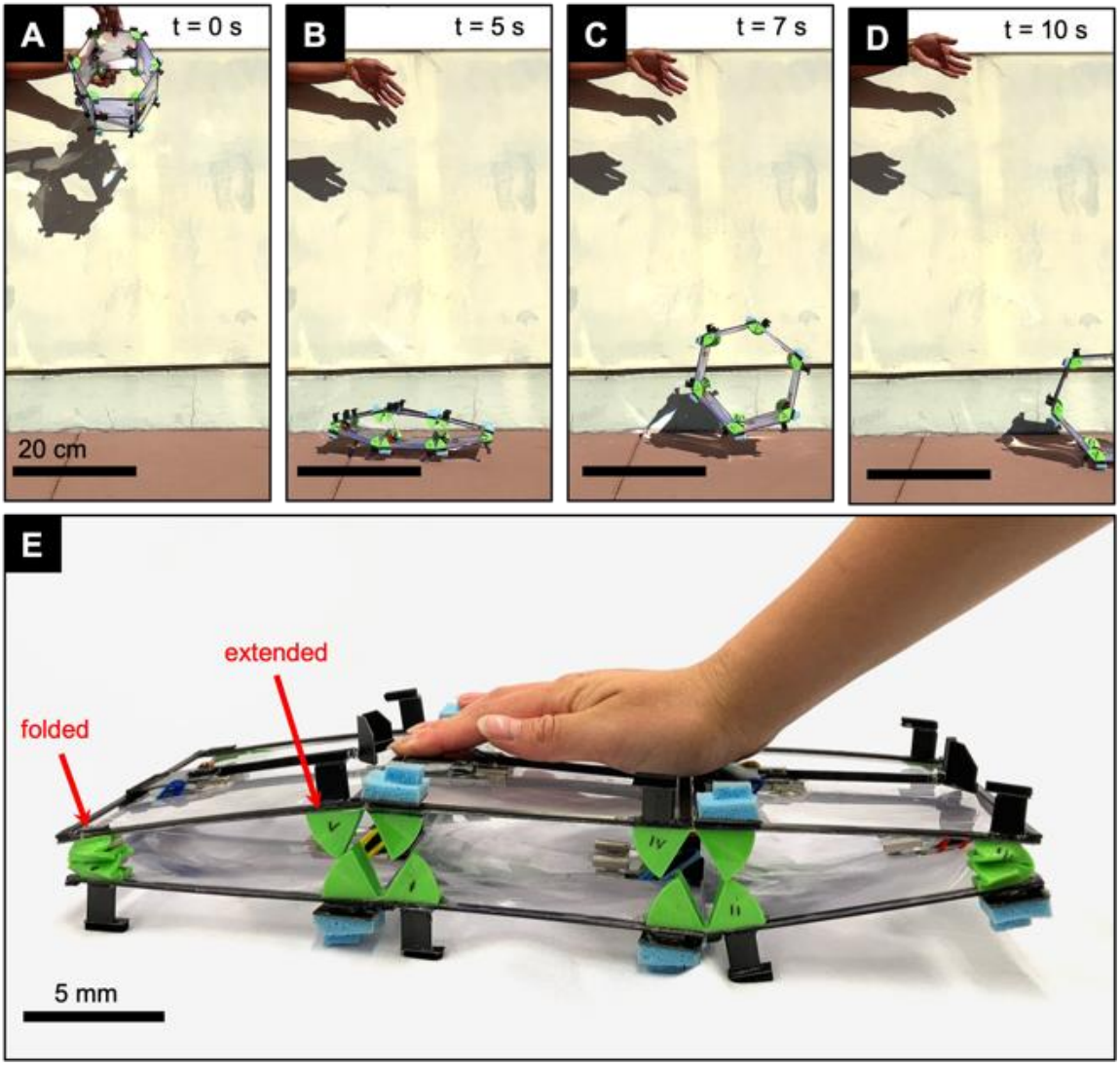

Fig. S19. Dynamic hinges enable resistance to mechanical deformation. (A-D) Stills taken from a video of the roller being dropped. The roller is dropped from ~92 cm (A). The stiff-soft nature of the dynamic hinges offer compliance upon impact to prevent damage to the roller (B), but also enough springiness and stiffness for the robot to bounce, regain its shape (C), and roll out of frame (D). (**E**) Further demonstrating the capacity of the stiff-soft hinges, we crush the robot virtually flat. Here, it is evident why the compliant hinges require compliance both in extension and compression.

Text S17. Outdoor testing of the solar-powered roller.

The roller was placed outdoors in Santa Barbara, CA and allowed to complete more than full cycle of rotation (i.e., seven flips). Wind, ambient temperature, and light flux were monitored (Fig. S20) using a commercially available weather station (Ambient Weather WS-8480 FALCON). Temperature was monitored using an internal thermometer (Fig. S20A), wind with a wind vane (Fig. S20B), and solar flux via a horizontal plate collector (Fig. S20C, "measured" curve). To gather a more accurate estimate of incident light flux, we perform a cosine transformation on each flux measurement based on the angle of the sun and the angle of our lenses:

$$q_{est} = \frac{q_{meas}}{\cos(\pi - \theta_{sun}) * \cos(\pi - \theta_{sun} - \theta_{lens})}$$

Where q_{est} is the estimated solar flux into the roller lens, q_{meas} is the measured solar flux, θ_{sun} is the angle of the sun above the horizon, and θ_{lens} is the angle of the lens above the horizon (i.e., 60º or $\pi/3$ radians). All angles are in radians.

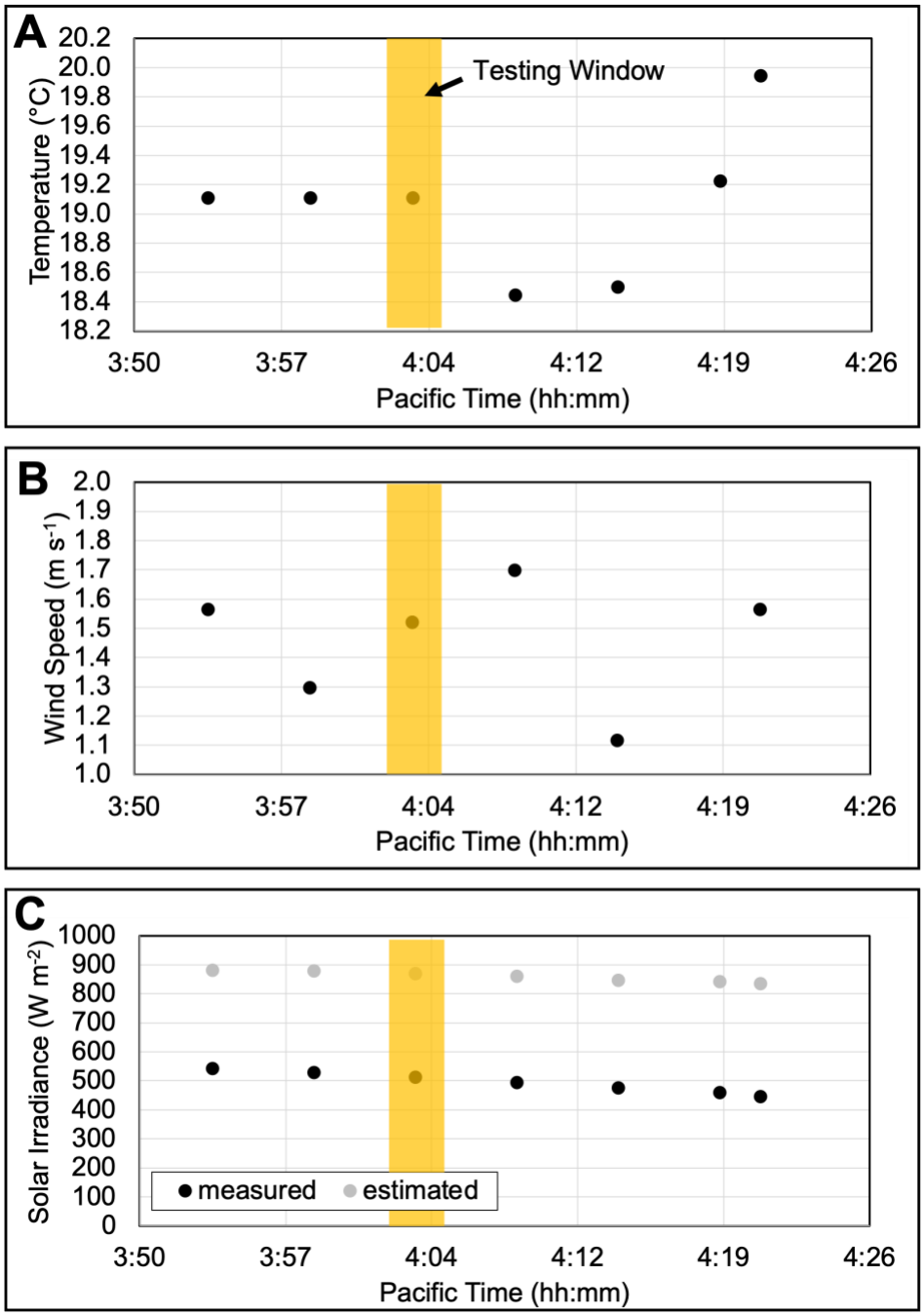

Fig. S20. Environmental conditions at the time of roller testing. In the main text, we demonstrate our roller performing seven flips—i.e., more than one full rotation. The environmental conditions during the window of testing were collected using a weather station every five minutes and are presented here. (**A**) The ambient air

temperature was roughly constant at 19.2 ℃. (**B**) Wind speed varied significantly during testing, but based on the data is estimated to have been between 1.3-1.7 m s^{-1}. (**C**) Solar irradiance was measured using a flat plate collector (see “measured”)—i.e., parallel with the ground. However, each lens of the robot is oriented at sixty degrees above horizontal, and thus absorbs more of the suns flux (see “estimated”).

Supplementary Video Descriptions

Supplementary Video 1 | The solar-powered roller completes seven flips.

Supplementary Video 2 | Manual perturbation does not hinder roller’s ability to flip.

Supplementary Video 3 | Roller is kicked down a flight of stairs & continues to flip.

Supplementary Video 4 | Roller is dropped from 92 cm, bounces, and rolls away.

Appendix II: Supplementary Information, Chapter III

Text S1. Imaging

A Canon Rebel SL2 (100 mm f/2.8 Macro USM fixed lens, 1x magnification, 29.97 frames per second) was used to image photoreactions occurring in the UV/Vis quartz cuvette. The setup for these reactions is depicted in Supplementary Figure 1. Note that we define the positive *u*-direction to be against gravity (Supplementary Fig. 1). This is later relevant in Note S2.

Text S2. Particle Image Velocimetry

Video records of photoreactions inside the UV/vis cuvette were then segmented into individual grayscale frames based on the camera's frame rate (i.e., 29.97 FPS) using MATLAB code. These frames were then used to perform particle image velocimetry (PIV) using open-source code from Thielecke and Stamhuis.[1,2] Prior to analysis, the region of interest was specified as a rectangle inside of the wetted region of the cuvette where flows occur (Supplementary Fig. 4). Next, a fast-Fourier transform (FFT) window deformation algorithm was selected and four interrogation areas of decreasing window size (i.e., 64, 32, 16, and 8 pixels) were used to analyze the motion of particles (Supplementary Fig. 4), according to published protocols.[3]

The published protocols also recommend post-processing of data to remove erroneous vectors and ensure accurate calculation. This is achieved by surveying a scatterplot of the horizontal and vertical velocities, and removing calculated vectors

determined to be outliers. Graphically, this is achieved by selecting a boundary outside of which the data are outliers and will be removed (Supplementary Fig. 5). Visually, the incongruity of these erroneous vectors is confirmed by surveying plots of vector fields overlaid on each analyzed image.

The remaining velocity data were interpolated to provide values at all coordinate points. The data for each frame were then exported as text files containing four columns: the *u*-coordinate, *v*-coordinate, and associated *u*- and *v*-velocities of the fluid. These data were then analyzed using separate, custom-written MATLAB code that analyzes the positive *v*-velocities (i.e., opposing gravity) of each frame, and stores the highest value—i.e., the maximum velocity—at each point in time. These values of maximum velocity are then plotted against time to produce the curves in Supplementary Figs. 6 and 7.

Note S1. Dilute Solutions

Studies of the backward photoreaction of DASA 3.0 in toluene and chloroform are restricted to dilute solutions of DASA 3.0 due to the high extinction coefficient of DASA and the limitations of the apparatus detector.

Note S2. Bleaching front depends on container geometry

In general, the shape and location of the concentration gradient in the bleaching front depends in a complex way on the illumination profile in the container, the resulting bleaching reaction kinetics, and the convective mass transport of DASA 3.0, which is carried along by the flow produced as a result of the Rayleigh-Benárd convection. However, if all we seek is the location of the front and its motion in time, then the problem can be simplified by restricting the analysis solely to the bleaching front itself.

Consider that the bleached zone near the bleaching front is maintained at a relatively constant concentration $N_{A,open}$ of open DASA 3.0, and that the unbleached zone near the bleaching front is maintained at a relatively constant concentration $N_{B,open}$. For simplicity, we assume that the concentration varies from $N_{A,open}$ to $N_{B,open}$ over a distance, δ, that is much smaller than both the height of the bleaching front h_I and the fluid height *H*. Under this assumption, the bleaching front can be treated as a fictitious interface between “phases” A and B, at which a step change in N_{open} occurs due to the photoreaction across the thickness δ. If h_I is appreciably far

from the bottom of the container, then we can assume that in phase A the photoreaction has reached local equilibrium, such that no photoreaction occurs, resulting in quasi-steady state mass transport for the interface. The location of the interface therefore advances with a quasi-steady velocity $\boldsymbol{v}_I = dh_I/dt$, where h_I is the height of the interface.

The general boundary condition for mass transfer of chemical species *i* across an interface between a general fluid phase A and fluid phase B in vectorial form is given by a molar mass balance of species *i* at the interface, and can be written without loss of generality:[4]

$$\frac{dN_{I,i}}{dt} = \left\{ \left[\boldsymbol{j}_{A,i} + N_{A,i}(\boldsymbol{v}_A - \boldsymbol{v}_I) \right]_I - \left[\boldsymbol{j}_{B,i} + N_{B,i}(\boldsymbol{v}_B - \boldsymbol{v}_I) \right]_I \right\} \cdot \hat{\boldsymbol{n}}_I - r_{i,I} \qquad \text{(S1)}$$

where $N_{X,i}$ is the concentration of species *i* in phase X, $\boldsymbol{j}_{X,i}$ is the diffusive flux of species *i* in phase X, and $\boldsymbol{v}_X$ is the fluid velocity in phase X. $\hat{\boldsymbol{n}}_I$ is the outward pointing normal vector (defined here as pointing into phase B), and subscript *I* denotes that the quantity is evaluated at the interface. Here, $\boldsymbol{v}_I$ is the velocity of the location of the interface, which in general need not be equal to $\boldsymbol{v}_{A,I}$ or $\boldsymbol{v}_{B,I}$ because it represents the rate of change in location of the interface rather than a fluid velocity. The curly bracketed term represents the total net molar flux of species *i* to/from the interface (either from diffusion or convection), and $r_{i,I}$ is the net reaction rate (in units of $mol\ (volume \cdot time)^{-1}$) of species *i.*

We now make a number of other simplifying assumptions for our bleaching system. Because we already assumed that the interface remains quasi-steady, the left hand side of Eq. (S1) is identically zero. Momentum continuity across the fictitious interface requires that $\boldsymbol{v}_{A_I} = \boldsymbol{v}_{B_I} = \boldsymbol{v}_{\boldsymbol{fluid}}$. Furthermore, we assume DASA is dilute in solution, such that Fick's law can be used for $\boldsymbol{j}_{X,i}$. Finally, we will assume that the bleaching front is symmetric about the vertical centerline of the container, and restrict our analysis to the centerline, such that the problem reduces to a one-dimensional problem in the vertical (negative *v*) direction.

Under these assumptions and applying the interfacial balance to open DASA 3.0, Eq. (S1) simplifies to:

$$0 = \left(N_{A,open} - N_{B,open}\right)\left(\boldsymbol{v}_{fluid} - \boldsymbol{v}_I\right) + \left(\frac{\partial D_{open} N_{A,open}}{\partial z}\bigg|_I - \frac{\partial D_{open} N_{B,open}}{\partial z}\bigg|_I\right) + \delta r_{open,I} \quad \text{(S2)}$$

The first term in Eq. (S2) represents the net convection of DASA to the interface due to the convective flow. The second term represents the net diffusion of DASA to the interface due to concentration gradients in the bleached and unbleached regions. We expect that such gradients will be small, such that the diffusive flux is negligible compared to the convective flux and will be ignored in subsequent analysis. Making this assumption and solving for the interface velocity gives

$$\boldsymbol{v}_I = \boldsymbol{v}_{fluid} + \frac{\delta r_{I,open}}{\Delta N_{I,open}} \quad \text{(S3)}$$

where $\Delta N_{I,open} = N_{A,open} - N_{B,open}$ is the change in open DASA concentration across the interface. Note that Eq. (S3) assumes nothing about the rate of reaction (or, for that matter, the illumination), and so it will apply to any general reacting system that creates a quasi-steady reaction front of the sort that we have assumed here. To apply this prediction specifically to the DASA system, we use the expression for the net rate of photochemical reaction developed by Lui *et al.*,[5]

$$r_{I,open} = -\sigma\left(N_{I,open}\right)\phi_{OC}\left(N_{I,open}\right)I(h_I)N_{I,open} + k_{back}\left(N_{I,open}\right)\left[N_o - N_{I,open}\right] \quad \text{(S4)}$$

where σ is the absorption cross-section, ϕ_{OC} the quantum efficiency for photoconversion between the open and closed form, $I(h_I)$ the irradiation intensity at the bleaching front, k_{back} the rate constant for the backward photoconversion, and N_o the total concentration of DASA (including open and closed forms) in solution, which remains constant everywhere because the photoreaction is unimolecular. Eq. (S4) explicitly notes the functional dependence on N_{open} of the various photokinetic parameters (these will be suppressed in the equations to follow). Note that, because our analysis treats the bleaching front as a concentration discontinuity, the concentration of the interface $N_{I,open}$ at which the rate is evaluated remains undefined. However, since we have already assumed that no net photoreaction

occurs in the bleaching zone, a reasonable choice would be $N_{I,open} = N_{A,open} - c\Delta N_{I,open}$, where c is either 0 or 0.5.

Substituting Eq. (S4) into Eq. (S3) gives

$$\boldsymbol{v}_I = \boldsymbol{v}_{fluid} + \frac{\delta}{\Delta N_{I,open}}\left\{\sigma\phi_{OC} I(h_I) N_{I,open} - k_{back}\left[N_o - N_{I,open}\right]\right\} \quad \text{(S5)}$$

From this equation, it may appear at first glance that we have lost any time dependence of the problem. However, many of the parameters (chiefly $\boldsymbol{v}_{fluid}$ and $I(h_I)$) are implicitly time dependent, both because the bleaching front is advancing through a non-uniform velocity and irradiation field, and because these fields themselves are time-varying. Therefore, solving Eq. (S5) to obtain the entire time-dependence of the front velocity requires solving the full complex coupled mass, heat and flow transport problem, which is not presented in its entirety here.

Note S3. Nonzero starting fluid velocity

Nonzero fluid velocities seen at time t = 0 s in Fig. 5a are likely the result of our imaging set up. Though solutions containing DASA are allowed to settle for two minutes prior to irradiation, as soon as the cuvette is exposed to the white light, it takes several hundreds of milliseconds before the digital camera used in this experiment is able to adjust to the new brightness in its field of view. As such, the particle image velocimetry (PIV) analyses begin only as the camera has adjusted to

the light, at which time the photoreaction is already under way—resulting in a nonzero fluid velocity.

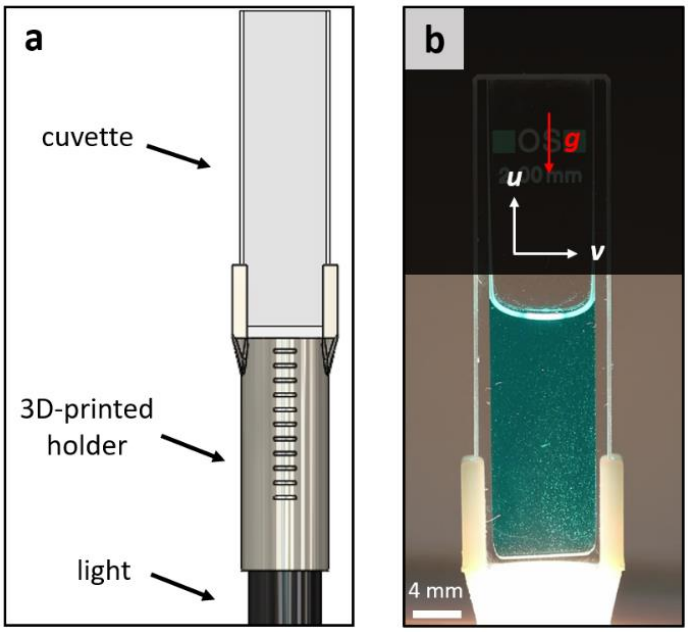

Supplementary Fig. S1 | Experimental setup used for UV-vis cuvette studies. a, Labeled SolidWorks rendering of setup. **b**, Image of setup with *u*- and *v*-coordinates labeled. As well as the gravity vector, *g*.

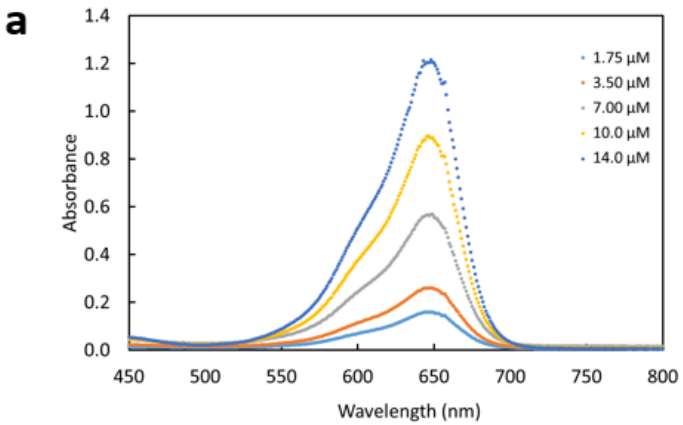

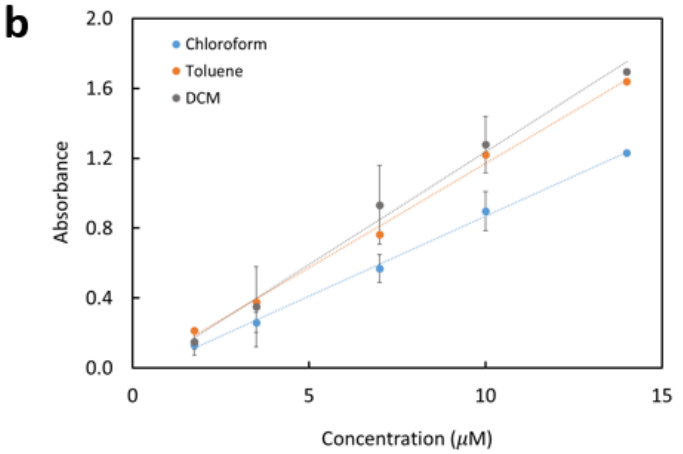

c

Solvent	ε (M^{-1} cm^{-1})
Toluene	118,820 ± 516
Chloroform	88,670 ± 300
DCM	129,190 ±490

Supplementary Fig. S2 | Molar Absorptivity of DASA in toluene, chloroform and dichloromethane. a, Representative absorption spectra obtained with UV-Vis spectrophotometry for various concentrations of DASA in chloroform. Maximum

absorption is plotted for each concentration in toluene, chloroform and dichloromethane **b,** from which the slope of the line is used to determine molar absorptivity according to Beer's law ($A = \varepsilon bc$, where ε is molar absorptivity, b is path length and c is concentration). **c,** Molar absorptivity values are reported for all solvents in the table.

a

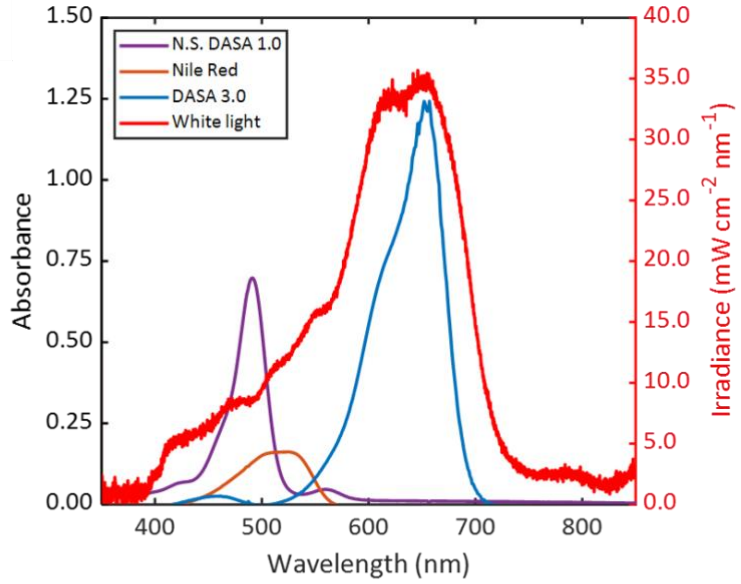

b

Dye (in Toluene)	ε (M^{-1} cm^{-1})
DASA 3.0	118,800 ± 520
Non-bleaching DASA	70,500 ± 350
Nile Red	38,000 ± 500

Supplementary Fig. S3 | Molar Absorptivity comparison of high-absorbing dyes and DASAs.

a, (Left axis) Representative absorption spectra obtained with UV-Vis spectrophotometry for 10 μM of DASA 3.0, non-switching DASA and Nile red in toluene. (Right axis) Absolute irradiance measurement of the white light source using a USB 4000-UV-Vis spectrometer (OceanOptics, Inc., USA). **b,** Molar absorptivities are determined at maximum absorption for each dye and reported for comparison.

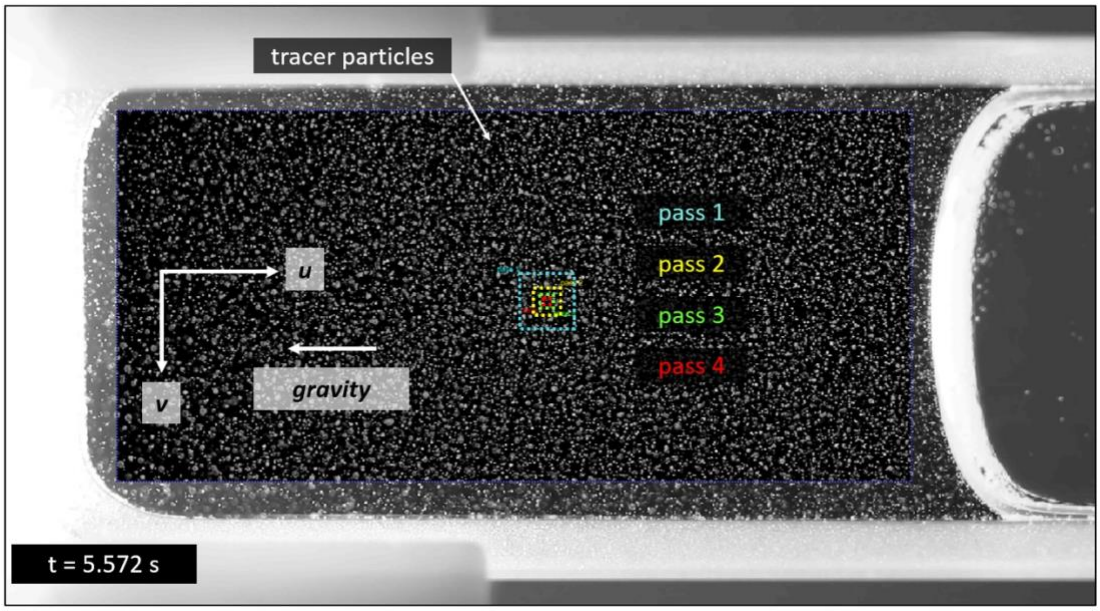

Supplementary Fig. S4 | Region of interest and window size selection, as executed in PIVLab. Speckles are tracer particles in space.

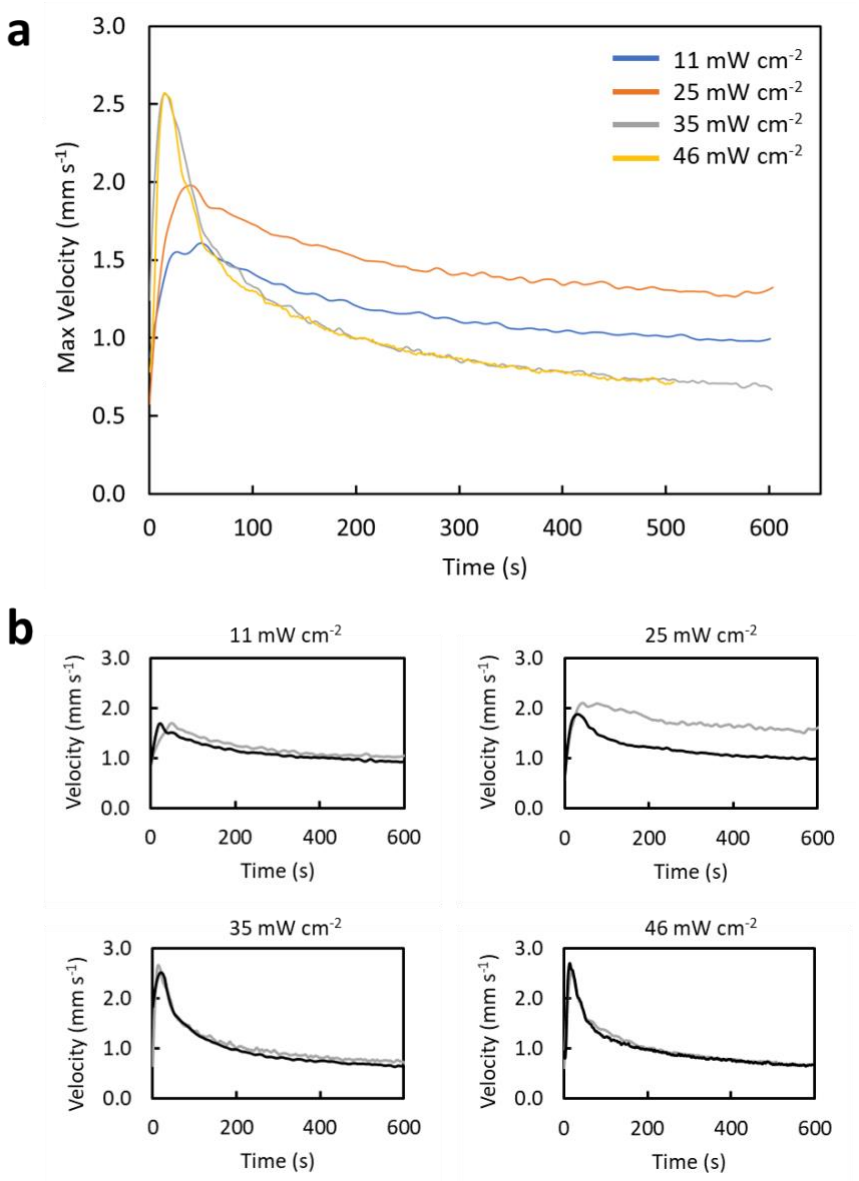

Supplementary Fig. S5 | Maximum velocity data for 0.25 mM DASA in chloroform irradiated at varying intensities. a, Average curves of differing intensity. **b**, Duplicate runs at each light intensity.

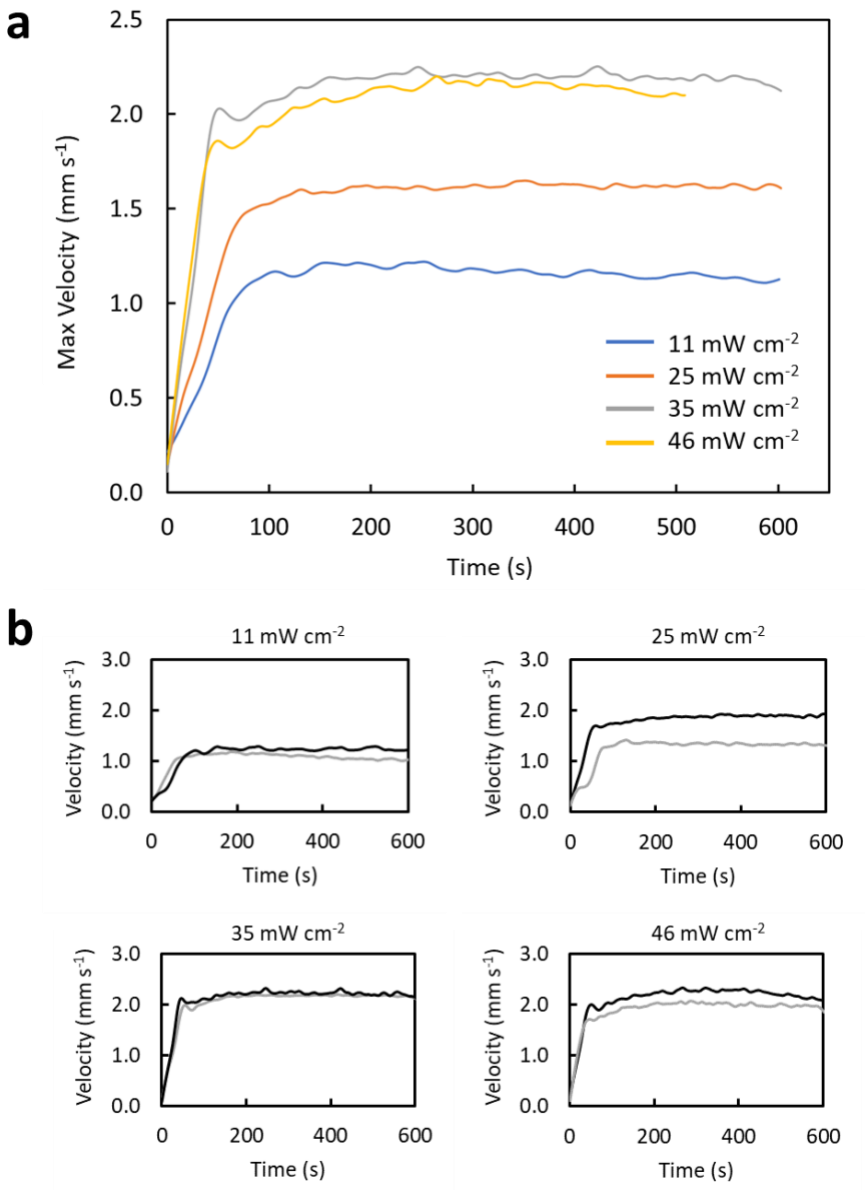

Supplementary Fig. S6 | Maximum velocity data for 0.25 mM DASA in toluene irradiated at varying intensities. a, Average curves of differing intensity. **b**, Duplicate runs at each light intensity.

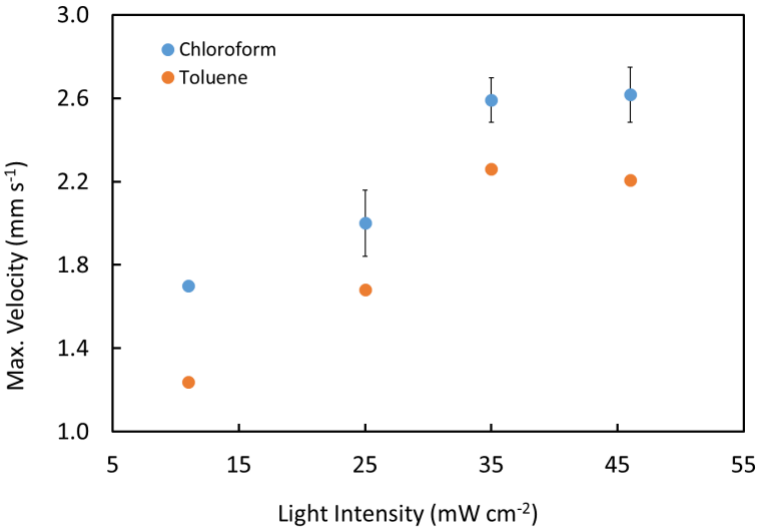

Supplementary Fig. S7 | Maximum velocity achieved vs. light intensity for DASA in chloroform and toluene. Erro bars: standard deviation, N=2. Note that in some cases the error bars are smaller than the marker size.

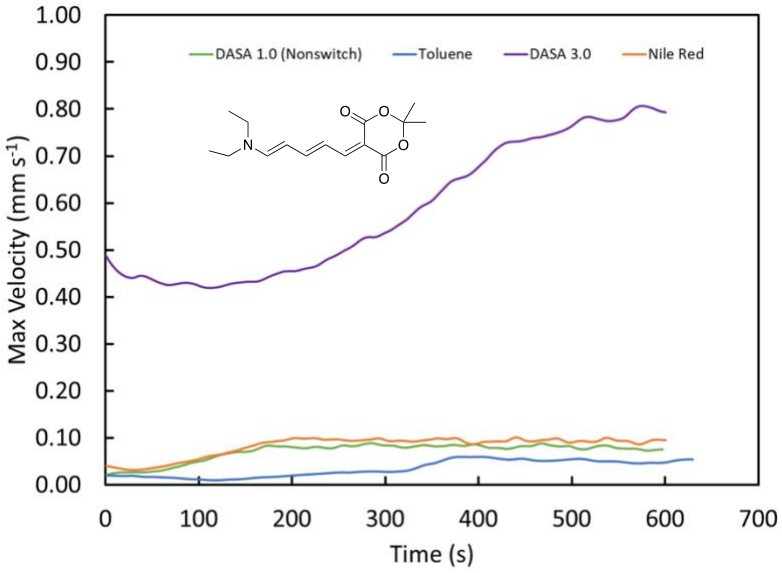

Supplementary Fig. S8 | DASA 3.0 and dye comparison. Velocity profiles for 0.25 mM DASA 3.0, Nile red and Non-switching DASA in toluene at 6.34 mW cm^{-2}. For the DASA 3.0-containing solutions, we measured a non-zero flow speed at the earliest times. This rapid increase, which sometimes appears to be instantaneous (as here), is observed in many of the measurements of fluids containing photochromic dyes (e.g., see Figures 5C, S5, and S6), and we suspect is due to the extremely rapid thermal response of the solution which quickly drives fluid motion. At this light intensity, it takes some time for the full convective rolling to establish, so we observe an increase in velocity as the full flow field develops. Future studies will enable measurement of the development and dynamics of the full flow field; these details are not fully captured in the maximum velocity reported here. At all times, the magnitude of flow velocity measured using DASA 3.0 is significantly larger than those observed for non-switching dyes or solvent only, as expected.

a

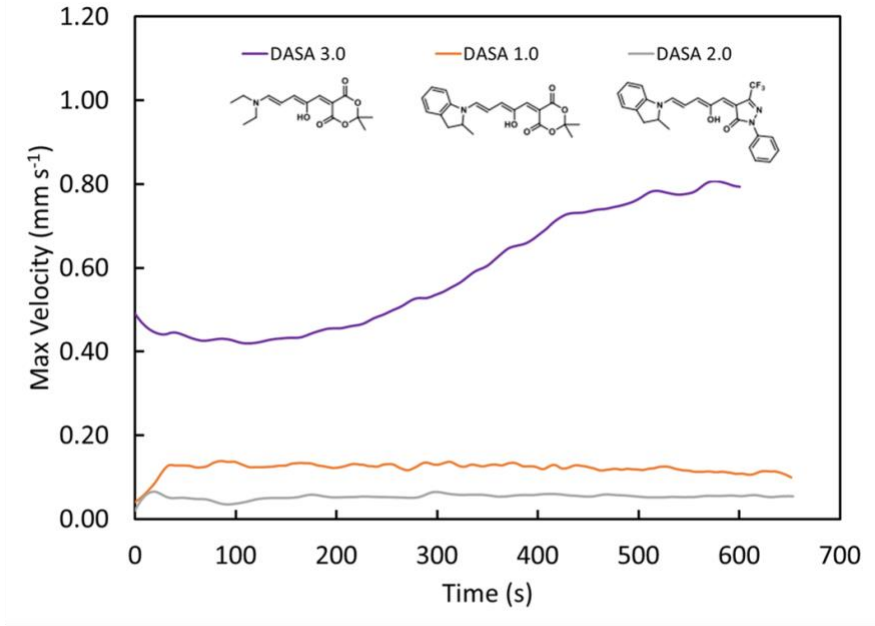

b

DASA	ε (M^{-1} cm^{-1})	% open	Half life $t_{1/2}$	Abs. max
DASA 3.0	118,200	>95%	40s	655 nm
DASA 2.0	107,000	31%	3240s	580 nm
DASA 1.0	102,000	>95%	100s	545 nm

Supplementary Fig. S9 | DASA 1.0, 2.0 and 3.0 comparison. a, Velocity profiles of 0.25mM of each generation DASA in toluene at 6.34 mW cm^{-2} light intensity. **b**, Representative details regarding molar absorptivity, thermal equilibria, and half-life ($1/k_b$) of each DASA in toluene.[6] We attribute the smaller flow velocities developed by DASA 1.0 as compared to DASA 3.0 to the smaller molar absorptivity, as well as the lower wavelength absorption maximum, which is off-peak for the white light source used here (see Figure S3). In the case of DASA 2.0, the equilibrium value and rate of photo conversion from the colored form to colorless form is significantly different: only 31% open for DASA 2.0 as compared to >95% for DASA 1.0 and 3.0,

which undermines its ability to serve as a photothermal agent to drive high speed flows.

Supplementary Video Descriptions

Supplementary Video 5 | Bleaching front of 0.25 mM DASA in chloroform. Cuvette was irradiated using 41.7 mW cm^{-2} of white light shone through a bandpass filter ($\lambda = 650 \pm 40$ nm).

Supplementary Video 6 | Convection of 0.25 mM DASA in toluene (video speed, 10x). Left panel depicts the video recording of the convection. Right panel depicts a heat map video of the same video, generated via particle image velocimetry analysis (Canon EOS Rebel T5i, 100mm f/2.8 macro lens, magnification 1x).

Supplementary Video 7 | Localized fluid motion in 0.25 mM DASA in chloroform.

Appendix III: Supplementary Information, Chapter IV

1. Experimental Details

A. Materials.

All chemicals were used as received unless otherwise noted. Aluminum oxide activated (basic, Brockmann I), methyl acrylate (MA, 99%, contains ≤100 ppm monomethyl ether hydroquinone as inhibitor), tetra(ethylene glycol) diacrylate (TEGDA, technical grade, contains 150-200 ppm MEHQ as inhibitor, 100-150 ppm HQ as inhibitor), 3,4-epoxycyclohexylmethyl 3,4-epoxycyclohexanecarboxylate (ECC), acryloyl chloride (≥97%, contains ~400 ppm phenothiazine as stabilizer), 2-methylthianaphthene (97%), and triethylamine (TEA, ≥99.5%) were purchased from Sigma Aldrich. Inhibitors were removed from MA and TEGDA by a plug of basic alumina. L-camphorquinone (CQ, 99%), benzothiophene (97%), and n-butyllithium (2.3 M solution in cyclohexane) were purchased from ACROS organics™. (3-ethyloxetan-3-yl)methanol (OXA. 98%) was purchased from Arc Pharm Inc. and used as received. Ethyl 4-(dimethylamino)benzoate (EDMAB, 99%) was purchased from Alfa Aesar. [4-[Octyloxy]phenyl]phenyliodonium hexafluoroantimonate (HNu_{254}), 2-(butyryloxy)-N,N,N-trimethylethan-1-aminium butyltriphenylborate (Borate), and 6-hydroxy-2,4,5,7-tetraiodo-3H-xanthen-3-one (HNu_{535}) were purchased from Spectra group limited. Octafluorocyclopentene (>98%) was purchased from TCI. XHT-500 fluorinated oil was purchased from Grainger.

All printed materials were produced by exposure to light produced by an Epson 5040UB 3 LCD projector focused through a Zeiss Bronica Zenzanon-S lens (105 mm, f/3.5).

B. Instrumentation.

Displacement-controlled uniaxial tensile testing was performed on a vertical TwinRail positioning table (Lintech, CA) with a Lebow Load Cell (Model 3108–10, 10-lb capacity, Eaton Corp., MI) fitted with a machined sample holder.

Optical microscopy was performed on a Keyence VHX-5000 Microscope at 10x-20x magnification.

A Canon Rebel SL2 (100 mm, f/2.8 Macro USM fixed lens, 1x magnification, 30 frames per second) was used to image the deformation of each sample during mechanical testing (see supplementary videos).

C. Synthesis.

Synthesis of (3-ethyloxetan-3-yl)methyl acrylate (OXA-A)

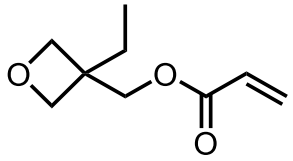

The synthesis of OXA-A was conducted according to previously reported protocols.[129]

Synthesis of 1,2-bis(3-methyl-1-benzothiophen-2-yl)perfluorocyclopentene (DAE_{470})
open and closed isomers

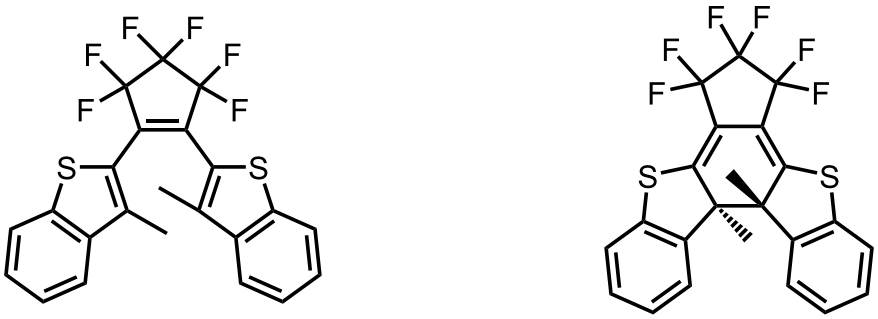

The synthesis of both the open (left) and closed (right) isomers of DAE470 were conducted according to previously reported protocols.[129]

Synthesis of 1,2-bis(2-methyl-1-benzothiophen-3-yl)perfluorocyclopentene (DAE_{530})
open and closed isomers

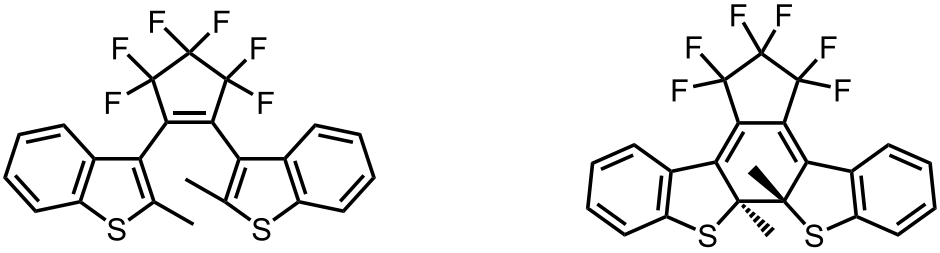

The synthesis of both the open (left) and closed (right) isomers of DAE_{470} were conducted according to previously reported protocols.[129], [130]

D. Resin formulation.

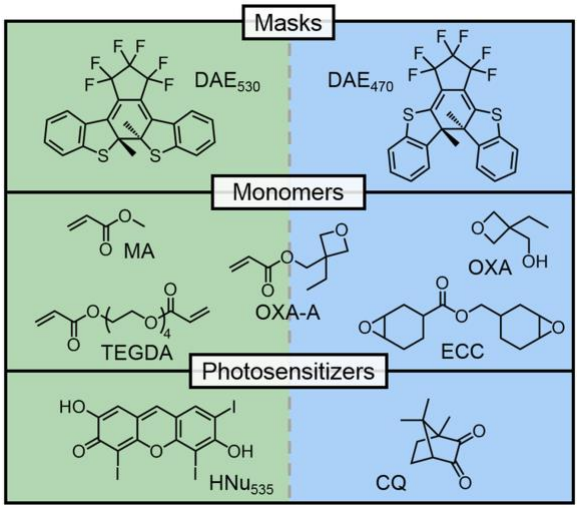

Figure S1. Chemical structures of select components in SMaLL resins used in this work**.**

Table S1. Weight percentages and function of chemical species in SMaLL resins used in this work

Species	Function	Loading (wt%)	
MA	Radical monomer	50	**Majority components**
OXA-A	Network compatibilizer	5	
OXA	Cationic initiator / monomer	10	
ECC	Cationic crosslinker	35	
TEGDA	Radical crosslinker	0.5	**wt% relative to majority components**
Borate	Radical accelerator	0.05	
EDMAB	Cationic accelerator	0.2	
HNu_{535}	Photosensitizer	0.01	
CQ	Photosensitizer	0.2	
HNu_{254}	Coinitiator	0.45	
DAE_{530}	Solution mask	8 mM	**mM instead of wt%**
DAE_{470}	Solution mask	10 mM	

E. Sample Preparation.

The printing of the reported samples follows previous literature conditions[129], summarized here. A surface treated (perfluoroalkyl) glass build plate was adhered to the bottom of a custom build chamber using a fluorinated oil (XHT-500). The septa-sealed chamber was then purged with argon and ~3 mL of degassed resin was transferred into the chamber. The build chamber was placed in custom brackets over a projector (Epson 5040UB 3 LCD) equipped with a photography lens (Zeiss Bronica Zenzanon-S lens, 105 mm, f/3.5). The resin was then exposed to digital images. Blue segments of the images were exposed for 6.5 minutes (if applicable) followed by exposure all non-black regions (i.e., pores) in green for 2 minutes to ensure strong connectivity between segments. After exposure, residual resin was retrieved via syringe and recycled for future prints.

The printed part was then removed from the build plate with a razor blade and introduced into a dialysis chamber to remove any unreacted monomers from the sample. Dialysis was carried out with mixtures of acetone:isopropanol (vol:vol 3:1, 1:1, 1:3) prior to drying overnight in air followed by storage in a vacuum chamber. Dried samples were adhered to laser-cut fiberglass tabs using a generic cyanoacrylate-based adhesive. This method was used to avoid applying unwanted stresses to the samples orthogonal to the loading axis.

2. Sample Design.

A. Notch-free sample templates.

All templates for solution mask liquid lithography (SMaLL) printing were designed in Microsoft PowerPoint and then projected onto resin baths using the above methods. Fig. S2 illustrates sample templates used for printing square-packed, hexagonally-packed, and pore-free samples and the resulting specimens. To simplify the comparison between samples, the area fraction of pores was held constant (51 ± 3%), as was the center-to-center distance between pores as measured along the horizontal and vertical axes of the structure. The hexagonal packing was achieved by simply shifting the pore position of every other horizontal row (defined along the long axes of the structure) by ½ of the center-to-center distance between pores and adding one additional pore to maintain left-right symmetry. This results in non-equal-sided hexagons that are slightly elongated along the vertical direction. A red outline of these shapes is illustrated in Fig. S2a.

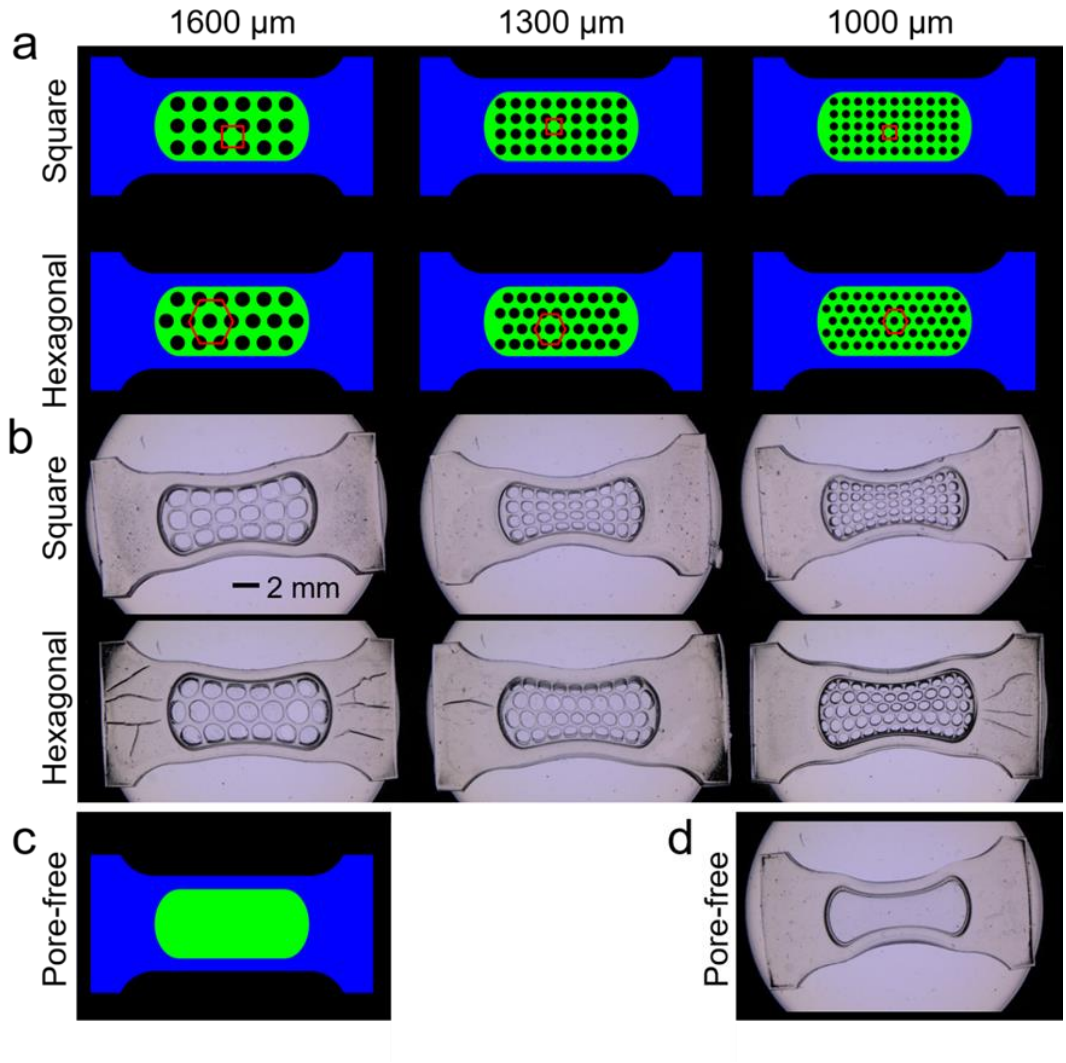

Fig. S2. a) SMaLL printing templates used for hex- and square-packed samples for all pore sizes. b) Optical microscope images of printed pore-containing specimens after dialysis and drying. c) SMaLL printing templates used for pore-free samples. d) Optical microscope image of a pore-free specimen after dialysis and drying.

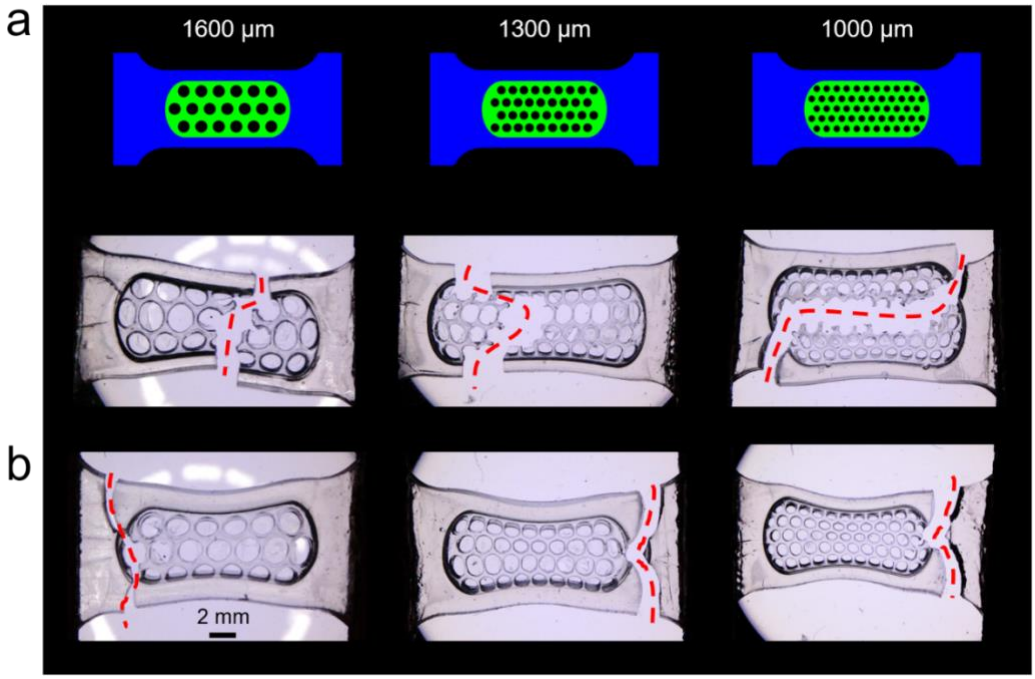

Fig. S3. a) Examples of crack paths (demarcated here forth by red dashed lines) for notch-free hexagonally-packed samples demonstrating increasing crack tortuosity as a function of reducing pore size, however these failures can largely be attributed to well-positioned stochastic failure in the stiff blue exterior. b) Examples of poor crack deflection in notch-free hexagonally-packed samples, demonstrating the need for repeatable crack initiation points (notched, below).

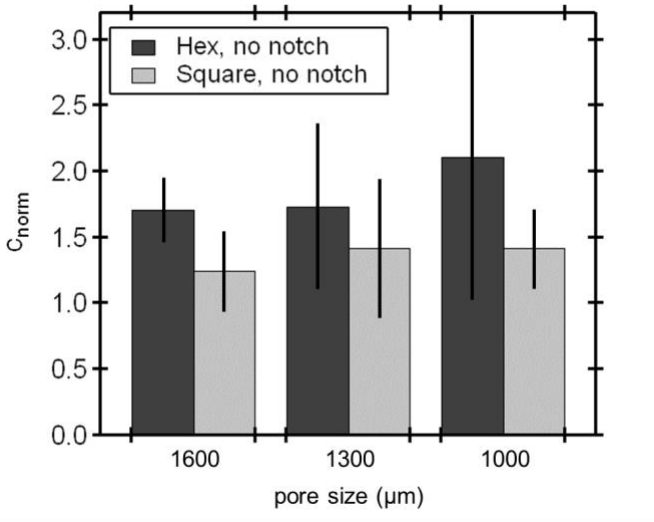

Fig. S4. Impact of pore size and packing of voids on crack tortuosity in hexagonally- and square-packed samples without notches. Without controlling the location of crack initiation (via notches), the crack lengths measured vary widely for all sample geometries, highlighting the importance of samples with notches.

B. Notched sample templates.

All templates for solution mask liquid lithography (SMaLL) printing were designed in Microsoft PowerPoint and then projected onto resin baths using the above methods. Fig. S5a illustrates sample templates used for notched square-packed and hexagonally-packed samples.

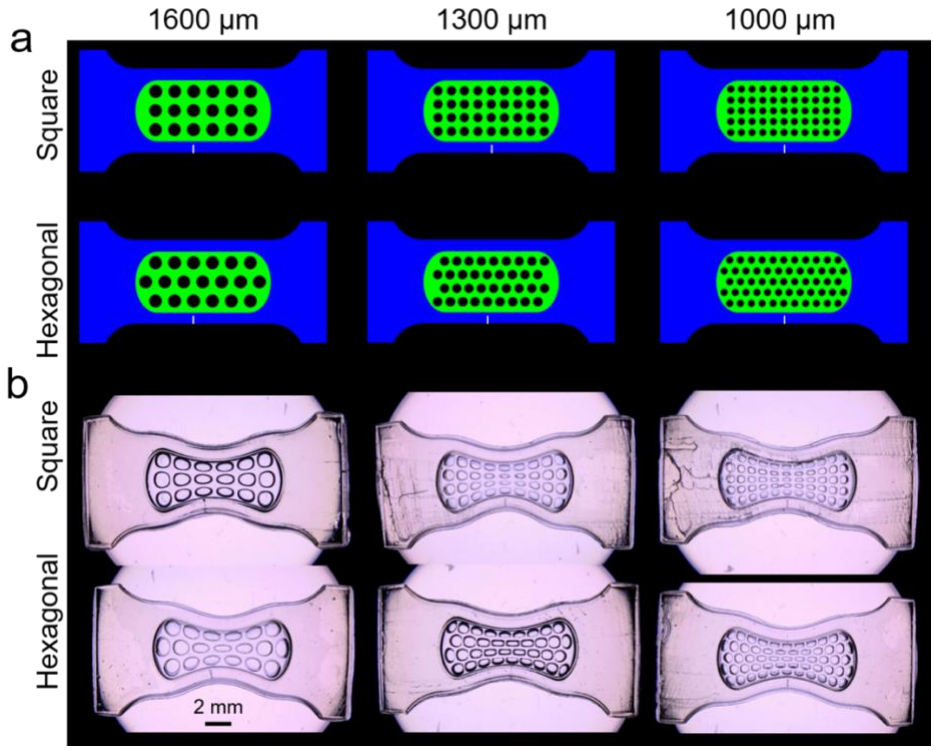

Fig. S5. a) SMaLL printing templates and b) resulting samples used for the notched square- and hex- packed cases.

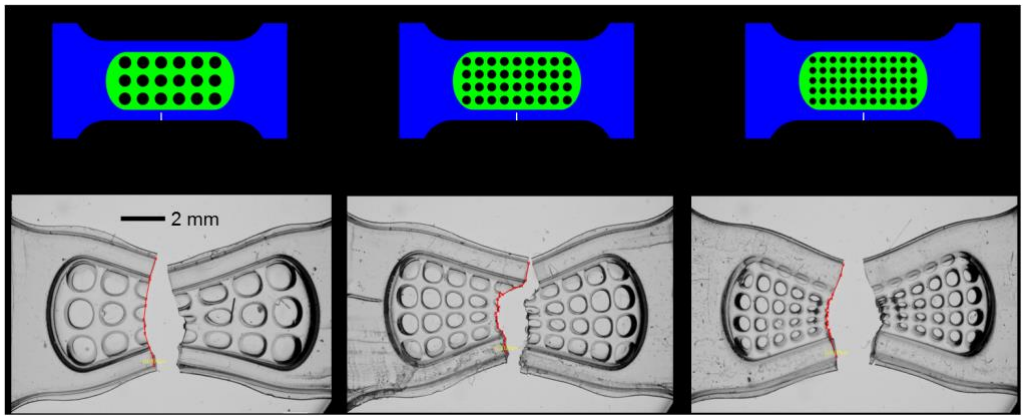

Fig S6. Representative failures of notched samples with square-packed pores (outline crack path with red line).

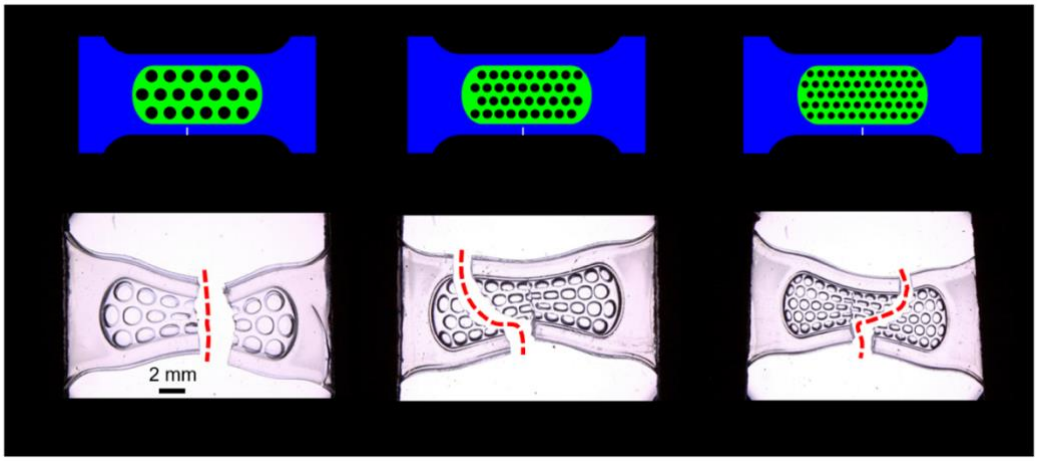

Fig S7. Representative failures of notched samples with hexagonally-packed pores (outline crack path with dashed red line).

3. Characterization.

A. Mechanical testing and imaging.

Using the aforementioned tensile testing apparatus, all samples were tested at a fixed strain rate of 100% min^{-1}. Forces and displacements recorded during tensile testing were then converted to stresses and strains using cross-sectional area and length measurements performed using the Keyence VHX-5000's built-in software. Post mechanical testing, Keyence's built-in software was used to calculate crack length.

A Canon Rebel SL2 was used to image the deformation of each sample during mechanical testing (see supplementary videos). Fig. S8b offers a screenshot from a recording of mechanical testing.

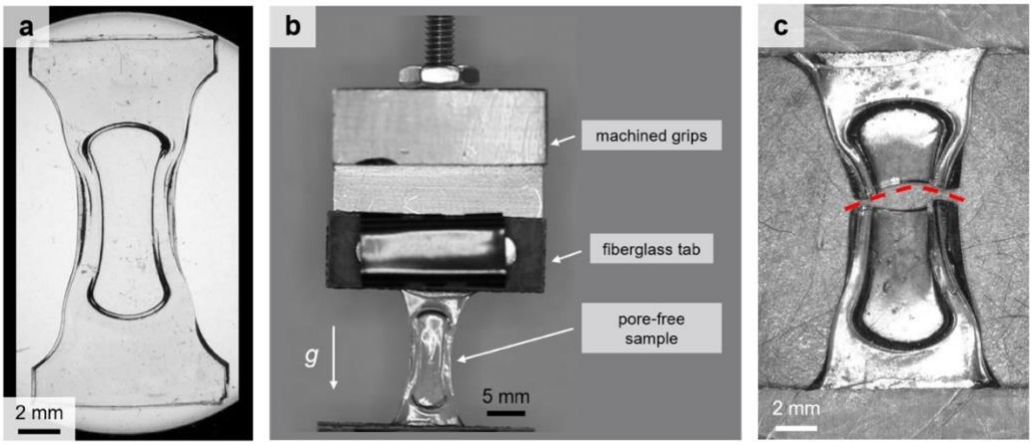

Fig. S8. Imaging before, during, and after mechanical testing. a) A pore-free composite imaged on the Keyence VHX-5000. b) A screenshot from a video

recording of a tensile test, illustrating the different components of the tensile testing setup. c) An image of the fractured composite obtained using the Keyence VHX-5000.

B. Mechanical properties of notched samples.

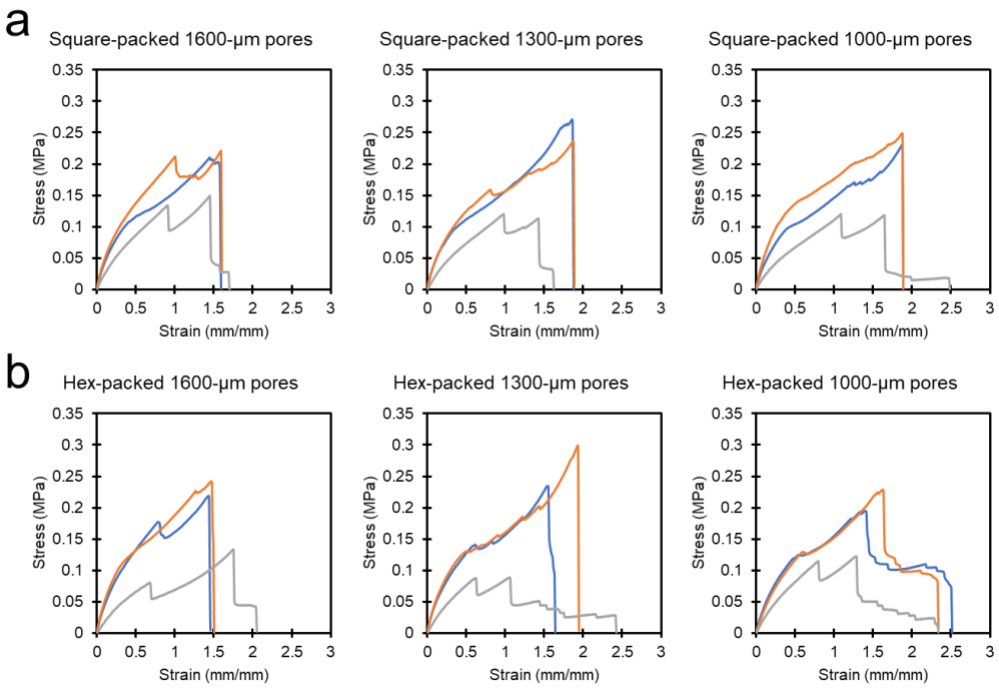

Fig. S9. a) Stress-strain curves for square-packed samples, demonstrating limited increases in ultimate strain as a function of reduced pore size due to near-linear crack paths. b) Stress-strain curves for hexagonally-packed samples, showing large increases in ultimate strain with similar tensile response.

4. Simulations.

A. Material fits.

The stress-strain response of constituent radical (green) and dual-cured radical/cationic (blue) materials were fitted to hyper-elastic models. The dual-cured material follows a Yeoh model (Fig. S10) while the radical material follows the Mooney-Rivlin model (Fig. S11). Both materials were assumed to be incompressible. The strain energy density in the Yeoh model is defined as $W = c_1(I_1 - 3) + c_2(I_1 - 3)^2 + \mathrm{c}_3(I_1 - 3)^3$ where I_1 is the first invariant of the Cauchy-Green deformation tensor and c_n is the n^{th} constant. Using a fit to experimental results from a simple tensile test, it was found that $c_1 = 0.136\ MPa$, $c_2 = -3.2\ KPa$, and $c_3 = 2.7\ KPa$. The strain energy density in the Mooney-Rivlin model is defined as $W = c_1(I_1 - 3) + c_2(I_2 - 3)$, where I_2 is the second invariant Cauchy-Green deformation tensor and c_n is the n^{th} constant. Here, a fit to the stress-strain data obtained by tensile test of dog bone samples of uniform radical (green) material reveals that $c_1 = 0.01\ \mathrm{MPa}$ and $c_2 = 0.083\ \mathrm{MPa}$.

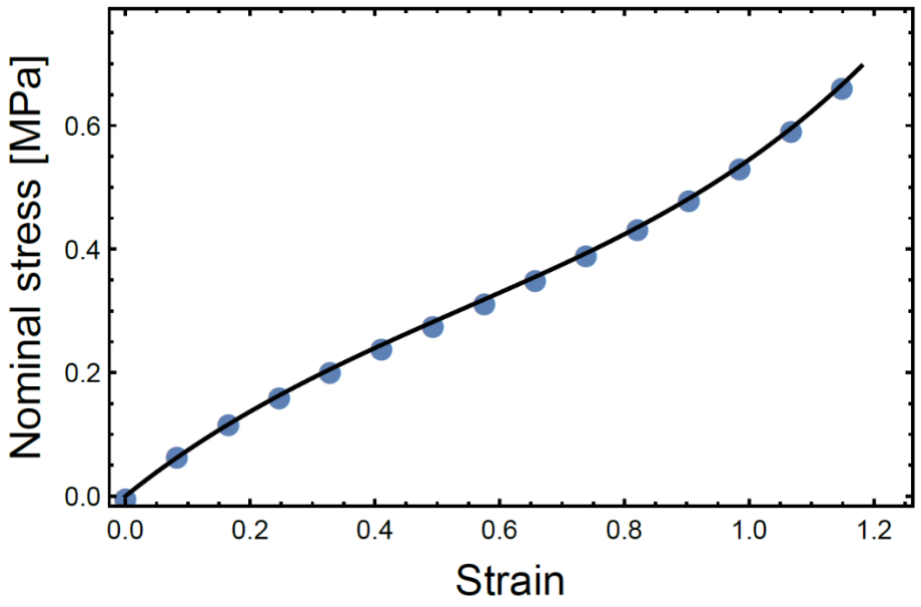

Fig. S10. Fit to the stress-strain data obtained for a uniform dual-cured radical/cationic material (obtained by curing with blue light only) subjected to uniaxial stretch, using a Yeoh hyper-elastic material model.

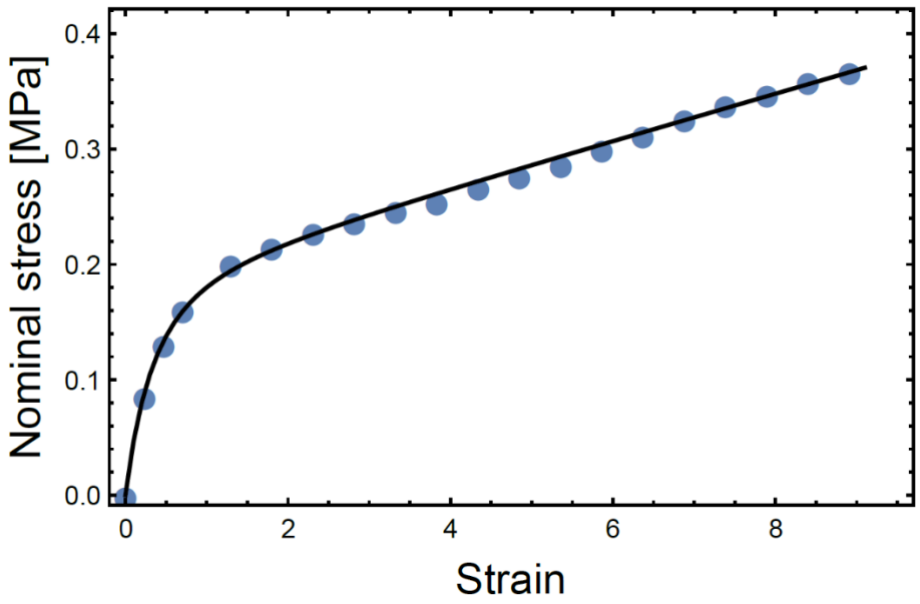

Fig. S11. Fit to the stress-strain data obtained for a uniform radical cured constituent material (obtained by curing with green light only) subjected to uniaxial stretch, using a Mooney Rivlin hyper-elastic material model.

B. Finite Element Analysis.

A two-dimensional analysis of the square- and hexagonally-packed porous samples was performed in COMSOL under plane-stress conditions. The samples were subjected to uniaxial strains of 100%. The results below are the maximum tensile principal stresses obtained for samples with hexagonally-packed 1600-µm (Fig. S12) and 1000-µm (Fig. S13) pores, as well as simulated samples with square-packed 1600-µm (Fig. S14) and 1000-µm (Fig. S15) pores.

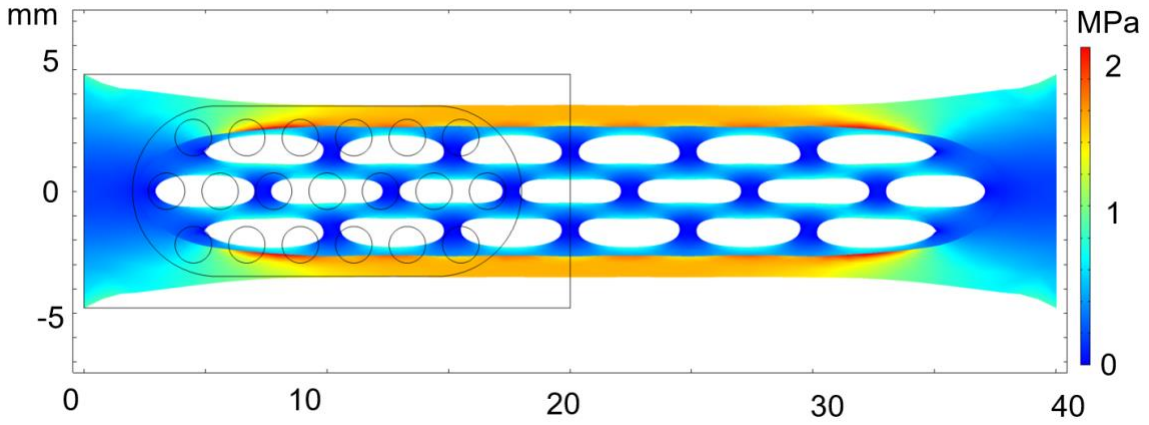

Fig S12. Maximum principal stresses of simulated sample with hexagonally-packed, 1600-µm pores, here shown at 100% strain. The thin black outline depicts the sample at 0% strain.

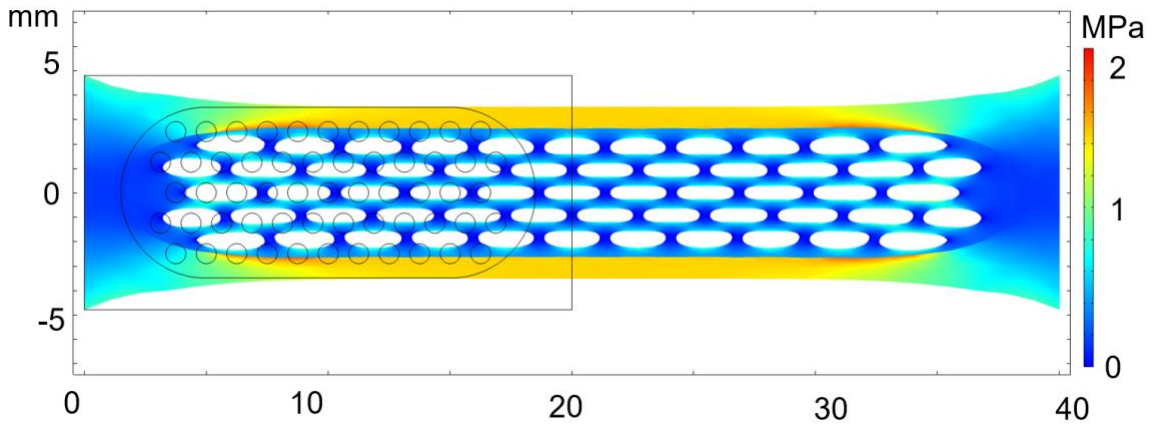

Fig S13. Maximum principal stresses of simulated sample with hexagonally-packed, 1000-µm pores at 100% strain. The thin black outline depicts the sample at 0% strain.

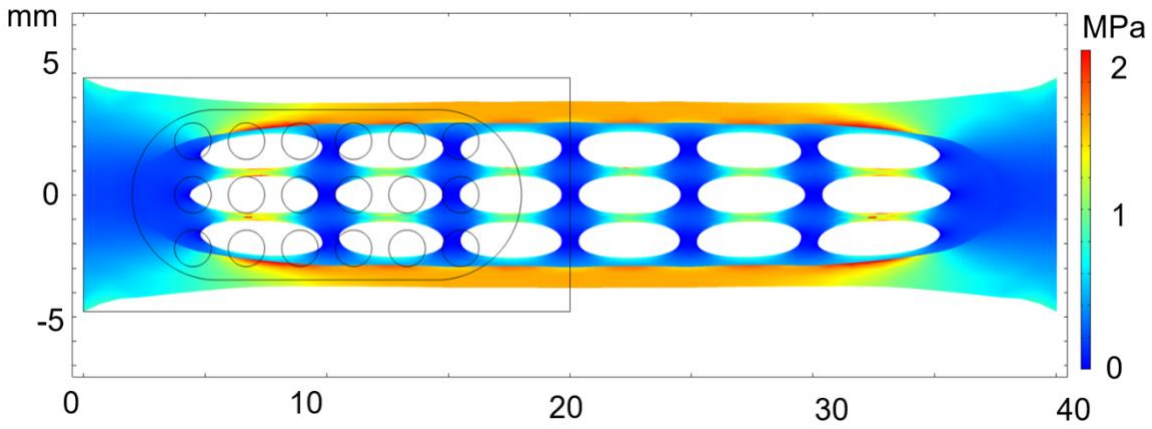

Fig S14. Maximum principal stresses of a simulated sample with square-packed, 1600-µm pores, at 100% strain. The thin black outline depicts the sample at 0% strain.

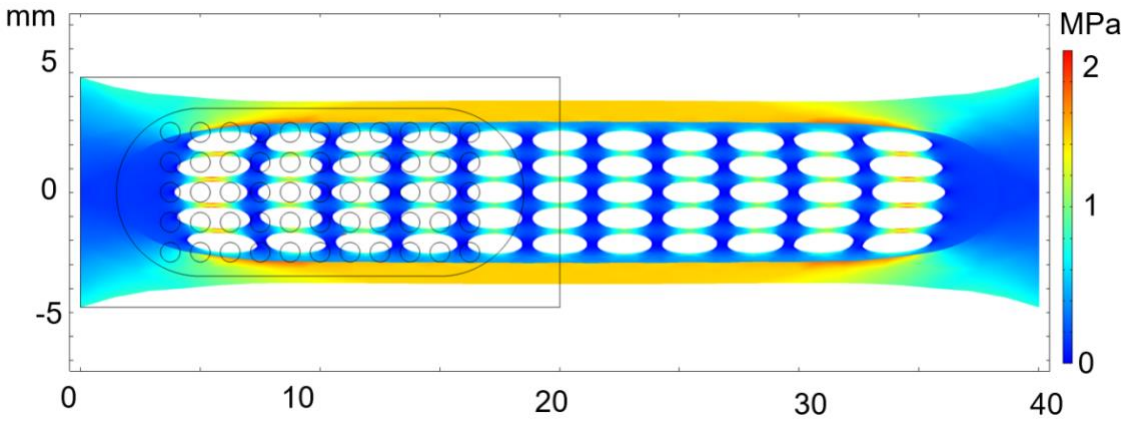

Fig S15. Maximum principal stresses of a simulated sample with square-packed, 1000-µm pores at 100% strain. The thin black outline depicts the sample at 0% strain.

5. Supplementary Video Descriptions

Supplementary Video S8 | Fracture of a pore-free sample.

Supplementary Video S9 | Fracture of an un-notched hexagonally-packed, small pore (mean pore diameter = 1000 μm) sample.

Supplementary Video S10 | Fracture of a notched hexagonally-packed, small pore (mean pore diameter = 1000 μm) sample.

Supplementary Video S11 | Fracture of a notched square-packed, small pore (mean pore diameter = 1000 μm) sample.

Supplementary Video S12 | Fracture of an un-notched square-packed, small pore (mean pore diameter = 1000 μm) sample.

References

[1] S. Kim, C. Laschi, and B. Trimmer, “Soft robotics: A bioinspired evolution in robotics,” *Trends in Biotechnology*, vol. 31, no. 5. pp. 287–294, May 2013. doi: 10.1016/j.tibtech.2013.03.002.

[2] B. Trimmer, “A Journal of Soft Robotics: Why Now?,” *Soft Robot*, vol. 1, no. 1, pp. 1–4, 2014, doi: 10.1089/soro.2013.0003.

[3] M. Wehner *et al.*, “Pneumatic Energy Sources for Autonomous and Wearable Soft Robotics,” *Soft Robot*, vol. 1, no. 4, pp. 263–274, Dec. 2014, doi: 10.1089/soro.2014.0018.

[4] V. Sanchez *et al.*, “Smart Thermally Actuating Textiles,” *Adv Mater Technol*, vol. 5, no. 8, Aug. 2020, doi: 10.1002/admt.202000383.

[5] M. Cianchetti, C. Laschi, A. Menciassi, and P. Dario, “Biomedical applications of soft robotics,” *Nature Reviews Materials*, vol. 3, no. 6. Nature Publishing Group, pp. 143–153, Jun. 01, 2018. doi: 10.1038/s41578-018-0022-y.

[6] J. B. Guang-Zhong Yang, Pierre E. Dupont, Peer Fischer, Luciano Floridi, N. J. Robert Full, Vijay Kumar, Marcia McNutt, Robert Merrifield, B. S. Bradley J. Nelson, Mariarosaria Taddeo, Russell Taylor, and Z. L. W. Manuela Veloso, Robert Wood, “The grand challenges of Science Robotics,” *Sci Robot*, 2018.

[7] F. Meder, G. A. Naselli, A. Sadeghi, and B. Mazzolai, “Remotely Light-Powered Soft Fluidic Actuators Based on Plasmonic-Driven Phase Transitions in Elastic Constraint,” *Advanced Materials*, vol. 31, no. 51, 2019, doi: 10.1002/adma.201905671.

[8] T. Hiraki *et al.*, “Laser Pouch Motors: Selective and Wireless Activation of Soft Actuators by Laser-Powered Liquid-to-Gas Phase Change,” *IEEE Robot Autom Lett*, vol. 5, no. 3, pp. 4180–4187, 2020, doi: 10.1109/LRA.2020.2982864.

[9] J. Han *et al.*, “Untethered Soft Actuators by Liquid–Vapor Phase Transition: Remote and Programmable Actuation,” *Advanced Intelligent Systems*, vol. 1, no. 8, p. 1900109, 2019, doi: 10.1002/aisy.201900109.

[10] S. M. Mirvakili, A. Leroy, D. Sim, and E. N. Wang, “Solar-Driven Soft Robots,” *Advanced Science*, vol. 2004235, pp. 1–7, 2021, doi: 10.1002/advs.202004235.

[11] Y. Zhao, Y. Chi, Y. Hong, Y. Li, S. Yang, and J. Yin, “Twisting for soft intelligent autonomous robot in unstructured environments,” 2022, doi: 10.1073/pnas.

[12] M. M. Russew and S. Hecht, “Photoswitches: From molecules to materials,” *Advanced Materials*, vol. 22, no. 31, pp. 3348–3360, Aug. 2010, doi: 10.1002/adma.200904102.

[13] S. Helmy, F. A. Leibfarth, S. Oh, J. E. Poelma, C. J. Hawker, and J. R. de Alaniz, “Photoswitching using visible light: A new class of organic photochromic molecules,” *J Am Chem Soc*, vol. 136, no. 23, pp. 8169–8172, Jun. 2014, doi: 10.1021/ja503016b.

[14] M. M. Russew and S. Hecht, “Photoswitches: From molecules to materials,” *Advanced Materials*, vol. 22, no. 31, pp. 3348–3360, Aug. 2010, doi: 10.1002/adma.200904102.

[15] S. Helmy, F. A. Leibfarth, S. Oh, J. E. Poelma, C. J. Hawker, and J. R. de Alaniz, “Photoswitching using visible light: A new class of organic photochromic molecules,” *J Am Chem Soc*, vol. 136, no. 23, pp. 8169–8172, Jun. 2014, doi: 10.1021/ja503016b.

[16] N. D. Dolinski *et al.*, “Solution Mask Liquid Lithography (SMaLL) for One-Step, Multimaterial 3D Printing,” *Advanced Materials*, vol. 30, no. 31, pp. 1–6, 2018, doi: 10.1002/adma.201800364.

[17] N. D. Dolinski *et al.*, “Tough Multimaterial Interfaces through Wavelength-Selective 3D Printing,” *ACS Appl Mater Interfaces*, vol. 13, no. 18, pp. 22065–22072, May 2021, doi: 10.1021/acsami.1c06062.

[18] H. Gao, B. Ji, I. L. Ja, E. Arzt, and P. Fratzl, “Materials become insensitive to flaws at nanoscale :,” *Proc Natl Acad Sci U S A*, vol. 100, no. 10, pp. 5597–5600, 2003.

[19] F. Barthelat and R. Rabiei, “Toughness amplification in natural composites,” *J Mech Phys Solids*, vol. 59, no. 4, pp. 829–840, 2011, doi: 10.1016/j.jmps.2011.01.001.

[20] V. Sanchez *et al.*, “Smart Thermally Actuating Textiles,” *Adv Mater Technol*, vol. 5, no. 8, pp. 1–10, 2020, doi: 10.1002/admt.202000383.

[21] M. Wehner *et al.*, “Pneumatic Energy Sources for Autonomous and Wearable Soft Robotics,” *Soft Robot*, vol. 1, no. 4, pp. 263–274, 2014, doi: 10.1089/soro.2014.0018.

[22] H. Y. Chen *et al.*, “RUBIC: An Untethered Soft Robot With Discrete Path Following,” *Front Robot AI*, vol. 6, no. July, 2019, doi: 10.3389/frobt.2019.00052.

[23] M. T. Tolley *et al.*, “A Resilient, Untethered Soft Robot,” *Soft Robot*, vol. 1, no. 3, pp. 213–223, 2014, doi: 10.1089/soro.2014.0008.

[24] M. Wehner *et al.*, “An integrated design and fabrication strategy for entirely soft, autonomous robots,” *Nature*, vol. 536, no. 7617, pp. 451–455, 2016, doi: 10.1038/nature19100.

[25] L. Chen *et al.*, “The energy flow and mechanical modeling of soft chemo-mechanical machines,” *J Appl Phys*, vol. 124, no. 16, 2018, doi: 10.1063/1.5050415.

[26] C. D. Onal, X. Chen, G. M. Whitesides, and D. Rus, “Soft mobile robots with on-board chemical pressure generation,” *Springer Tracts in Advanced Robotics*, vol. 100, pp. 525–540, 2017, doi: 10.1007/978-3-319-29363-9_30.

[27] R. F. Shepherd *et al.*, “Using explosions to power a soft robot,” *Angewandte Chemie - International Edition*, vol. 52, no. 10, pp. 2892–2896, 2013, doi: 10.1002/anie.201209540.

[28] M. T. Tolley *et al.*, “An untethered jumping soft robot,” *IEEE International Conference on Intelligent Robots and Systems*, no. Iros, pp. 561–566, 2014, doi: 10.1109/IROS.2014.6942615.

[29] M. Loepfe, C. M. Schumacher, U. B. Lustenberger, and W. J. Stark, “An untethered, jumping roly-poly soft robot driven by combustion,” *Soft Robot*, vol. 2, no. 1, pp. 33–41, 2015, doi: 10.1089/soro.2014.0021.

[30] M. Boyvat, D. M. Vogt, and R. J. Wood, “Ultrastrong and High-Stroke Wireless Soft Actuators through Liquid–Gas Phase Change,” *Adv Mater Technol*, vol. 4, no. 2, pp. 1–6, 2019, doi: 10.1002/admt.201800381.

[31] A. Miriyev, K. Stack, and H. Lipson, “Soft material for soft actuators,” *Nat Commun*, vol. 8, no. 1, pp. 1–8, 2017, doi: 10.1038/s41467-017-00685-3.

[32] S. M. Mirvakili, D. Sim, I. W. Hunter, and R. Langer, “Actuation of untethered pneumatic artificial muscles and soft robots using magnetically induced liquid-to-gas phase transitions,” *Sci Robot*, vol. 5, no. 41, pp. 1–10, 2020, doi: 10.1126/SCIROBOTICS.AAZ4239.

[33] J. Li, M. Sun, and Z. Wu, “Design and Fabrication of a Low-Cost Silicone and Water-Based Soft Actuator with a High Load-to-Weight Ratio,” *Soft Robot*, vol. 00, no. 00, pp. 1–14, 2020, doi: 10.1089/soro.2019.0186.

[34] T. Akagi, S. Dohta, S. Fujimoto, Y. Tsuji, and Y. Fujiwara, “Development of Flexible Thin Actuator Driven by Low Boiling Point Liquid,” *International Journal of*

Materials Science and Engineering, vol. 3, no. 1, pp. 55–59, 2015, doi: 10.12720/ijmse.3.1.55-59.

[35] Z. Zhou, Q. Li, L. Chen, C. Liu, and S. Fan, "A large-deformation phase transition electrothermal actuator based on carbon nanotube-elastomer composites," *J Mater Chem B*, vol. 4, no. 7, pp. 1228–1234, 2016, doi: 10.1039/c5tb02715b.

[36] K. Nakahara, K. Narumi, R. Niiyama, and Y. Kawahara, "Electric phase-change actuator with inkjet printed flexible circuit for printable and integrated robot prototyping," *Proc IEEE Int Conf Robot Autom*, pp. 1856–1863, 2017, doi: 10.1109/ICRA.2017.7989217.

[37] R. A. Bilodeau, A. Miriyev, H. Lipson, and R. Kramer-Bottiglio, "All-soft material system for strong soft actuators," *2018 IEEE International Conference on Soft Robotics, RoboSoft 2018*, pp. 288–294, 2018, doi: 10.1109/ROBOSOFT.2018.8404934.

[38] Y. Nishikawa and M. Matsumoto, "A design of fully soft robot actuated by gas–liquid phase change," *Advanced Robotics*, vol. 33, no. 12, pp. 567–575, 2019, doi: 10.1080/01691864.2019.1626281.

[39] D. J. Kang, S. An, A. L. Yarin, and S. Anand, "Programmable soft robotics based on nano-textured thermo-responsive actuators," *Nanoscale*, vol. 11, no. 4, pp. 2065–2070, 2019, doi: 10.1039/c8nr08215d.

[40] M. Garrad, G. Soter, A. T. Conn, H. Hauser, and J. Rossiter, "Driving soft robots with low-boiling point fluids," *RoboSoft 2019 - 2019 IEEE International Conference on Soft Robotics*, pp. 74–79, 2019, doi: 10.1109/ROBOSOFT.2019.8722812.

[41] R. Chellattoan, A. Yudhanto, and G. Lubineau, “Low-Voltage-Driven Large-Amplitude Soft Actuators Based on Phase Transition,” *Soft Robot*, vol. 7, no. 6, pp. 688–699, 2020, doi: 10.1089/soro.2019.0150.

[42] K. Narumi *et al.*, “Liquid Pouch Motors: Printable Planar Actuators Driven by Liquid-to-Gas Phase Change for Shape-Changing Interfaces,” *IEEE Robot Autom Lett*, vol. 5, no. 3, pp. 3915–3922, 2020, doi: 10.1109/LRA.2020.2983681.

[43] B. Oh *et al.*, “Untethered Soft Robotics with Fully Integrated Wireless Sensing and Actuating Systems for Somatosensory and Respiratory Functions,” *Soft Robot*, vol. 7, no. 5, pp. 564–573, 2020, doi: 10.1089/soro.2019.0066.

[44] Y. il Kim, S. An, A. L. Yarin, and S. S. Yoon, “Performance Enhancement of Soft Nanotextured Thermopneumatic Actuator by Incorporating Silver Nanowires into Elastomer Body,” *Soft Robot*, vol. 00, no. 00, pp. 1–9, 2020, doi: 10.1089/soro.2020.0044.

[45] X. Li, H. Duan, P. Lv, and X. Yi, “Soft Actuators Based on Liquid–Vapor Phase Change Composites,” *Soft Robot*, vol. 00, no. 00, pp. 1–11, 2020, doi: 10.1089/soro.2020.0018.

[46] J. Han, W. Jiang, H. Zhang, B. Lei, L. Wang, and H. Liu, “Submersible Soft-Robotic Platform for Noise-Free Hovering Utilizing Liquid–Vapor Phase Transition,” *Advanced Intelligent Systems*, vol. 3, no. 1, p. 2000147, 2021, doi: 10.1002/aisy.202000147.

[47] H.-J. Lee and K. J. Loh, “Liquid vaporization actuated soft structures with active cooling and heat loss control,” *Smart Mater Struct*, vol. 30, no. 5, p. 055007, 2021, doi: 10.1088/1361-665x/abeefb.

[48] G. L. Liu, J. Kim, Y. U. Lu, and L. P. Lee, “Optofluidic control using photothermal nanoparticles,” *Nat Mater*, vol. 5, no. 1, pp. 27–32, 2006, doi: 10.1038/nmat1528.

[49] D. Baigl, “Photo-actuation of liquids for light-driven microfluidics: State of the art and perspectives,” *Lab Chip*, vol. 12, no. 19, pp. 3637–3653, 2012, doi: 10.1039/c2lc40596b.

[50] J. Palacci, S. Sacanna, A. P. Steinberg, D. J. Pine, and P. M. Chaikin, “Colloidal Surfers,” *Science (1979)*, vol. 339, no. February, pp. 936–939, 2013, doi: 10.1126/science.1230020.

[51] M. J. Esplandiu, A. A. Farniya, and A. Bachtold, “Silicon-Based Chemical Motors : An E ffi cient Pump for Triggering and Guiding Fluid Motion Using Visible Light,” no. 11, pp. 11234–11240, 2015, doi: 10.1021/acsnano.5b04830.

[52] L. Xu, F. Mou, H. Gong, M. Luo, and J. Guan, “Light-driven micro/nanomotors: From fundamentals to applications,” *Chem Soc Rev*, vol. 46, no. 22, pp. 6905–6926, 2017, doi: 10.1039/c7cs00516d.

[53] J. Luo, J. Zheng, F. Wei, W. Yang, L. Yao, and Z. Zhan, “Recent advances of light-driven micro/nanomotors: toward powerful thrust and precise control,” *Nanotechnol Rev*, vol. 7, no. 6, pp. 555–581, 2018, doi: 10.1515/ntrev-2018-0106.

[54] B. M. Tansi, M. L. Peris, O. E. Shklyaev, A. C. Balazs, and A. Sen, “Organization of Particle Islands through Light-Powered Fluid Pumping,” *Angewandte Chemie - International Edition*, vol. 58, no. 8, pp. 2295–2299, 2019, doi: 10.1002/anie.201811568.

[55] W. Li, X. Wu, H. Qin, Z. Zhao, and H. Liu, “Light-Driven and Light-Guided Microswimmers,” *Adv Funct Mater*, vol. 26, no. 18, pp. 3164–3171, 2016, doi: 10.1002/adfm.201505378.

[56] M. Li, Y. Su, H. Zhang, and B. Dong, “Light-powered direction-controlled micropump,” *Nano Res*, vol. 11, no. 4, pp. 1810–1821, 2018, doi: 10.1007/s12274-017-1799-5.

[57] Y. Hong, M. Diaz, U. M. Córdova-Fteueroa, and A. Sen, “Light-driven titanium-dioxide-based reversible microfireworks and micromotor/micropump systems,” *Adv Funct Mater*, vol. 20, no. 10, pp. 1568–1576, 2010, doi: 10.1002/adfm.201000063.

[58] J. C. Ndukaife, A. Mishra, U. Guler, A. G. A. Nnanna, S. T. Wereley, and A. Boltasseva, “Photothermal heating enabled by plasmonic nanostructures for electrokinetic manipulation and sorting of particles,” *ACS Nano*, vol. 8, no. 9, pp. 9035–9043, 2014, doi: 10.1021/nn502294w.

[59] S. J. Williams, A. Kumar, N. G. Green, and S. T. Wereley, “A simple, optically induced electrokinetic method to concentrate and pattern nanoparticles,” *Nanoscale*, vol. 1, no. 1, pp. 133–137, 2009, doi: 10.1039/b9nr00033j.

[60] S. Santer, “Remote control of soft nano-objects by light using azobenzene containing surfactants,” *J Phys D Appl Phys*, vol. 51, no. 1, 2018, doi: 10.1088/1361-6463/aa95ca.

[61] D. Feldmann, S. R. Maduar, M. Santer, N. Lomadze, O. I. Vinogradova, and S. Santer, “Manipulation of small particles at solid liquid interface: Light driven diffusioosmosis,” *Sci Rep*, vol. 6, no. November, pp. 1–10, 2016, doi: 10.1038/srep36443.

[62] A. D. Jadhav *et al.*, “Photoresponsive microvalve for remote actuation and flow control in microfluidic devices,” *Biomicrofluidics*, vol. 9, no. 3, pp. 1–12, 2015, doi: 10.1063/1.4923257.

[63] A. Diguet *et al.*, “Photomanipulation of a droplet by the chromocapillary effect,” *Angewandte Chemie - International Edition*, vol. 48, no. 49, pp. 9281–9284, 2009, doi: 10.1002/anie.200904868.

[64] C. Zhou, H. Zhang, Z. Li, and W. Wang, “Chemistry pumps: A review of chemically powered micropumps,” *Lab Chip*, vol. 16, no. 10, pp. 1797–1811, 2016, doi: 10.1039/c6lc00032k.

[65] R. Merindol and A. Walther, “Materials learning from life: Concepts for active, adaptive and autonomous molecular systems,” *Chem Soc Rev*, vol. 46, no. 18, pp. 5588–5619, 2017, doi: 10.1039/c6cs00738d.

[66] S. Helmy, F. A. Leibfarth, S. Oh, J. E. Poelma, C. J. Hawker, and J. R. De Alaniz, “Photoswitching using visible light: A new class of organic photochromic molecules,” *J Am Chem Soc*, vol. 136, no. 23, pp. 8169–8172, 2014, doi: 10.1021/ja503016b.

[67] S. Helmy, S. Oh, F. A. Leibfarth, C. J. Hawker, and J. Read De Alaniz, “Design and synthesis of donor-acceptor stenhouse adducts: A visible light photoswitch derived from furfural,” *Journal of Organic Chemistry*, vol. 79, no. 23, pp. 11316–11329, 2014, doi: 10.1021/jo502206g.

[68] J. R. Hemmer *et al.*, “Tunable Visible and Near Infrared Photoswitches,” *J Am Chem Soc*, vol. 138, no. 42, pp. 13960–13966, 2016, doi: 10.1021/jacs.6b07434.

[69] J. R. Hemmer *et al.*, “Controlling Dark Equilibria and Enhancing Donor-Acceptor Stenhouse Adduct Photoswitching Properties through Carbon Acid Design,” *J Am Chem Soc*, vol. 140, no. 33, pp. 10425–10429, 2018, doi: 10.1021/jacs.8b06067.

[70] M. M. Lerch *et al.*, “Tailoring Photoisomerization Pathways in Donor-Acceptor Stenhouse Adducts: The Role of the Hydroxy Group,” *Journal of Physical Chemistry A*, vol. 122, no. 4, pp. 955–964, 2018, doi: 10.1021/acs.jpca.7b10255.

[71] M. M. Lerch, S. J. Wezenberg, W. Szymanski, and B. L. Feringa, “Unraveling the Photoswitching Mechanism in Donor-Acceptor Stenhouse Adducts,” *J Am Chem Soc*, vol. 138, no. 20, pp. 6344–6347, 2016, doi: 10.1021/jacs.6b01722.

[72] N. Mallo *et al.*, “Structure-function relationships of donor-acceptor Stenhouse adduct photochromic switches,” *Chem Sci*, vol. 9, no. 43, pp. 8242–8252, 2018, doi: 10.1039/c8sc03218a.

[73] M. M. Lerch, W. Szymański, and B. L. Feringa, “The (photo)chemistry of Stenhouse photoswitches: Guiding principles and system design,” *Chem Soc Rev*, vol. 47, no. 6, pp. 1910–1937, 2018, doi: 10.1039/c7cs00772h.

[74] N. Mallo *et al.*, “Photochromic switching behaviour of donor-acceptor Stenhouse adducts in organic solvents,” *Chemical Communications*, vol. 52, no. 93, pp. 13576–13579, 2016, doi: 10.1039/C6CC08079K.

[75] M. M. Lerch *et al.*, “Solvent Effects on the Actinic Step of Donor–Acceptor Stenhouse Adduct Photoswitching,” *Angewandte Chemie - International Edition*, vol. 57, no. 27, pp. 8063–8068, 2018, doi: 10.1002/anie.201803058.

[76] N. Mallo *et al.*, “Structure-function relationships of donor-acceptor Stenhouse adduct photochromic switches,” *Chem Sci*, vol. 9, no. 43, pp. 8242–8252, 2018, doi: 10.1039/c8sc03218a.

[77] B. F. Lui *et al.*, “Unusual concentration dependence of the photoisomerization reaction in donor–acceptor Stenhouse adducts,” *Photochemical & Photobiological Sciences*, pp. 1587–1595, 2019, doi: 10.1039/c9pp00130a.

[78] N. D. Dolinski *et al.*, “A Versatile Approach for In Situ Monitoring of Photoswitches and Photopolymerizations,” *ChemPhotoChem*, vol. 1, no. 4, pp. 125–131, 2017, doi: 10.1002/cptc.201600045.

[79] W. Thielicke and E. J. Stamhuis, “42-489-1-Pb,” 2014.

[80] B. F. Lui *et al.*, “Unusual concentration dependence of the photoisomerization reaction in donor–acceptor Stenhouse adducts,” *Photochemical & Photobiological Sciences*, pp. 1587–1595, 2019, doi: 10.1039/c9pp00130a.

[81] H. Gao, B. Ji, I. L. Ja, E. Arzt, and P. Fratzl, “Materials become insensitive to flaws at nanoscale :,” *Proc Natl Acad Sci U S A*, vol. 100, no. 10, pp. 5597–5600, 2003.

[82] F. Barthelat and R. Rabiei, “Toughness amplification in natural composites,” *J Mech Phys Solids*, vol. 59, no. 4, pp. 829–840, 2011, doi: 10.1016/j.jmps.2011.01.001.

[83] F. Barthelat, “Designing nacre-like materials for simultaneous stiffness, strength and toughness: Optimum materials, composition, microstructure and size,” *J Mech Phys Solids*, vol. 73, pp. 22–37, 2014, doi: 10.1016/j.jmps.2014.08.008.

[84] F. Barthelat, Z. Yin, and M. J. Buehler, “Structure and mechanics of interfaces in biological materials,” *Nat Rev Mater*, vol. 1, no. 1, p. 16007, 2016, doi: 10.1038/natrevmats.2016.7.

[85] J. W. C. Dunlop, R. Weinkamer, and P. Fratzl, “Artful interfaces within Biological materials have a wide range of mechanical properties,” *Materials Today*, vol. 14, no. 3, pp. 70–78, 2011, doi: 10.1016/S1369-7021(11)70056-6.

[86] H. Yuk, T. Zhang, G. A. Parada, X. Liu, and X. Zhao, “Skin-inspired hydrogel-elastomer hybrids with robust interfaces and functional microstructures,” *Nat Commun*, vol. 7, no. May, pp. 1–11, 2016, doi: 10.1038/ncomms12028.

[87] S. Lin, C. Cao, Q. Wang, M. Gonzalez, J. E. Dolbow, and X. Zhao, “Design of stiff, tough and stretchy hydrogel composites via nanoscale hybrid crosslinking and macroscale fiber reinforcement,” *Soft Matter*, vol. 10, no. 38, pp. 7519–7527, 2014, doi: 10.1039/c4sm01039f.

[88] Y. Huang *et al.*, “Superior fracture resistance of fi ber reinforced polyampholyte hydrogels achieved by extraordinarily large energy-dissipative process zones †,” *J Mater Chem A Mater*, vol. 7, no. 7, pp. 13431–13440, 2019, doi: 10.1039/c9ta02326g.

[89] Y. Huang *et al.*, “Energy-Dissipative Matrices Enable Synergistic Toughening in Fiber Reinforced Soft Composites,” *Adv Funct Mater*, vol. 27, p. 1605350, 2017, doi: 10.1002/adfm.201605350.

[90] N. Suksangpanya, N. A. Yaraghi, R. B. Pipes, D. Kisailus, and P. Zavattieri, “Crack twisting and toughening strategies in Bouligand architectures,” *Int J Solids Struct*, vol. 150, pp. 83–106, 2018, doi: 10.1016/j.ijsolstr.2018.06.004.

[91] G. X. Gu, F. Libonati, S. D. Wettermark, and M. J. Buehler, “Printing nature: Unraveling the role of nacre’s mineral bridges,” *J Mech Behav Biomed Mater*, vol. 76, no. May, pp. 135–144, 2017, doi: 10.1016/j.jmbbm.2017.05.007.

[92] P. Zhang, M. A. Heyne, and A. C. To, “Biomimetic staggered composites with highly enhanced energy dissipation: Modeling, 3D printing, and testing,” *J Mech Phys Solids*, vol. 83, pp. 285–300, 2015, doi: 10.1016/j.jmps.2015.06.015.

[93] A. R. Studart, “Additive manufacturing of biologically-inspired materials,” *Chem. Soc. Rev.*, vol. 45, no. 2, pp. 359–376, 2016, doi: 10.1039/C5CS00836K.

[94] G. X. Gu, I. Su, S. Sharma, J. L. Voros, Z. Qin, and M. J. Buehler, “Three-Dimensional-Printing of Bio-Inspired Composites,” *J Biomech Eng*, vol. 138, no. 2, p. 021006, 2016, doi: 10.1115/1.4032423.

[95] G. I. Peterson *et al.*, “Production of Materials with Spatially-Controlled Cross-Link Density via Vat Photopolymerization,” *ACS Appl Mater Interfaces*, vol. 8, no. 42, pp. 29037–29043, 2016, doi: 10.1021/acsami.6b09768.

[96] A. Sydney Gladman, E. A. Matsumoto, R. G. Nuzzo, L. Mahadevan, and J. A. Lewis, “Biomimetic 4D printing,” *Nat Mater*, vol. 15, no. 4, pp. 413–418, 2016, doi: 10.1038/nmat4544.

[97] J. O. Hardin, T. J. Ober, A. D. Valentine, and J. A. Lewis, “Microfluidic printheads for multimaterial 3D printing of viscoelastic inks,” *Advanced Materials*, vol. 27, no. 21, pp. 3279–3284, 2015, doi: 10.1002/adma.201500222.

[98] N. D. Dolinski *et al.*, “Solution Mask Liquid Lithography (SMaLL) for One-Step, Multimaterial 3D Printing,” *Advanced Materials*, vol. 30, no. 31, p. 1800364, 2018, doi: 10.1002/adma.201800364.

[99] J. J. Schwartz and A. J. Boydston, “Multimaterial actinic spatial control 3D and 4D printing,” *Nat Commun*, vol. 10, p. 791, 2019, doi: 10.1038/s41467-019-08639-7.

[100] J. Norman, J. G. Shapter, K. Short, L. J. Smith, and N. L. Fazzalari, “Micromechanical properties of human trabecular bone: A hierarchical investigation using nanoindentation,” *J Biomed Mater Res A*, vol. 87, no. 1, pp. 196–202, 2008, doi: 10.1002/jbm.a.31766.

[101] J. Y. Rho, L. Kuhn-Spearing, and P. Zioupos, “Mechanical properties and the hierarchical structure of bone,” *Med Eng Phys*, vol. 20, no. 2, pp. 92–102, 1998, doi: 10.1016/S1350-4533(98)00007-1.

[102] S. A. Ruiz and C. S. Chen, “Emergence of Patterned Stem Cell Differentiation Within Multicellular Structures,” *Stem Cells*, vol. 26, no. 11, pp. 2921–2927, 2008, doi: 10.1634/stemcells.2008-0432.

[103] Y. Sasai, “Cytosystems dynamics in self-organization of tissue architecture,” *Nature*, vol. 493, no. 7432, pp. 318–326, 2013, doi: 10.1038/nature11859.

[104] A. J. Bidhendi, B. Altartouri, F. P. Gosselin, and A. Geitmann, “Mechanical Stress Initiates and Sustains the Morphogenesis of Wavy Leaf Epidermal Cells,” *Cell Rep*, vol. 28, no. 5, pp. 1237–1250, 2019, doi: 10.1016/j.celrep.2019.07.006.

[105] V. Gordon, L. Bakhtiari, and K. Kovach, “From molecules to multispecies ecosystems: The roles of structure in bacterial biofilms,” *Phys Biol*, vol. 16, no. 4, p. 041001, 2019, doi: 10.1088/1478-3975/ab1384.

[106] T. J. Deming, “Mussel byssus and biomolecular materials,” *Curr Opin Chem Biol*, vol. 3, no. 1, pp. 100–105, 1999, doi: 10.1016/S1367-5931(99)80018-0.

[107] J. H. Waite and C. C. Broomell, “Changing environments and structure-property relationships in marine biomaterials,” *Journal of Experimental Biology*, vol. 215, no. 6, pp. 873–883, 2012, doi: 10.1242/jeb.058925.

[108] J. H. Waite, X. X. Qin, and K. J. Coyne, “The peculiar collagens of mussel byssus,” *Matrix Biology*, vol. 17, no. 2, pp. 93–106, 1998, doi: 10.1016/S0945-053X(98)90023-3.

[109] J. H. Waite, E. Vaccaro, C. Sun, and J. M. Lucas, “Elastomeric gradients: A hedge against stress concentration in marine holdfasts?,” *Philosophical Transactions of the Royal Society B: Biological Sciences*, vol. 357, no. 1418, pp. 143–153, 2002, doi: 10.1098/rstb.2001.1025.

[110] M. H. Wilhelm, E. Filippidi, J. H. Waite, and M. T. Valentine, “Influence of multi-cycle loading on the structure and mechanics of marine mussel plaques,” *Soft Matter*, vol. 13, no. 40, pp. 7381–7388, 2017, doi: 10.1039/c7sm01299c.

[111] E. Carrington and J. M. Gosline, “Mechanical design of mussel byssus: Load cycle and strain rate dependence,” *Am Malacol Bull*, vol. 18, no. 1, pp. 135–142, 2004.

[112] N. Bandara, H. Zeng, and J. Wu, “Marine mussel adhesion: Biochemistry, mechanisms, and biomimetics,” *J Adhes Sci Technol*, vol. 27, no. 18–19, pp. 2139–2162, 2013, doi: 10.1080/01694243.2012.697703.

[113] H. G. Silverman and F. F. Roberto, “Understanding marine mussel adhesion,” *Marine Biotechnology*, vol. 9, no. 6, pp. 661–681, 2007, doi: 10.1007/s10126-007-9053-x.

[114] H. Lee, N. F. Scherer, and P. B. Messersmith, “Single-molecule mechanics of mussel adhesion,” *Proceedings of the National Academy of Sciences*, vol. 103, no. 35, pp. 12999–13003, 2006, doi: 10.1073/pnas.0605552103.

[115] M. J. Sever, J. T. Weisser, J. Monahan, S. Srinivasan, and J. J. Wilker, “Metal-Mediated Cross-Linking in the Generation of a Marine-Mussel Adhesive,”

Angewandte Chemie - International Edition, vol. 43, no. 4, pp. 448–450, 2004, doi: 10.1002/anie.200352759.

[116] Q. Lin *et al.*, "Adhesion mechanisms of the mussel foot proteins mfp-1 and mfp-3," *Proceedings of the National Academy of Sciences*, vol. 104, no. 10, pp. 3782–3786, 2007, doi: 10.1073/pnas.0607852104.

[117] N. Holten-Andersen *et al.*, "pH-induced metal-ligand cross-links inspired by mussel yield self-healing polymer networks with near-covalent elastic moduli.," *Proc Natl Acad Sci U S A*, vol. 108, no. 7, pp. 2651–2655, Feb. 2011, doi: 10.1073/pnas.1015862108.

[118] E. Filippidi *et al.*, "Toughening elastomers using mussel-inspired iron-catechol complexes," *Science (1979)*, vol. 358, no. 6362, pp. 502–505, 2017, doi: 10.1126/science.aao0350.

[119] N. Holten-Andersen, H. Zhao, and J. H. Waite, "Stiff coatings on compliant biofibers: The cuticle of Mytilus californianus byssal threads," *Biochemistry*, vol. 48, no. 12, pp. 2752–2759, 2009, doi: 10.1021/bi900018m.

[120] A. Reinecke, L. Bertinetti, P. Fratzl, and M. J. Harrington, "Cooperative behavior of a sacrificial bond network and elastic framework in providing self-healing capacity in mussel byssal threads," *J Struct Biol*, vol. 196, no. 3, pp. 329–339, 2016, doi: 10.1016/j.jsb.2016.07.020.

[121] E. W. Hawkes, C. Majidi, and M. T. Tolley, "Hard questions for soft robotics," 2021. [Online]. Available: https://www.science.org

[122] R. Uramune, H. Ishizuka, T. Hiraki, Y. Kawahara, S. Ikeda, and O. Oshiro, "HaPouch: A Miniaturized, Soft, and Wearable Haptic Display Device Using a Liquid-to-Gas

Phase Change Actuator," *IEEE Access*, vol. 10, pp. 16830–16842, 2022, doi: 10.1109/ACCESS.2022.3141385.

[123] "Preliminary_Experiments_Conducted_on_Prototypes_of_Sensitivity-changeable_Soft_Tactile_Sensors_Utilizing_Phase_Change".

[124] Q. Lyu, S. Gong, J. Yin, J. M. Dyson, and W. Cheng, "Soft Wearable Healthcare Materials and Devices," *Advanced Healthcare Materials*, vol. 10, no. 17. John Wiley and Sons Inc, Sep. 01, 2021. doi: 10.1002/adhm.202100577.

[125] N. D. Naclerio *et al.*, "Controlling subterranean forces enables a fast, steerable, burrowing soft robot," 2021. [Online]. Available: https://www.science.org

[126] N. Boddeti *et al.*, "Optimal Soft Composites for Under-Actuated Soft Robots," *Adv Mater Technol*, vol. 6, no. 8, Aug. 2021, doi: 10.1002/admt.202100361.

[127] M. Cartolano, B. Xia, A. Miriyev, and H. Lipson, "Conductive fabric heaters for heat-activated soft actuators," *Actuators*, vol. 8, no. 1, 2019, doi: 10.3390/act8010009.

[128] O. Coddington, J. L. Lean, P. Pilewskie, M. Snow, and D. Lindholm, "A solar irradiance climate data record," *Bull Am Meteorol Soc*, vol. 97, no. 7, pp. 1265–1282, Jul. 2016, doi: 10.1175/BAMS-D-14-00265.1.

[129] N. D. Dolinski *et al.*, "Solution Mask Liquid Lithography (SMaLL) for One-Step, Multimaterial 3D Printing," *Advanced Materials*, vol. 1800364, p. 1800364, 2018, doi: 10.1002/adma.201800364.

[130] N. D. Dolinski *et al.*, "A Versatile Approach for In Situ Monitoring of Photoswitches and Photopolymerizations," *ChemPhotoChem*, vol. 1, no. 4, pp. 125–131, 2017, doi: 10.1002/cptc.201600045.